The Dissertation Committee for Shanzhong Gong Certifies that this is the approved version of the following dissertation:

Mechanisms of Nucleoside Analog Resistance and the Role of Magnesium Ions in HIV-1 Reverse Transcriptase

Committee:

Kenneth Johnson, Supervisor

Ilya Finkelstein

Rick Russell

Christian Whitman

Yan Jessie Zhang

Mechanisms of Nucleoside Analog Resistance and the Role of Magnesium Ions in HIV-1 Reverse Transcriptase

by

Shanzhong Gong, B.Ag., M.Ag., M.S.

Dissertation

Presented to the Faculty of the Graduate School of

The University of Texas at Austin

in Partial Fulfillment

of the Requirements

for the Degree of

Doctor of Philosophy

The University of Texas at Austin

August 2016

Dedication

to

my father Huainian Wu,

my mother Benqun Gong,

my wife Jieyi Zhu

and my son Rui Gong

Acknowledgements

I would like to thank my advisor, Dr. Kenneth Johnson, for all his support over the past five years. His guidance helped me not only in learning enzyme kinetics, but also in cultivating problem solving abilities. His patience, integrity, and peaceful mind in dealing scientific problems set an excellent example for students like me. I feel that I was very lucky to have such a wonderful advisor and mentor. In addition, I would like to thank Dr. JoAnn Johnson for her continuous support in the lab and in my life. I want to thank her for spending so much time to hone my oral presentation skills, and teach me how to handle stress and be positive. She and Dr. Kenneth Johnson mold the scientist and person that I am today.

I would like to thank my lab member and also my best friend Dr. An Li, who always provided support and good advices at the corner. It is not very often to have such a good friend who not only gives encouragement and help but also provides criticism and feedbacks, as I need it. I am also grateful to other lab members that I have been fortunate to work with: Dr. Erin Taylor, Dr. Myong-chul Koag, Jiawen Li, Brian Villalba, and Tyler Dangerfield. In addition, I would like to thank my previous lab members: Dr. Yufeng Qian and Dr. Jessica Mckenzie for their support and help during my graduate study.

I would like to express my gratitude to my doctoral committee members: Dr. Rick Russell, Dr. Jessie Zhang, Dr. Christian Whitman and Dr. Ilya Finkelstein for their suggestions and scientific expertise. In addition, I would like to give my special thanks to Dr. Jessie Zhang who spent her precious time offering invaluable advice and help on my research.

Finally, I would like giving many thanks to my family. I am grateful to my father Huainian Wu and my mother Benqun Gong for training me as good and useful person for the society. I would like to thank my mother-in law Laiping Lee and my mom for taking turns to take care of my son in the past two years. In addition, I would like to thank my dear wife Jieyi Zhu for providing endless support and love through the ups and downs of my graduate study. I also would like to thank my lovely son Rui Gong for giving me so much joy.

Mechanisms of Nucleoside Analog Resistance and the Role of Magnesium Ions in HIV-1 Reverse Transcriptase

Shanzhong Gong, Ph.D

The University of Texas at Austin, 2016

Supervisor: Kenneth Allen Johnson

Effectiveness of antiviral drugs used to treat HIV infections is limited by the evolution of drug resistance. There are two common mechanisms leading to the resistance against nucleoside reverse transcriptase inhibitors (NRTIs): Selective discrimination before incorporation and excision after incorporation. In order to better understand the mechanisms of NRTI resistance, we investigated each step involved in the incorporation and excision of two NRTIs: Azidothymidine (AZT) and Tenofovir (TFV) using two RT mutants, K65R and K66R. Our results showed that the mutation of K65R does not significantly affect the ATP-mediated NRTIs excision, but rather affects the pyrophosphate-mediated NRTIs excision by decreasing the efficiency of pyrophosphate-mediated excision. Our data suggest that K65R may not prefer the ATP- or pyrophosphate-mediated excision as a mechanism to excise NRTIs leading to drug resistance. Rather, the NRTI resistance conferred by K65R is achieved mainly through the discrimination mechanism rather than through the excision mechanism. Furthermore,

our results showed that the primary effect of K65R on NRTI discrimination (TFV and AZT) is to decrease the rate of the chemistry step. In addition, our results showed that the drug resistances for TFV and AZT conferred K65R are comparable. Compared with K65R, the resistance conferred by K66R is mild.

We also revisited the classic two-metal-ion mechanism from analysis of enzyme kinetics and crystal structure. Our data showed that a tight binding (K_d is 0.5 μM) of the Mg^{2+}-nucleotide complex induces a conformational change of the enzyme from open to the closed state. The catalytic Mg^{2+} binds (K_d is 3.7 mM) after the conformational change. The binding of the catalytic Mg^{2+} stabilizes the Mg^{2+}-nucleotide complex in the active site and stimulates the catalysis of the reaction. In addition, our data suggested that changing the free Mg^{2+} from 10 mM to 0.25 mM significantly affects the processivity, but not the fidelity of HIVRT.

Table of Contents

List of Tables

List of Figures

List of Illustrations

Chapter 1: Introduction to HIV-1 Reverse Transcriptase

1.1 Project Summary

The research project reported in this dissertation aims to further expand our understanding on the mechanisms of drug resistance conferred by HIV-1 reverse transcriptase (HIVRT), as well as the effects of magnesium ions (Mg^{2+}) on the activities of HIVRT. Chapter one provides a detailed introduction to HIV infection and HIVRT. Chapter two presents the effects of a clinically important mutation (K65R) and a non-clinically observed mutation (K66R) on the discrimination against tenofovir (TFV) and zidovudine (AZT). Chapter three presents the effects of two mutations (K65R and K66R) on the excision of TFV and AZT by directly comparing the efficiencies of three reactions (nucleotide incorporation, ATP-mediated excision and pyrophosphate-mediated excision) to provide a more thorough understanding regarding the resistance of nucleoside reverse transcriptase inhibitors (NRTIs). Chapter four presents the effects of Mg^{2+} on nucleotide specificity, and it also provides a better and more detailed understanding of the general two-metal-ion mechanism. Finally, chapter five presents the effects of Mg^{2+} on the fidelity and processivity of HIVRT, as well as the effects of Mg^{2+} on DNA binding.

1.2 History of HIV and AIDS

Human Immunodeficiency Virus (HIV) is a lentivirus that belongs to the retrovirus family. The infection of HIV ultimately causes the acquired immunodeficiency syndrome (AIDS), which has claimed many lives in the last thirty years. The virus was discovered in 1983 and it was first named as human T-cell lymphotropic virus-type III/lymphadenopathy-associated virus by an international scientific committee, and identified as the cause of AIDS by two separate groups led by Robert Gallo and Luc

Montagnier (1). In the USA, this disease was first observed in 1981 among injecting drug users and homosexual men. The patients had compromised immunity system with no specific cause, and later they developed a rare skin cancer called "Kaposi's Sarcoma (KS)". By 1982, it was known that this disease was not limited to the gay community, therefore the term AIDS was introduced.

HIV can be divided into two major types, HIV type 1 (HIV-1) and HIV type 2 (HIV-2). HIV-1 is the predominant type and it exists worldwide, while HIV-2 mainly exists in the West Africa. HIV-1 can be further classified into 4 groups named as M, N, O, and P respectively. Groups of N, O, and P are not very common and exist only in Cameroon, Gabon and equatorial Guinea regions (2). Group of M is the most important group in worldwide, and it also can be further classified into 9 subtypes (A, B, C, D, F, G, H, J, and K) (2). The origin of HIV-1 was reported from a virus called simian immunodeficiency virus (SIVcps) affecting a subspecies of chimpanzees living in west equatorial Africa, while the origin of HIV-2 was reported from simian immunodeficiency virus (SIVsmm) affecting the sooty mangabey (old world monkey) (3). Most people believed that it is the long exposure of SIV in human (hunters in Africa) that allowed the evolution of SIV to adapt and infect humans. Others believed that it was the unsafe medical and sexual practices in Africa that allowed the evolution of SIV to HIV and the rapid transmission of HIV among humans (4).

There are three main modes of transmission for HIV: sexual contact, exposure to body fluids (blood and blood product), and mother to child transmission. Sexual contact is the most frequent mode of transmission, among which homosexual transmission is most common. However, different countries or regions may have different situation. For example, man-to-man transmission accounted for 64% of all new cases in U.S.A in 2009 (5). Exposure to body fluids is the second frequent mode of transmission (6). In

developing countries, blood transfusion is the most dominant way in this type of transmission due to the poor hygiene and regulation condition in those areas. Mother-to-child transmission is the vertical form of transmission of the virus, and it can occur during pregnancy, delivery or breast feeding. There are no risk of infection in people exposed to patient feces, nasal secretion, saliva, vomit, sweat and tears as long as no blood contamination was found (7).

The symptoms of HIV infection can be classified into three stages. The first stage is called the initial symptom. Some people may not have any obvious symptoms at this stage, but most of them may have influenza-like symptoms such as fever, throat inflammation, rash, and headache (8). This stage occurs usually 2-4 weeks after the exposure to the virus. The recommendation for diagnosis of HIV infection at this stage is that patients may have unexpected fever after exposure to the virus for a few weeks. The second stage of infection is called clinical latency, and it can last from 3 years to about 20 years. Usually, there are no symptoms at the beginning of this stage. The symptoms will occur at the end of this stage, and people may have fever, weight loss, muscle pain, gastrointestinal problems (9). The third and also the last stage of the infection is called acquired immunodeficiency syndrome (AIDS). At this stage, the number of CD4+ T cell decreased significantly, and usually it count below 200 cells per μL. Due to the impaired immune system, people are very susceptible to various diseases and usually tend to develop various virally induced cancers including cervical cancer, Burkitt's lymphoma, Kaposi's Sarcoma, primary central nervous system, and lymploma (8). In addition, people with AIDS frequently exhibit systematic symptoms such as prolonged fever, sweats, chills, weakness, significant weight loss and diarrhea (10).

From its first clinical report to 2012, AIDS has caused a total of 36 million deaths worldwide (11). In 2014, there were 1.2 million deaths and 36.9 million HIV patients (Figure 1.1), and the new infections continue at a rate of about 2.3 million per year (12). In U.S.A, there were 1.2 million HIV-infected individuals and 17,500 deaths in 2008. The US Centers for Disease Control and Prevention estimated that about 20% of HIV-infected individuals were unaware of the infection.

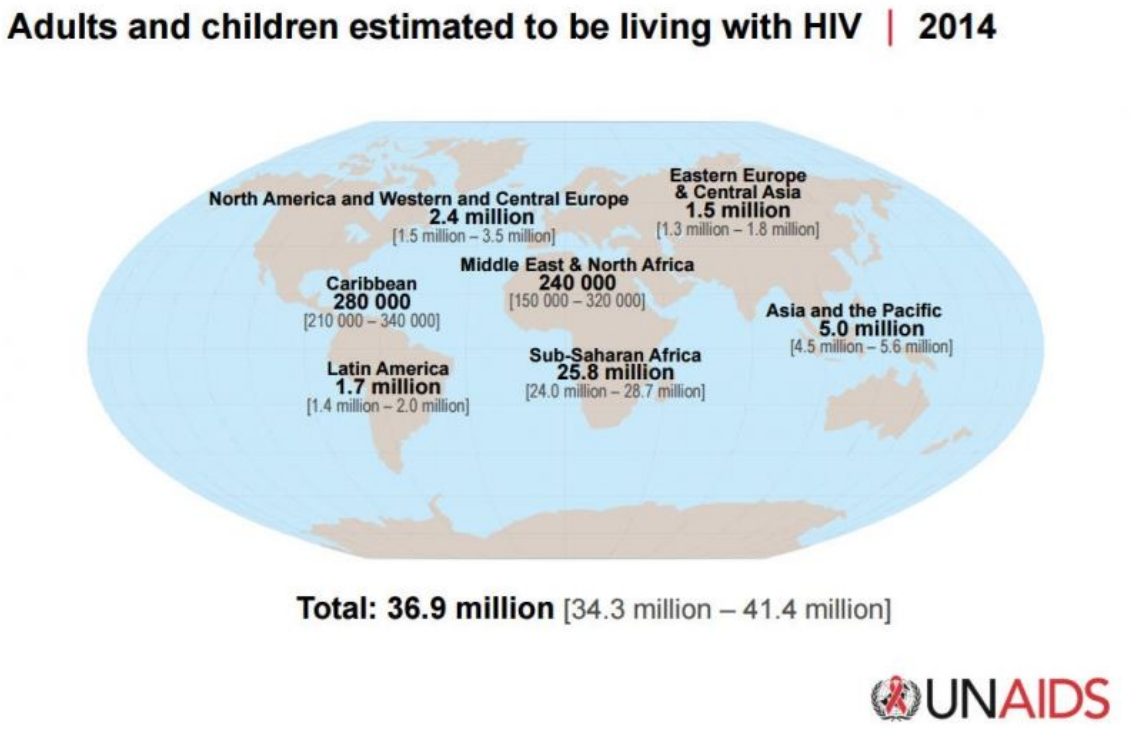

Figure 1.1 HIV infection worldwide in 2014.

Reproduced from online source (https://www.phan.ca/hiv-aids-changed-everything/)

The diagnosis of HIV infection is based on laboratory testing and the appearance of certain signs and symptoms (13). Laboratory testing also includes two methods. The first method is to use enzyme-linked immunosorbent assay (ELISA) to test HIV infection and this method is based on specific antibody. The second method is to use polymerase chain reaction (PCR) technology to detect HIV-RNA (14). If the initial testing is positive, another round of ELISA or PCR is needed to confirm the HIV infection. In children younger than 18 months, the antibody testing may not be very accurate due to the presence of maternal antibodies (15). In this case, The diagnosis of HIV infection can only based on PCR testing for HIV-RNA or p24 antigen (13). In many developing countries, the diagnosis of HIV infection can only based on antibody testing and certain signs or symptoms of AIDS due to lack of access to the PCR testing.

The prevention of HIV infection consists of the recommendation for the use of condoms and the programs to prevent the mother-to-child transmission. It is reported that consistent use of condom reduces the risk of HIV transmission in sexual contact by 80% (16). It is also reported that treatment of patients with HIV inhibitors before and after the sexual contact hugely decreased the risk of transmission of the virus (17). The program for preventing the mother-to-child transmission requires treatment of HIV infection for both mother and infant during the pregnancy period and after birth. In addition, it also requires the change of traditional feeding, using bottle feeding rather than breast feeding (16). It is reported that this method can reduce the vertical transmission of HIV infection by 92-99% (18).

Currently, there is no licensed vaccine for HIV infection. In 2009, it is reported that a group of scientists developed a vaccine called RV144, and it could provide partial protection (about 30%) against HIV infection. However, further studies are still required to make it more effective (19, 20). The treatment of HIV infection or AIDS includes the

use of highly active antiretroviral therapy (HAART), which consists of at least three medicines belonging to at least two separate classes of HIV inhibitors. It is true that this treatment significantly decreases the progression of the disease to AIDS and reduces the risk of death. But it is also true that there is significant toxicity along with the use of HAART. For example, it is reported that the adverse effects include but are not limited to lipodystrophy syndrome, dyslipidemia, diabetes mellitus and cardiovascular diseases (14, 21).

1.3 HIV STRUCTURE, LIFE CYCLE, AND TREATMENT

The virus is about 100 nm in diameter (22). The outmost layer of the viral particle is the lipid envelope, in which a transmembrane glycoprotein gp41 is embedded (Figure 1.2). A surface glycoprotein protein called gp120 is attached with gp41. Both gp41 and gp120 are critical proteins for virus binding to host cells, encoded by *env* gene of the viral RNA (22). Inside the viral particle are the matrix protein p17, capsid core proteins p24 and p6, and nucleocapsid (NC) protein p7, encoded by the *gag* gene of the viral RNA. It is believed that NC proteins bind to viral RNA and protect it from degradation and facilitate the RNA template annealing in the viral replication stage (23). Inside the capsid, there are 2 copies of the roughly 9 kb (kilo base) length of positive-sense RNA strands, which are bound with NC proteins. Inside the matrix and capsid, there are three important proteins: HIV protease, integrase and reverse transcriptase, and they are critical for viral replication, transcription and maturation. All three proteins are encoded by *pol* gene of the viral RNA genome (22). In addition, other proteins such as viral infectivity protein (vif), viral protein R (vpr), transactivator of transcription (tat), regulator of viral protein expression (rev) and negative regulatory factor (nef) are also abundant. The specific

functions of those proteins have not been fully characterized. Except for that, viral protein u (vpu) and viral protein x (vpx) are specific for HIV-1 and HIV-2 respectively (22).

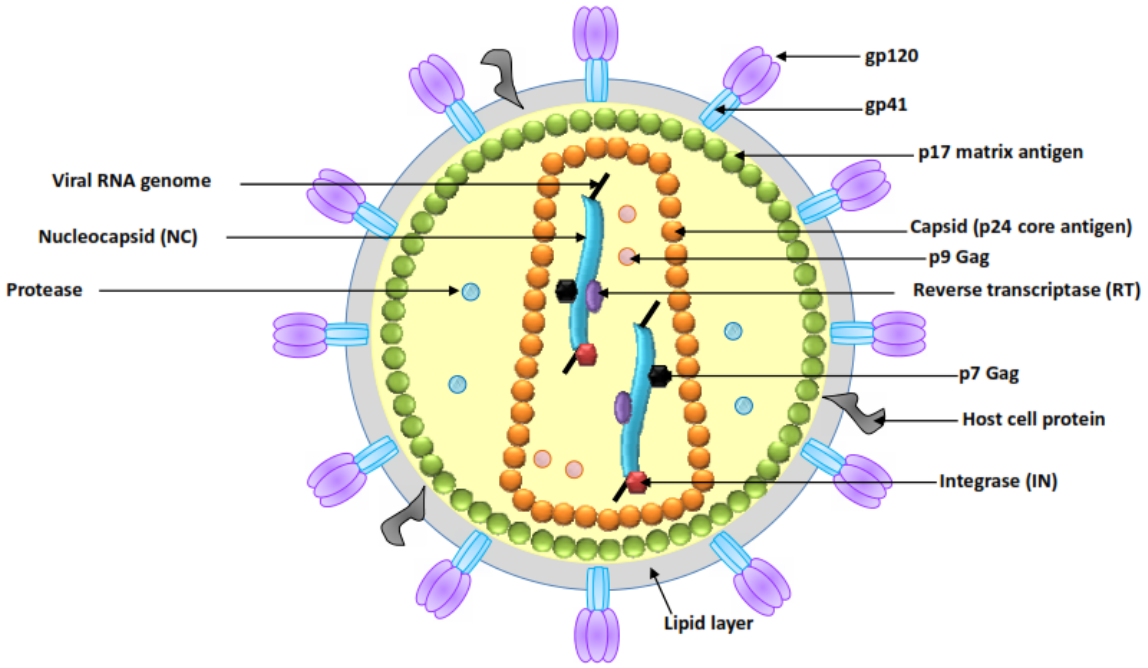

Figure 1.2 Structure of HIV viral particle.

The virus contains lipid layer, matrix and capsid core. Two copies of RNA are kept inside of capsid surrounded by NC proteins. Gp41 and gp120 proteins are located outside of lipid layer, while other viral proteins are located inside of matrix and capsid. The picture is reproduced from Shum KT, Zhou J, Rossi JJ. 2013 (or reference (24)).

For HIV transmitted by sexual contact, the virus first infects the dendritic cells in the mucosal membrane areas surrounding mouth, vagina, rectum, penis and upper gastrointestinal tract. Then, the virus is transported from site of infection to the lymph nodes, where it begins to infect other immune cells such as CD4+ lymphocytes (T cells) and macrophages. For infecting T cells, the virus first attaches to the CD4 receptor expressed on the surface of CD4+ lymphocytes by using its gp120 and gp41 spikes, and the binding causes the conformational change in the host cell envelop which allows the binding of two co-receptors: CXC-chemokine receptor 4 (CXCR4) and/or CC-chemokine receptor 5 (CCR5). The binding of co-receptor brings the virus closer to the cell membrane, and causes the fusion between the viral envelope and host cell membrane. After the fusion, the virus releases its two copies of positive-sense RNA and abundant viral proteins into the cytoplasm of the host cells, and the viral replication begins (Figure 1.3).

The first step of the replication is replication of the single-stranded RNA into double-stranded DNA catalyzed by HIV reverse transcriptase. The new synthesized double-stranded DNA will then be transported into the nucleus of the host cell and integrated into the host genome by HIV integrase. Later, the viral DNA will be converted to mRNA along with host genomic transcription and the viral mRNA will then be translated into the various viral protein precursors. Following that, new synthesized viral protein and viral RNA will be packaged, assembled, and ready for budding. At the same time, poly-protein precursors will be cleaved by HIV protease to allow formation of mature virus particles ready for infecting other healthy cells (25).

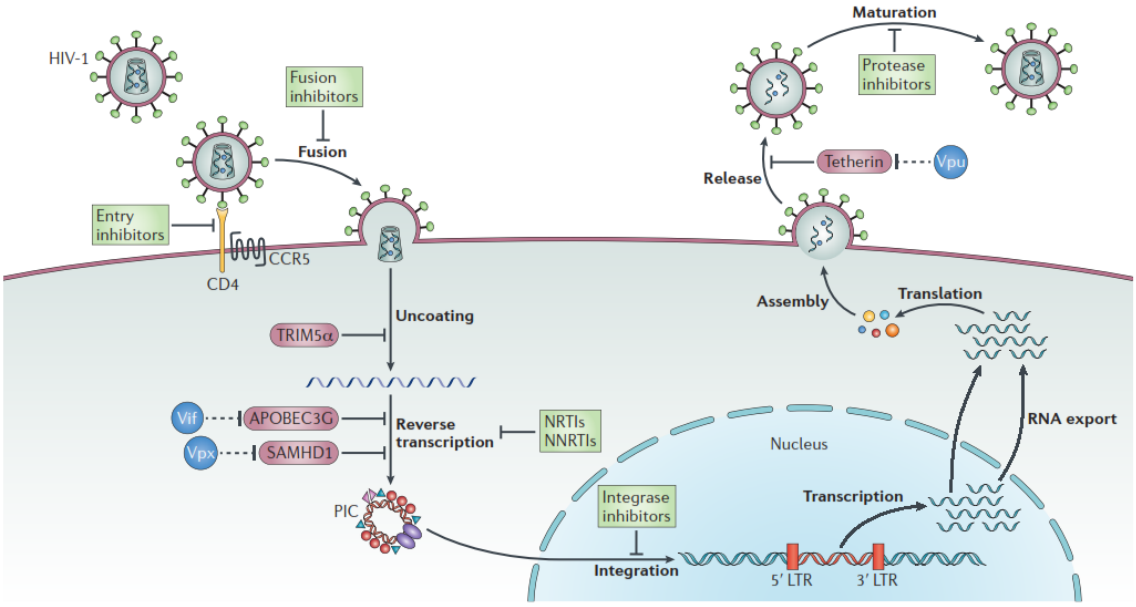

Figure 1.3 Life cycle of HIV.

The virus first enters the host cells through CD4 receptor and CCR5 co-receptor. After the entry, the viral RNA is converted to double-stranded DNA by HIV reverse transcriptase, which will be integrated into the host genome by HIV integrase. After transcription along with the host genome, the viral mRNA is transported outside of nucleus and translated into viral protein precursors. Later, The viral particle will be assembled and released from the host cells and the precursors will be cleaved to yield various viral proteins at this stage. The picture is reproduced from Engelman A and Cherepanov P. 2012 (or reference (25)).

Currently, the treatment of HIV infections is to use a combination therapy, called highly active antiretroviral therapy (HAART), to target the life cycle of the virus at various stages and thereby prevent it from replicating inside the host cells. It is reported that the treatment of HAART effectively reduces the risk of transmission to others, and makes HIV patients live longer and healthier (8). Because HAART does not eliminate all viruses inside the cell, it is used to control the multiplication of the virus but cannot cure the disease. Therefore, the treatment has to be used continuously for a long time. According to the life cycle of the virus, the HIV drugs can be classified into six classes (Figure 1.3). The first two classes of HIV drug are called fusion inhibitors and entry inhibitors. Fusion inhibitors block the fusion step between the HIV envelop and the cell membrane of CD4+ cell, and therefore prevent the virus from infecting the host cells (26). For example, peptide fusion inhibitors (T-20, enfuvirtide) block the activity of gp41 by preventing its intramolecular interactions (27). Entry inhibitors work in a similar way, but they target at CCR5 at the host cell. For example, small molecule CCR5 antagonists target at the hydrophobic pocket of CCR5 and block its binding to the HIV envelop (26). Along with the wide usage of those inhibitors, drug resistance also occurs. It is reported that the mutations in the amino terminal heptad repeat region of gp41 lead to the resistance to fusion inhibitors (28). It is believed that the mutations not only decrease the binding affinity of fusion inhibitors but also decrease the efficiency of fusion between the viral envelope and host cell membrane (29, 30). Although there are a few cases of failure in the use of entry inhibitors, the clinical experience of this class of inhibitors is still not enough to define the mechanism of resistance. It is reported that the susceptibility of entry inhibitors may depend on cell types, state of cellular activation, and the number of HIV entering the cell (31).

The third class of HIV drugs is the nucleoside reverse transcriptase inhibitors (NRTIs). NRTIs are normally administrated as prodrugs, and they require the phosphorylation by host cellular kinases for transforming to their active (triphosphate) forms (32). The structures of NRTIs are very similar to that of natural nucleosides, except that they lack 3'-hydroxyl group. After the incorporation of NRTIs, the next incoming nucleotide cannot be incorporated because NRTIs do not allow the formation of the subsequent 3'-5' phosphodiester bond. Therefore, NRTIs are also called chain terminators. Previously eight NRTIs were approved by the FDA for treatment of HIV infections (Figure 1.4); namely, abacavir (ABC), didanosine (ddI), emtricitabine (FTC), lamivudine (3TC), stavudine (d4T), zalcitabine (ddC), zidovudine (AZT) and tenofovir (TFV or TNV). Because the structures of NRTIs are very similar to that of natural nucleotides, some of them also react readily with human mitochondrial polymerase, which causes depletion of mitochondrial DNA leading to toxicity. Currently, two NRTIs (d4T and ddC) have been eliminated from the FDA approval list because their severe toxicity (33).

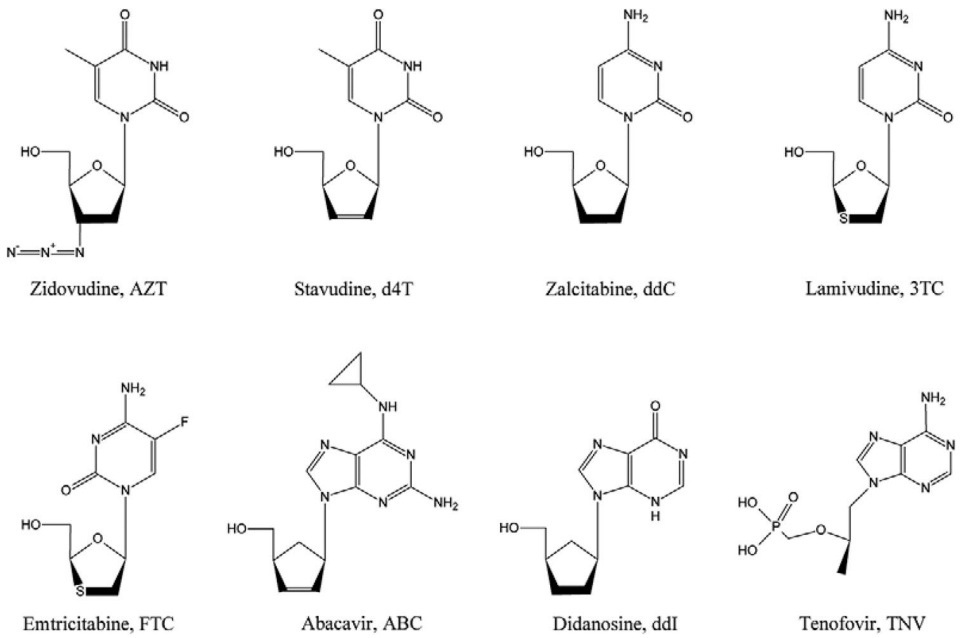

Figure 1.4 Chemical Structures of FDA approved NRTIs.

Abacavir (ABC), didanosine (ddI), emtricitabine (FTC), lamivudine (3TC), stavudine (d4T), zalcitabine (ddC), zidovudine (AZT) and tenofovir (TFV or TNV). The picture is reproduced from Lucianna Helene Santos et al., 2015 (reference (34))

The fourth class of HIV drugs is the non-nucleoside reverse transcriptase inhibitors (NNRTIs). They create and bind to a new hydrophobic pocket, which is adjacent to the active site of HIVRT. The hydrophobic residues around the active site that are involved in the binding of NNRTIs include: Y187, Y188, F227, W229 and Y232; and the hydrophilic residues that are involved include: K101, K103, S105, D192, and E224. Except for those residues in the p66 subunit, one residue (E138) in p51 subunit is also involved (35). The binding of NNRTIs changes the alignment of the primer grip, dimerization interface and the geometry of the catalytic aspartic residues in the YMDD motif (36-38). It is reported that the binding of NNRTs does not inhibit the initial binding of natural nucleotide, but only inhibits the chemistry step of nucleotide incorporation by allosteric mechanism (39, 40). Currently, there are four FDA approved NNRTIs: etravirine, delavirdine, efavirenz, and nevirapine (26). The resistance of NNRTIs is observed due to mutations in the immediate vicinity of the hydrophobic binding pocket. Two common mutations believed to play important role in NNRTIs resistance are K103N and Y182C (41). In contrast to other HIV drugs, the resistance of NNRTIs does not decrease the viral replicative fitness significantly (42).

The last two classes of HIV drugs are integrase inhibitors and protease inhibitors. Because HIV integrase targets the 3'-end processing of viral DNA and strand transfer, integrase inhibitors are designed by targeting the strand transfer step. Therefore, they are also named as integrase strand transfer inhibitors (inSTIs) (43). The structure of integrase inhibitors contains a metal binding pharmacophore and hydrophobic groups that interact with both DNA and enzyme (44). They function by binding to the specific complex between integrase and DNA, and interacting with two Mg^{2+} ions in the active site of the enzyme and the DNA template. Therefore, the mutations that lead to the resistance of integrase inhibitors usually locate at the active site of the enzyme. As a result, the

resistance of integrase inhibitors also leads to the decrease of the enzyme function and viral replicative fitness (45).

HIV protease is a small protein (kDa) responsible for the cleavage of the polyprotein precursor (46). Currently, there are 10 FDA approved protease inhibitors (PIs): amprenavir (APV), atazanavir (ATZ), darunavir (TMC114), fosamprenavir (Lexiva), indinavir (IDV), lopinavir (LPV), nelfinavir (NFV), ritonavir (RTV), saquinavir (SQV) and tipranavir (TPV). The resistance of PIs involves a stepwise accumulation of primary and compensatory mutations (47). The locations of primary mutations are close to the active site of the enzyme. Therefore, the resistance of PIs also decreases the replicative fitness of the virus (48).

1.4 HIV REVERSE TRANSCRIPTASE

Reverse transcription is an essential step in the HIV replication. It converts single-stranded RNA into double-stranded DNA by using HIV reverse transcriptase (HIVRT). The first step of reverse transcription is the primer annealing, using the 3'-end of host tRNA basing pair with a 18 nucleotide long complementary sequence in the 5'-end of the viral RNA (Figure 1.5). This special sequence is called the primer binding site (PBS)(49). After primer annealing, HIVRT begins to synthesize the first DNA strand (the minus strand), forming a DNA/RNA duplex. Then, the RNA part of this duplex is degraded by the RNase H activity of HIVRT, leaving the new synthesized DNA intact. The exposed new synthesized DNA has a sequence that is complementary to the direct repeat region in the 3'-end of the viral RNA, which allows the DNA to anneal with the 3'-end of the viral RNA in a step called first (minus strand) transfer. Then, the minus strand synthesis continues. At the same time, the RNase H domain of HIVRT continues to degrade the

RNA of the new-formed DNA/RNA duplex. The degradation of RNA stops at the specific position containing a purine-rich sequence (the polypurine tract, PPT). Then, PPT serves as a primer for second strand (plus strand) DNA synthesis. The plus strand synthesis continues until it reaches the end of DNA template and copies the first 18 nucleotides of the host tRNA. Then, HIVRT removes the host tRNA, leaving a ribo-A in end of its DNA strand. The 18 nucleotides in the 3'-end of the new exposed plus strand DNA is complementary to the 5'-end of minus strand DNA, which allows the second (plus strand) transfer. After the second transfer occurs, plus strand DNA synthesis continues, making the double-stranded DNA. The new synthesized double-stranded DNA is longer than its original viral RNA, and it contains the same sequences at both ends of the DNA called long terminal repeats (LTRs) (50). The advantage of having two copies of viral RNA in its viral particle is that DNA synthesis still can continue by using strand transfer if one of the two copies of its viral RNA that has nicks or is damaged (51).

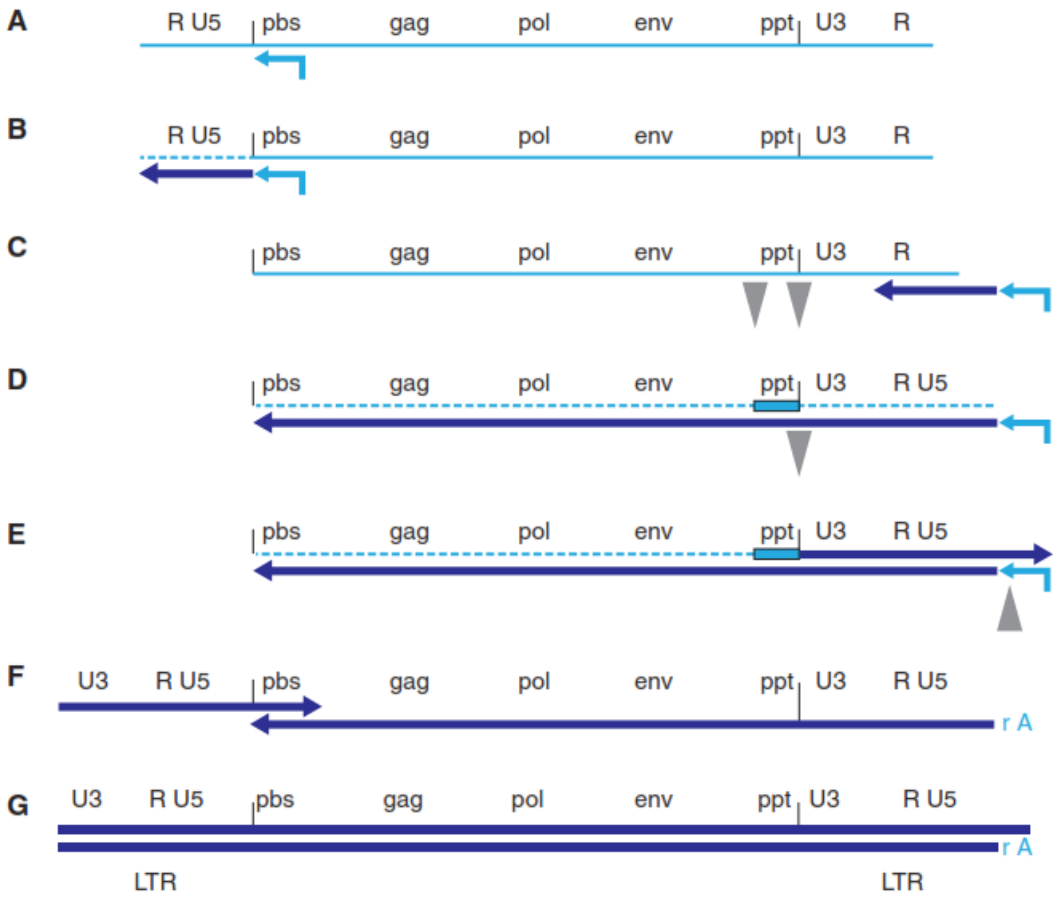

Figure 1.5 Process of HIV Reverse Transcription.

The virus uses our host tRNA as a primer to initiate the reverse transcription (A, B). Along with minus strand synthesis, HIVRT also degrades the RNA part of the new synthesized DNA/RNA duplex (B). Then, first strand transfer occurs (C) and minus strand synthesis continues. The RNA part of the new synthesized DNA/RNA is degraded by HIVRT (D), and the polypurine tract (PPT) of RNA serves as primer for plus strand synthesis (E). The host tRNA is removed by HIVRT when the new synthesized plus strand DNA has reached the 3'-end of the minus strand (E). The second strand transfer occurs and plus strand synthesis continues (F). Then, double-stranded DNA is finished. The picture is reproduced from Hu WS, Hughes SH. 2012 (or reference (50)).

HIV reverse transcriptase is produced by the cleavage of Gag-pol polyprotein using HIV protease. The mature form of HIVRT is an asymmetric heterodimer (Figure 1.6), which contains two subunits: p66 and p51, 560 and 440 amino acids in length respectively. The p66 subunit contains two domains: polymerase domain and RNase H domain. The polymerase domain also contains four subdomains: fingers, palm, thumb, and connection (52). The p51 subunit does not have an RNase H domain, but it also contains four subdomains, although arrangements of the four subdomains differ from that of the p66 subunit (53). The p66 subunit is enzymatically active, while the p51 subunit plays only structural role in the dimer (52, 54). There are two active sites in HIVRT P66 (Figure 1.5) for polymerase and RNase H activities. The distance between the two active sites spans a distance corresponding to 18 nucleotides of duplex DNA. Three aspartatic acid residues (D110, D185, and D186) in the polymerase domain coordinate with two Mg^{2+} ions in the active site, while four residues (D443, E478, D498, and D549) in the RNase H domain have similar functions (52).

The nucleic acid binding cleft of HIVRT is formed by the contribution of both p51 and p66 subunits. Two subdomains of the p51 subunit (connection and thumb subdomains) provide the base for the cleft, while all four subdomains and RNase H domain of the p66 subunit work together to complete the DNA binding cleft. In addition, several highly conserved motifs are involved in positioning of the nucleic acid. It is reported that the RNase H primer grip near the active site of RNase H domain plays an important role in positioning the RNA/DNA duplex for proper cleavage. It is also reported that the DNA primer grip (β12-β13 hairpin) near the active site of polymerase domain helps by positioning the 3'-OH end of the primer at the polymerase site (55, 56). For either RNA/DNA or DNA/DNA, the duplex is in B-form for most of its length in

binding to the enzyme. However, the duplex bends about 40° near the thumb of the p66 subunit to transform the B-form duplex to A-form as it enters the polymerase active site. The bending or transition is finished through stretching about 4 nucleotides. Although the structure of the RNA/DNA duplex is very similar to DNA/DNA duplex when bound to the enzyme, the structures are not identical, and some refer to the structure of RNA/DNA duplex as H-form (50). In either case, it is clear that the interaction of the duplex with the enzyme alters its structure.

At the time of nucleotide incorporation, a part of the fingers subdomain (β3-β4 loop) undergoes a large conformational change from open to closed. After nucleotide incorporation, the enzyme reopens to release the pyrophosphate. Then, the duplex shifts (or translocates) to move the 3'-end of the primer from nucleotide binding site (N site) to primer site (P site), which allows the next incoming nucleotide binding at the N site. The repeated translocation is of great importance in the processive DNA synthesis (51). It is reported that two aspartic acid residues (D185 and D186) in the highly conserved YMDD motif of the polymerase domain are involved in the regulation of translocation (57).

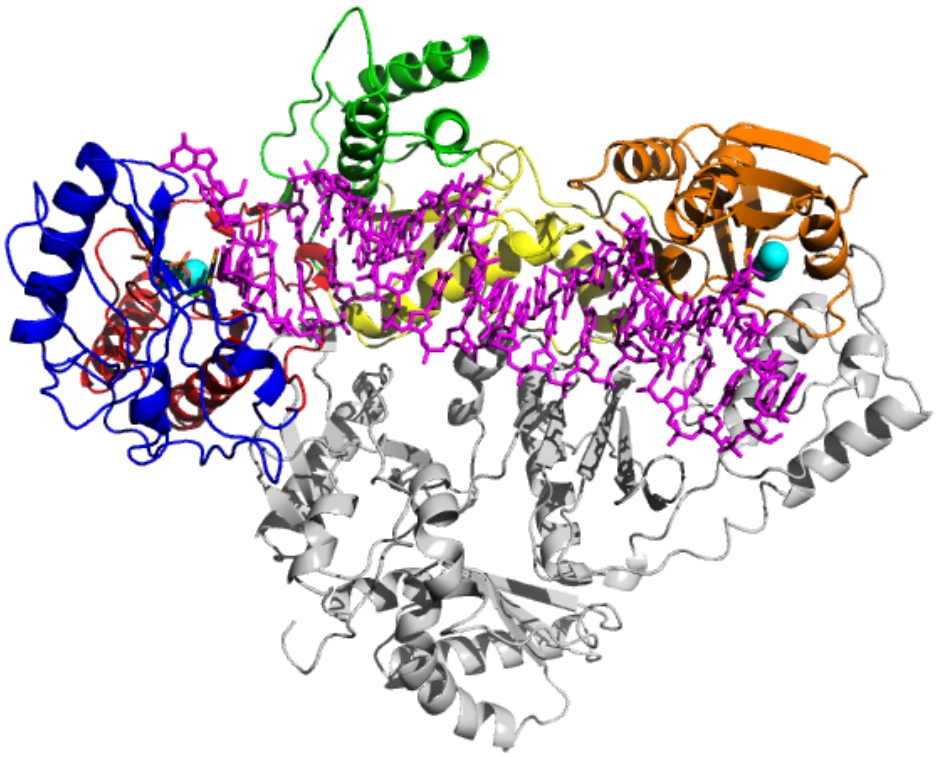

Figure 1.6 Structure of HIVRT.

The mature form of HIVRT contains two subunits: p66 (colored) and p51 (grey). The fingers, palm, thumb, connection subdomains and the RNase H domain of the p66 subunit are shown in blue, red, green, yellow and orange respectively. The Mg^{2+} ions in the polymerase and RNase H active sites are shown in cyan spheres. The picture is created from pdb file (1rtd).

The nucleotide binding pocket in the polymerase active site of HIVRT contains residues including Lysine 65 (K65), Arginine 72 (R72), Glutamine 151 (Q151), Tyrosine 115 (Y115), Alanine 114 (A114), Aspartic acid 110 (D110) (Figure 1.6). Crystal structures show that the triphosphate of the incoming nucleotide interacts with the ε-amino group of K65, the guanidinium group of R72, the main chain of residue 113 and 114, and two magnesium (Mg^{2+}) ions. Residues K65 and R72 donate hydrogen bonds to the α-phosphate and γ -phosphate of the incoming nucleotide, respectively (Figure 1.7). In the structure, the 3'-OH of the primer end in the active site aligns very well to attack the α-phosphate of the incoming nucleotide. The chemical reaction is catalyzed by the two-metal-ion mechanism using the two Mg^{2+} ions in the active site (58).

It has also been suggested that the RNase H domain catalyzes the cleavage reaction using the two-metal-ion mechanism as well (51). Recently, the crystal structure of HIVRT shows that there are two manganese ions (Mn^{2+}) in the active site of RNase H domain, and the distance between them is about 4 angstrom. In addition, calorimetry and solution NMR studies also suggested that there are two Mn^{2+} or Mg^{2+} ions in the RNase H active site (59, 60).

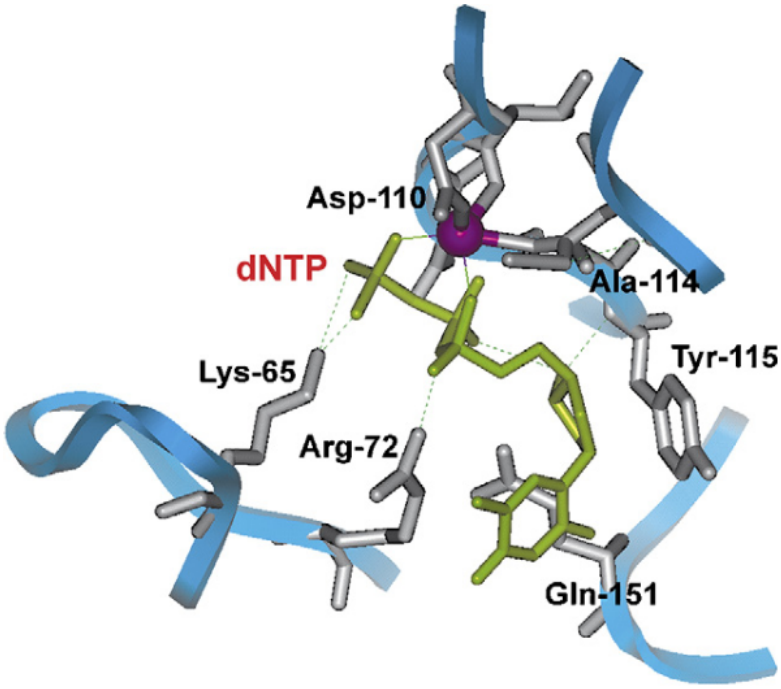

Figure 1.7 The nucleotide-binding pocket of HIVRT.

The incoming dNTP is shown in yellow-green stick, the residues in the active site that are involved in dNTP binding are shown in grey sticks, and one of the Mg^{2+} ions is shown in purple sphere. The picture is reproduced from Menendez-Arias L. 2008 (reference (61)).

1.5 KEY MUTATIONS IN HIV REVERSE TRANSCRIPTASE AND NRTIS RESISTANCE

The long-term use of NRTIs has led to the emergence of multiple NRTI-resistance mutations. The mechanisms of NRTI resistance are classified into two categories: discrimination and excision. The discrimination mechanism is where HIVRT discriminates against NRTIs to prevent or slow down their rates of incorporation. The mutated residues involved in NRTI discrimination (eg. Q151M, M184V, and K65R) usually are located at the nucleotide-binding pocket and interacted with the incoming nucleotide (Figure 1.7). For example, K65R in β3-β4 loop, which shows resistance against TFV, interacts with the γ-phosphate of the incoming nucleotide; M184V, which shows high resistance to 3TC, interacts with ribose ring of the incoming nucleotide; and Q151M complex, which is a combination of six mutations (A62V, V75L, F72L, F116Y and Q151M), affects the architecture of dNTP binding pocket and provides discrimination against many NRTIs including AZT, ddI, ddC, d4T, ABC, and 3TC (61, 62). The "excision mechanism" is based on a mechanism in which NRTIs are excised from the end of the primer after they have been incorporated into the DNA template. The signature mutations that lead to NRTI excision are also called thymidine analogue resistance mutations (TAMs). They are a combination of several mutations (M41L, T215Y/T215F, D67N, K70N, L210W, and K219Q/K219E), which show high resistance against AZT and d4T (61, 63, 64). TAMs mutations are located at both fingers and palm subdomain of the HIVRT, and most are located outside of the nucleotide-binding pocket (Figure 1.8) (65, 66).

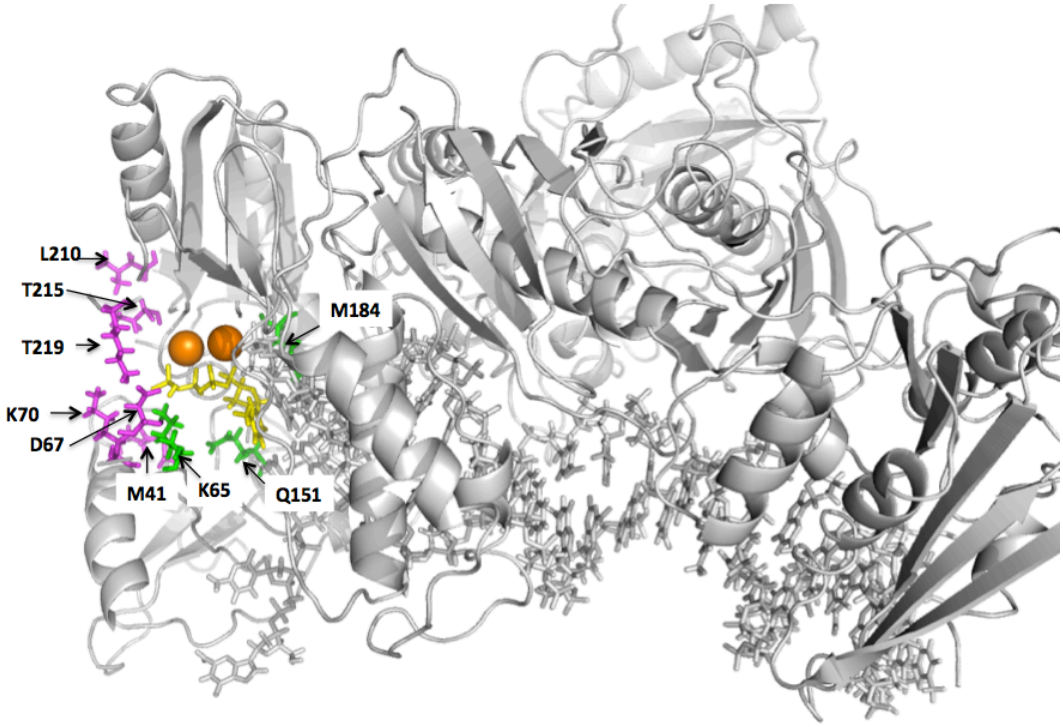

Figure 1.8 Mutations of HIVRT lead to NRTIs resistance.

The incoming dNTP is shown in yellow stick, two Mg^{2+} ions are shown in orange spheres, mutations leading to NRTIs discrimination are shown in green sticks and mutations leads to NRTIs excision are shown in magenta. The image was created from pdb file (1rtd).

M184I/V: Residue M184 interacts with both dNTP and the 3'-end of the primer in the active site of HIVRT, and M184I/V mutation confers high resistance to many NRTIs. In particular the M184I/V mutation confers a high resistance against 3TC (Figure 1.4) by decreasing the incorporation efficiency (k_{pol}/K_d) of 3TC (67, 68). The crystal structure of 3TC bound with HIVRT showed that the M184I/V mutation causes a steric hindrance between L-oxathiolane ring of 3TC and the side chain of β-branched amino acids (Valine or Isoleucine), which may affect the binding of 3TC and the chemistry of the incorporation (58, 69, 70). It is also reported that the M184I/V mutation cause resistance to elvucitabine, an experimental NRTI that is similar to 3TC in its structure, by decreasing the rate of chemistry (71). The M184I/V mutation also causes resistance to abacavir, a carbocyclic synthetic nucleoside analogue of dGTP, by decreasing the rate of chemistry for about 50-fold (71). In addition, this mutation causes resistance to emtricitabine, which is a synthetic nucleotide analogue of cytidine, and two other NRTIs (ddC and ddI) (72-74). In low concentration of dNTP, this mutation also decreases the viral replication fitness (75, 76).

Q151M: Glutamine 151 (Q151) is located in the palm subdomain of HIVRT, and its side chain interacts with the ribose ring of incoming dNTP (58). The mutation of Q151M confers low-level resistance to many NRTIs including AZT, ddI, d4T, ddC, TFV, ABC, and 3TC (77-80). Previous kinetic experiments have suggested that Q151M decreases the rate of chemistry for many NRTIs (68). The possible mechanism has been suggested that the mutation of Gln to Met disrupts a hydrogen-bond network between the incoming nucleotide and the residues in the active site of HIVRT (81). When Q151M is combined with other mutations such as A62V, V75L, F72L, F116Y, it forms what is

referred to as the “Q151M complex”, which shows a high resistance to many NRTIs. It is suggested that Q151M complex affects the architecture of dNTP binding pocket (61).

TAMs: Thymidine analogue resistance mutations (TAMs) are a combination of several mutations (M41L, T215Y/T215F, D67N, K70N, L210W, and K219Q/K219E), and it shows resistance to AZT and d4T by an excision mechanism. Most of the TAMs are located outside the nucleotide-binding pocket and they do not interact with the primer end or incoming nucleotides or ATP. There are two kinds of nucleotide excision that may be responsible for NRTI resistance: ATP-mediated excision and pyrophosphate-mediated excision (pyrophosphorolysis). ATP-mediated excision has been studied more intensely because the physiological concentration of ATP is much higher than that of pyrophosphate. When ATP reacts with an AZT-terminated primer, it forms dinucleoside tetraphosphate (AZTppppA) resulting in the excision of AZT. After the excision, HIVRT allows subsequent nucleotide binding and DNA synthesis. The excision efficiency can be affected by many factors such as specific NRTIs (AZT, d4T, ddT, and ddA), or nucleotide sequence (82).

There are two mutational patterns observed clinically: TAM-1 and TAM-2. TAM-1 is also called primary resistance mutations because it causes higher levels of resistance and this mutational pattern contains mutations including M41L, L210W, and T215Y. TAM-2 is called the secondary resistance mutations and it contains mutations including D67N, K70R, K219E/K, and T215F (83, 84). It is reported that Y215 in TAM-1 facilitates ATP binding through π-π interaction with the adenine ring of ATP, which may explain why TAM-1 has a higher resistance (85).

When TAMs are combined with other mutations, the resistance against NRTIs is also altered. For example, TAMs are also combined with a T69S insertion complex, which a substitution of Thr with Ser at position 69, followed by a dipeptide insertion

(Ser-Ser, Ser-Gly or Ser-Ala), leading to increased resistance against AZT (86, 87). As TAMs are combined with A62V mutation or deletions in the β3-β4 loop, the resistance is also increased (88-90). In addition, when TAMs are combined with the mutations in the RNase H primer grip or mutations in the connection domain, it also increases NRTIs resistance by reducing the frequency of template switch and by shifting the balance between RNase H activity and polymerase (ATP-mediated excision in this case) activity toward the polymerase activity in favor of NRTIs excision (91). When A371V (connection domain mutation) and Q509L (RNase H domain mutation) are combined with TAMs (M41L/L210W/T215Y) or (D67N/K70R/T215F), the AZT resistance is increased for about 10~50-fold (92).

1.6 THE EFFECTS OF K65R AND K66R MUTATIONS ON NRTI RESISTANCE

Lysine 65 is located at the β3-β4 loop in the fingers subdomain and interacts with the γ-phosphate of the incoming nucleotide via its ε-amino group (58). Accordingly, the mutation of K65R is thought to change this interaction explaining resistance to many NRTIs including TFV, ddC, ddI, d4T, 3TC and FTC (93-95). It is reported that the K65R is the signature mutation for TFV, and the resistance against TFV is achieved by the discrimination mechanism (96). It is also proposed that the mutation of K65R forms a rigid molecular platform with R72, which restrains the conformational change of HIVRT and reduces the efficiency of NRTIs incorporation (96). However, biochemical experiments are still needed to test this hypothesis. In addition, Lysine 65 and 66 residues are adjacent to each other in the fingers domain of HIVRT. Although the NRTIs resistance due to K66R mutation was very rarely reported, K66 lies adjacent to the

phosphate of the penultimate nucleotide (97), and therefore it is highly possible that this residue is directly or indirectly involved in the nucleotide or NRTIs incorporation.

It has been reported that K65R mutant increases the susceptibility to AZT incorporation (96, 98-100) and it has been proposed that the rigid molecular platform between K65R and K72 restrains the conformational change of HIVRT thereby decreasing the efficiency of NRTIs excision by reducing ATP binding and ATP-mediated excision (96). However, a recent report showed that AZT and TFV are associated with similar reductions in HIV-1 RNA levels in the presence of the K65R mutant (101). Whether the mutation of K65R causes a different or a comparable drug resistance against AZT and TFV is still under investigation. In addition, pyrophosphorolysis and ATP-mediated excision occur by attacking the phosphodiester bond between the penultimate nucleotide and the NRTI at the 3' end of the primer (102). Because K66 is located adjacent to the penultimate nucleotide, it is possible that this non-clinical mutation (K66R) may have some effects on pyrophosphorolysis or ATP-mediated excision, from which it may cause some resistance against AZT.

The cross talk between K65R and other mutations may affect the NRTI resistance as well. It is reported that the combination of K65R and M184V causes a high resistance to 3TC by decreasing its rate of incorporation value more than 1000-fold compared with natural nucleotide. This combination also causes a high resistance to a combined NRTI treatment containing 3TC, abacavir and TFV, or a combined NRTI treatment containing TFV and emtricitabine (95, 103). In addition, it also reduces the viral replication capacity because it decreases the processivity as well as the level of minus-strand DNA (94, 104).

1.7 THE EFFECTS OF Mg^{2+} ON THE ACTIVITIES OF HIVRT

The catalytic activity of many polymerases is achieved by the assistance of Mg^{2+}, through a mechanism called a general two metal ion mechanism (105). In this mechanism, there are two Mg^{2+} ions bound in the active site of many polymerases (Figure 1.9), which are called catalytic Mg^{2+} (or Mg^{2+} A) and nucleotide bound Mg^{2+} (or Mg^{2+} B), respectively. Nucleotide bound Mg^{2+} comes to the enzyme along with the incoming nucleotide, and coordinates with all three phosphates (α, β, and γ) of the incoming nucleotide. The catalytic Mg^{2+} reduces the pKa of 3'-OH group or a H_2O molecule, activates the nucleophile and brings it close to the α-phosphate of the incoming nucleotides. The coordination among nucleotide-bound Mg^{2+}, catalytic Mg^{2+}, water molecules, and acidic residues in the active site helps to stabilize the transition state by neutralizing the developing negative charges. After product formation, it has been proposed that nucleotide bound Mg^{2+} facilitates the release of pyrophosphate (105). Although the general two-metal-ion mechanism has been supported by many crystal structures of DNA polymerases, biochemical experiments are still needed to test this hypothesis. In addition, many details about the activities of the two Mg^{2+} in the active site are still unknown. For example, what is the binding affinity and order of the nucleotide bound Mg^{2+} and catalytic Mg^{2+}? How does each of the two Mg^{2+} affect the whole pathway of nucleotide incorporation, which includes ground state binding, conformational change, chemistry and pyrophosphate release? And how does the Mg^{2+} affect the nucleotide specificity?

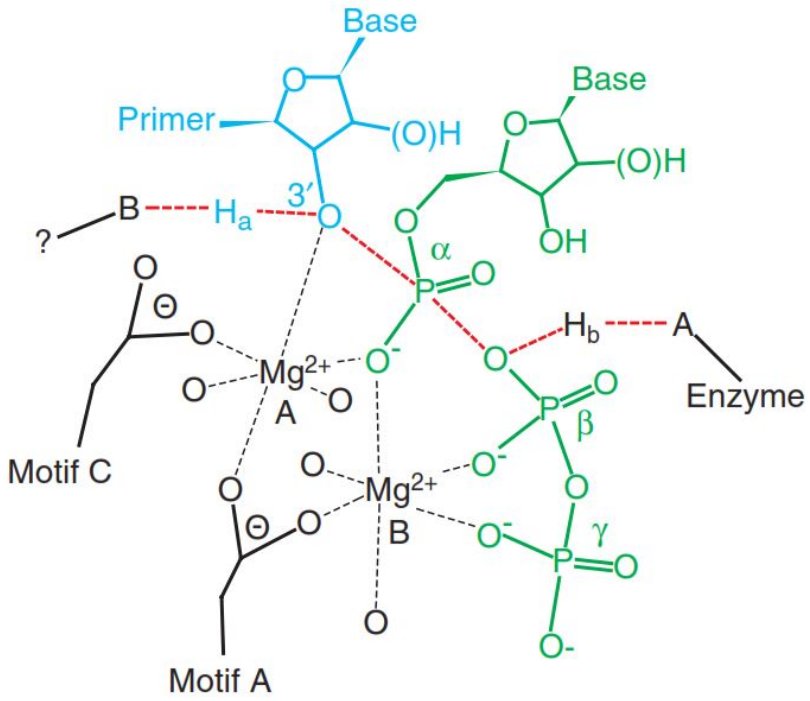

Figure 1.9 The general two-metal-ion mechanism.

Mg^{2+} B (nucleotide bound Mg^{2+}) comes to the active site of the enzyme along with the incoming nucleotide (green color), and coordinates with all three phosphates (α, β, and γ). In addition, it coordinates with an aspartate residue located in motif A and probably water molecules (represented as "O"). Mg^{2+} A (catalytic Mg^{2+}) comes to the active site alone. It coordinates the 3'-OH group, water molecules, α-phosphate of the incoming nucleotides, and aspartate residues located in motif A and motif C. The image is reproduced from Christian Castro, *et al*., 2009 (or reference(106))

Fidelity and processivity are the two important attributes of a DNA polymerase (107). Fidelity is the ability of enzymes to discriminate correct nucleotide from the pool of mismatched nucleotides. Processivity is the ability of the enzyme to perform continuous polymerization without dissociating from the DNA template. The value of processivity is quantified by the number of nucleotides incorporated into the DNA template during a single DNA binding event. Recently, it was reported that the value of HIVRT fidelity is different between some of the *in vitro* studies (around 10^{-4}) and cellular experiments (10^{-5}) (108). Because most of the *in vitro* studies were performed in Mg^{2+} concentrations ranging from 5 to 10 mM (108) and the physiological Mg^{2+} concentration in human lymphocytes was reported as low as 0.25 mM (108-110), whether the concentration of Mg^{2+} affects fidelity is under investigation. In addition, it is reported that HIVRT tends to display low fidelity in the presence of DNA template containing sequence with high probability of termination, suggesting certain correlations exist between the fidelity and the processivity (107). Whether the concentration of Mg^{2+} affects the processivity of HIVRT, or even the possible correlation between the fidelity and the processivity, needs further study.

Recently, the two-metal-ion mechanism was studied by time-resolved X-ray crystallography using DNA polymerase η (111). This polymerase is a repair enzyme that used to replicate at DNA damage caused by ultraviolet light, and it has very slow rate of catalysis (half time is around 1 min). Because the reaction time course in crystal is usually from 20 to 100-fold slower than in solution, each individual step of the reaction could be directly captured by freezing the enzyme (at the temperature of 77K) at different time points. The experiment was performed by first mixing enzyme DNA complex with Ca^{2+} and incoming nucleotide to allow the conformational transition from open to closed. Because Ca^{2+} does not allow the chemistry to occur, the closed conformation upon

nucleotide binding could be directly observed. Then, a large excess of Mg^{2+} was added to solution to replace Ca^{2+} and allow the chemistry to occur. Therefore, the chemistry of the reaction could be directly observed. Surprisingly, a third Mg^{2+} was observed at this step, but appeared only transiently (Figure 1.10). It is proposed that the function of this Mg^{2+} is to neutralize the negative charging at the active site and facilitate the release of pyrophosphate. Later on, a similar phenomenon was also observed in another enzyme (DNA polymerase β) (112), suggesting the third Mg^{2+} may be universal for all polymerases. In their study, the authors found that the third Mg^{2+} appeared after the chemistry step, and it existed only in the correct nucleotide incorporation but not in mismatched incorporation. Because the author only observed pyrophosphorolysis in the correct nucleotide base pairing ended DNA template, they proposed that the function of the third Mg^{2+} is to facilitate the pyrophosphorolysis (112). However, many biochemical experiments are still needed to test the activities of this interesting third Mg^{2+} ion.

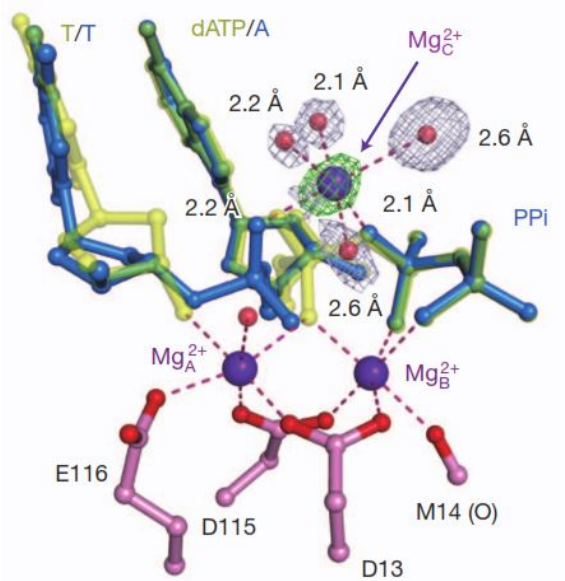

Figure 1.10 The third Mg^{2+} observed by time-resolved X-ray crystallography using DNA polymerase η.

A stereo view of Mg^{2+} ions (shown as purple spheres) in the transition state captured at 230s after Mg^{2+} addition, which contains a mixture of reactant state (yellow sticks) and product state (blue sticks). Nucleotide bound Mg^{2+} and catalytic Mg^{2+} are represented as Mg^{2+}_A and Mg^{2+}_B, respectively. The third Mg^{2+} is presented as Mg^{2+}_C. It coordinates with six ligands, from which four are water molecules (shown as dark orange small sphere). The F_o-F_c map with the Mg^{2+}_C omitted contoured at 4.0 σ (green) and 2F_o-F_c map contoured at 1.5 σ (grey) are overlaid with the ball-stick model. The coordination and hydrogen bonds are shown as dashed purple lines. Residues that are coordinated with Mg^{2+}_A and Mg^{2+}_B are shown as magenta sticks. The picture is reproduced from Teruya Nakamura *et al*., 2012 (or reference (111))

In summary, many cases of NRTI resistance have been reported following long-term use of the drugs (113-118). It is known that there are two mechanisms of resistance: discrimination and excision (84, 86, 96). However, many details regarding the NRTI resistance remain unknown. What is the role of enzyme conformational change in NRTI resistance? How does a given mutation altering discrimination affect the excision? What is the role of pyrophosphorolysis in nucleotide excision? In the following chapters, we will systematically investigate each of these aspects of the mechanisms of NRTI resistance, from which a better understanding about the discrimination and excision will be achieved. In addition, we will investigate the general two-metal-ion mechanism by investigating the role of each Mg^{2+} ion in the nucleotide incorporation pathway, which includes ground state binding, conformational change, chemistry and pyrophosphate release. We will also investigate the difference between the two Mg^{2+} ions including their binding affinities and binding sequence. Furthermore, we will study the effects of Mg^{2+} on the fidelity and processivity of the enzyme, and study the effects of Mg^{2+} on the DNA binding. Finally, we will perform some studies on the possible third Mg^{2+} as well.

Chapter 2: The Roles of HIV Reverse Transcriptase K65R and K66R in NRTIs Resistance by Discrimination Mechanism

2.1 INTRODUCTION

HIV reverse transcriptase (RT) is a RNA- and DNA- dependent polymerase responsible for converting single-stranded viral RNA into double-stranded DNA. Because of its critical role in the process of viral replication, it serves as a key drug target for many inhibitors. Currently, two classes of inhibitors are widely used in clinics: nucleoside reverse transcriptase inhibitors (NRTIs) and non-nucleoside reverse transcriptase inhibitors (NNRTIs). NRTIs are nucleoside analogs, which lack a 3'-hydroxyl group so they prevent the incorporation of the next incoming nucleotide and act as chain terminators. Along with the prolonged usage of NRTIs, drug resistance has appeared. Two mechanisms regarding the NRTIs drug resistance have been reported: discrimination during incorporation and excision after incorporation. The mechanism of discrimination requires that HIVRT evolve to distinguish the inhibitors from the normal nucleotides by changing the relative k_{cat}/K_m values for incorporation. The mechanism of excision relies upon the ability of HIVRT to excise the incorporated NRTIs from the DNA primer, thereby rescuing processive polymerization. Examples of HIVRT mutations that lead to NRTI resistance also could be classified into two classes. Mutations of K65R, M184V, and Q151M are known for selective discrimination against

tenofovir (TFV), lamivudine (3TC), and abacavir (ABC) (61, 71, 100). Thymidine analogue mutations (TAMs) including D67N, K70R, L210W, T215Y/F and K219Q/E increase the rate of nucleotide-dependent excision of all chain terminators, with preference for thymidine analogs zidovudine (AZT) and stavudine (d4T) (119-121).

Lysine 65 is a key residue at the polymerase active site, and it interacts with the γ-phosphate of the incoming nucleotide (58). The mutation of K65R is thought to change this interaction and cause the resistance against tenofovir (TFV) by discriminating against TFV incorporation (122). Recently, it was claimed that the mutation K65R mainly influenced the maximum rate of polymerization (k_{pol}). The analysis of most previous studies was based on an assumption that the binding of TFV is a fast equilibrium step and the chemistry is rate-limiting. However, there was not enough information to define each individual step, including the conformational change and the reverse of the conformational change, which is a major determinant of nucleotide specificity (123, 124). In particular, recent studies have shown that the rate of the reverse of the conformational change relative to the rate of the chemistry step is an important parameter governing specificity (123, 124). When the rate of the chemistry is much greater than the rate of the reverse of the conformational change, specificity constant is governed solely by the rate of the formation of the closed enzyme species ($k_{cat}/K_m = K_1k_2$). When the rate of the chemistry is much slower than the rate of the reverse of the conformational change, the specificity constant is governed by the product of the equilibrium and the rate of the chemistry ($k_{cat}/K_m=K_1K_2k_3$). Therefore, lacking of the information in the conformational change prevents us from thoroughly understanding the mechanism of TFV resistance.

It was reported that the guanidinium planes of the arginines in K65R and R72 stack to form a molecular platform that restrains the conformational change of HIVRT upon TFV incorporation (96). It was also claimed that the main effect of K65R is probably focused on the conformational change of HIVRT (96). Recently, we have developed a system where the conformational change of HIVRT upon nucleotide incorporation could be monitored by a time dependent manner using stopped flow methods. HIVRT was labeled by an MDCC fluorophore (7–diethylamino–3-((((2-maleimidyl)ethyl)amino)carbonyl)coumarin), without changing the kinetics of nucleotide binding and incorporation (123). Using this MDCC-labeled HIVRT, we could measure the effects of the K65R mutation on the conformational change during binding and incorporation of both natural nucleotides and TFV. In addition, it has been reported that the mutation of K65R increases the susceptibility for azidothymidine (AZT) (98, 101). Different from TFV, it is thought that AZT resistance is achieved mainly by the mechanism of excision (125). In this chapter, the effects of the K65R mutation on AZT resistance were also studied.

Lysine 66 is another key residue at the polymerase active site in the fingers domain. It is reported that K66 locates adjacent to the penultimate nucleotide, and that mutations in K66 change the mismatch extension and mis-incorporation rates of HIV-1 reverse transcriptase (97). In this chapter, the role of K66R in TFV and AZT resistance was studied. Therefore, our study not only provided valuable information regarding the AZT and TFV resistance, but also provided insights into the difference between K66R

and K65R in the drug resistance, from which a better understanding for the positions of the residues and their roles in the drug resistance were obtained.

2.2 MATERIALS AND METHODS

Mutagenesis, Expression and Purification of MDCC-labeled HIV Reverse Transcriptase

Mutations of K65R and K66R were introduced to HIV wild type reverse transcriptase using Quickchange Site Directed Mutagenesis kit (Table 2.1), and the results were confirmed by DNA sequencing. The proteins were expressed, purified and labeled as previous described (123). Briefly, the p51 and p66 subunits of the mutants were separately expressed and then cells were combined, lysed, sonicated and the p66/p51 heterodimer was purified. Proteins were first purified by using the tandem Q-Sepharose and Bio-Rex70 columns, and further purified by using single-stranded DNA (ssDNA) affinity column followed by labeling with MDCC. The excess MDCC was removed by chromatography on a Bio-Rex70 column. After purification, the "Coomassie Plus" protein assay was used to determine the purified protein concentrations. Active site titration experiments were also performed to determine the active site concentrations of the purified protein.

Table 2.1 Mutagenesis primer to create mutations of K65R and K66R

Position 65: Lys to Arg

Fwd:

5′-TCCAGTATTTGCCATAAAA**CGT**AAAGACAGTACTAAATGGAGAAA-3′

Rev:

5′-TTTCTCCATTTAGTACTGTCTTT**ACG**TTTTATGGCAAATACTGGA-3′

Position 66: Lys to Arg

Fwd: 5′-GTATTTGCCATAAAGAAA**CGT**GACAGTACTAAATGGAGA-3′

Rev: 5′-TCTCCATTTAGTACTGTC**ACG**TTTCTTTATGGCAAATAC-3′

Forward (Fwd) and reverse (Rev) primers are used to introduce mutagenesis. Mutated codons are shown in bold and underlined.

Prepare DNA Substrates for Kinetic Studies

The 25/45nt DNA substrates were purchased from Integrated DNA Technologies (Table 2.2). The oligonucleotides were annealed by heating at 95° for 5 minutes and then slow cooling to room temperature. The 25nt oligonucleotide was labeled at the 5' end by γ-^{32}P for use in the quench flow kinetic assays.

Table 2.2 DNA substrates for kinetic studies

25/45-A

25nt: 5′-GCCTCGCAGCCGTCCAACCAACTCA-3′

45nt: 5′-CGGAGCGTCGGCAGGTTGGTTGAGT**A**GCAGCTAGGTTACGGCAGG-3′

25ddA/45-A

25nt: 5′-GCCTCGCAGCCGTCCAACCAACTCA$_{dd}$-3′

45nt: 5′-CGGAGCGTCGGCAGGTTGGTTGAGT**A**GCAGCTAGGTTACGGCAGG-3′

Quench Flow Kinetic Assays

Quench flow experiment was performed by rapidly mixing preformed a enzyme-DNA complex (150 nM enzyme and 100 nM ^{32}P labeled 25/45nt DNA template) with various concentrations of nucleotides or NRTIs at 37° using KinTek RQF-3 instrument (KinTek Corp., Austin, TX). The reaction was quenched by the addition of 0.5 M EDTA at varying time points. Products were collected and separated on 15% denaturing PAGE (acrylamide (1:19 bisacrylamide), 7M Urea) and quantified using a Typhoon scanner in ImageQuant 6.0 software (Molecular® Dynamics).

Stopped Flow Kinetic Assays

The stopped flow measurement was performed by rapidly mixing 100 nM MDCC-labeled HIVRT-DNA complex with various concentrations of nucleotide or NRTIs. All specified concentrations are after mixing at a 1:1 ratio. The time dependent fluorescence change upon nucleotides or NRTIs binding was monitored by AutoSF-120 stopped-flow instrument (KinTek Corp., Austin, TX) by exciting the fluorophore at 425 nm and monitoring the fluorescence change at 475 nm using a single band-pass filter with a 25 nm bandwidth (Semrock).

Global Analysis of Kinetic Data

The kinetic constants defining nucleotide binding and incorporation obtained by globally fitting data to the model shown in scheme 2.1 by *KinTek Explorer* software (KinTek-Corp. Austin, TX). FitSpace confidence contour analysis was performed for each analysis to assess standard errors on fitted parameters.

2.3 RESULTS

dATP and Tenofovir Incorporation by HIV-1 Wild Type Reverse Transcriptase

The time dependence of fluorescence change after mixing an enzyme-DNA complex with various concentrations of dATP was recorded by stopped flow (Figure 2.1A). The decrease in fluorescence indicates a conformational change of HIVRT from an open to a closed state upon dATP binding. The recovery of fluorescence provides a measurement of the return to the open state after chemistry and pyrophosphate release. Because the rate of pyrophosphate release is usually fast, the rise of fluorescence could also be used to define the rate of the chemistry (126). The maximum rate of the conformational change (k_2 value in the scheme 2.1) was measured by monitoring the time course of fluorescence change at saturating nucleotide concentration. However, the value of k_2 at 37° could not be accurately determined because it was too fast to measure directly. To obtain a better estimate of k_2, stopped flow experiments were first performed at lower temperatures at 10, 18, and 25°, respectively (Figure 2.2). Then, the k_2 value at 37° was obtained by extrapolation using the Arrhenius equation. The k_2 value for dATP incorporation was $1450 \pm 350\ s^{-1}$ (Table 2.1).

In addition, rapid quench-flow experiments were also performed to define the apparent binding of dATP and the rate of the chemistry ($K_{d,app}$ and k_{pol}, respectively). Then, two experiments were globally fit to the model shown in the Scheme 2.1 to define the rate constants governing each individual step of the dATP incorporation. The specificity constant (k_{cat}/K_m) governing dATP incorporation by wild type HIVRT was calculated as 8.2 $\mu M^{-1}s^{-1}$. In addition, the results from quench-flow were also analyzed by

conventional fitting to estimate the specificity constants ($k_{cat}/K_m = k_{pol}/K_{d,app}$) governing dATP incorporation. The concentration dependent nucleotide incorporation was first fit to single exponential equation (equation 2.1) to obtain the observed rate for each concentration. Then, the observed rates as a function of nucleotide concentration were plotted using hyperbola equation (equation 2.2) to estimate the maximal rate of polymerization (k_{pol}) and apparent binding ($K_{d,app}$) of dATP. The $k_{pol}/K_{d,app}$ value was obtained as 11.7 $\mu M^{-1}s^{-1}$, which is consistent with the result from global fitting. The comparable rates of two analysis indicates that the conventional fitting was still valid in the estimation of specificity constant governing the dATP incorporation.

Scheme 2.1 The Complete Model of Nucleotide Incorporation

$$\overset{open}{ED_n} + dNTP \underset{}{\overset{K_1}{\rightleftharpoons}} \overset{open}{ED_n dNTP} \underset{k_{-2}}{\overset{k_2}{\rightleftharpoons}} \overset{closed}{FD_n dNTP} \underset{k_{-3}}{\overset{k_3}{\rightleftharpoons}} \overset{closed}{FD_{n+1}PP_i} \xrightarrow{fast} \overset{open}{ED_{n+1}} + PP_i$$

Equation 2.1 Single Exponential Equation

$$Y = A \cdot (1 - e^{-k_{obs} \cdot t})$$

Equation 2.2 Hyperbola Equation

$$v = \frac{k_{pol} \cdot [S]}{K_{d,app} + [S]}$$

Similar experiments and analysis were performed for TFV incorporation (Figure 2.1C and 2.1D). The results showed that TFV does not affect the rate of the

conformational change (k_2) but affects the rate of the chemistry (k_3). It decreases the k_3 value by 6-fold (from 30 s^{-1} to 5 s^{-1}). Compared with the natural nucleotide (dATP), the specificity constant (k_{cat}/K_m) for TFV incorporation is also decreased by about 4-fold (to 2.1 $\mu M^{-1}s^{-1}$) (Table 2.1). Therefore, HIV-1 wild type RT has about 4-fold discrimination against TFV incorporation, and the main difference between dATP and TFV incorporation is on the rate of chemistry (~6-fold difference).

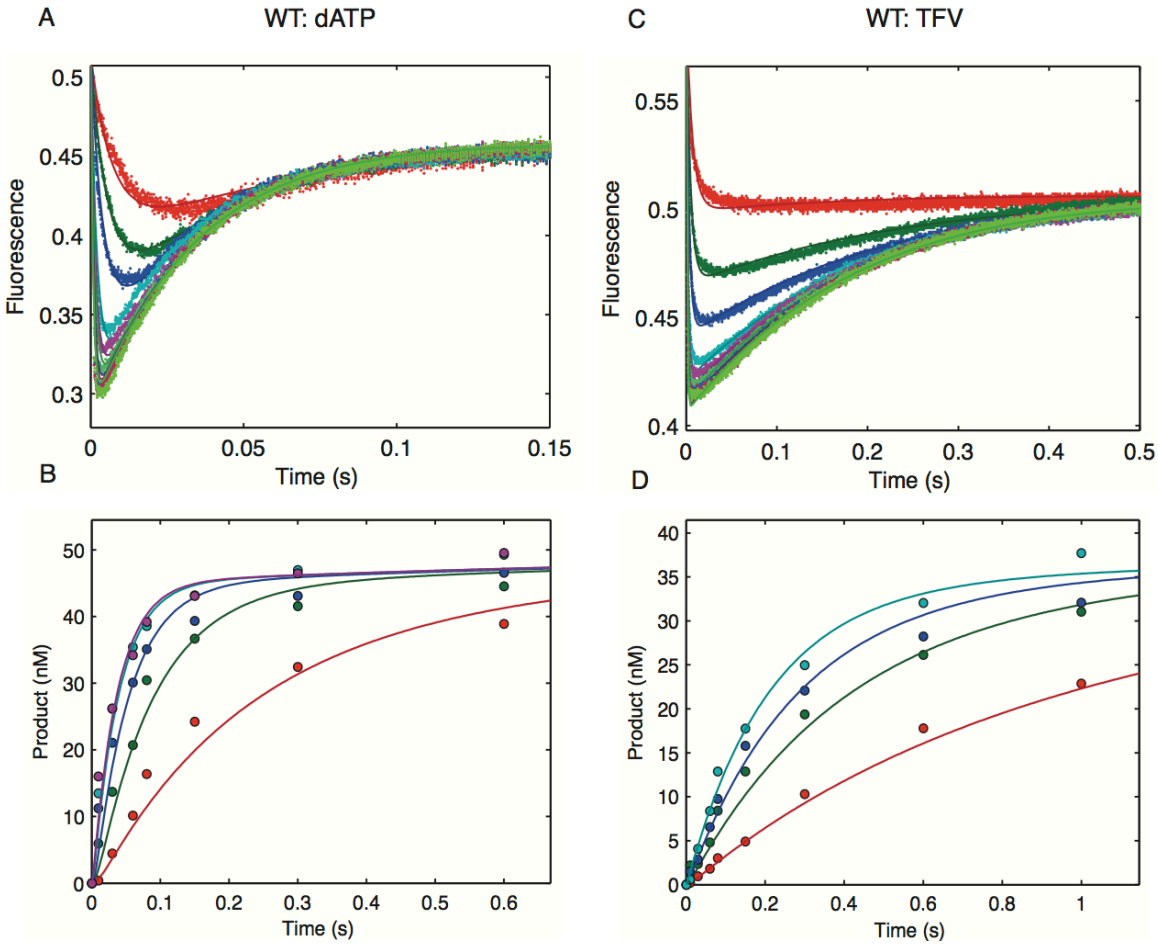

(Figure 2.1)

Figure 2.1 Global fitting of dATP and TFV binding and incorporation by MDCC-labeled HIVRT.

The stopped flow experiments were performed by rapidly mixing various concentrations (2.5, 5, 10, 20, 30, 40, 60, 80, 100 μM) of dATP (A) or TFV (C) with a preformed enzyme-DNA complex (100 nM MDCC-labeled HIVRT and 150 nM DNA). The time dependence of the fluorescence change was then monitored using stopped flow instrument. The rapid chemical quench flow experiments were performed by rapidly mixing various concentrations (0.5, 2, 5, 20, 40 μM) of dATP (B) or (0.5, 2, 5, 40 μM) TFV (D) with a preformed enzyme-DNA complex (100 nM DNA and 150 nM HIVRT). Global fitting was performed independently for dATP (A and B) and TFV (C and D).

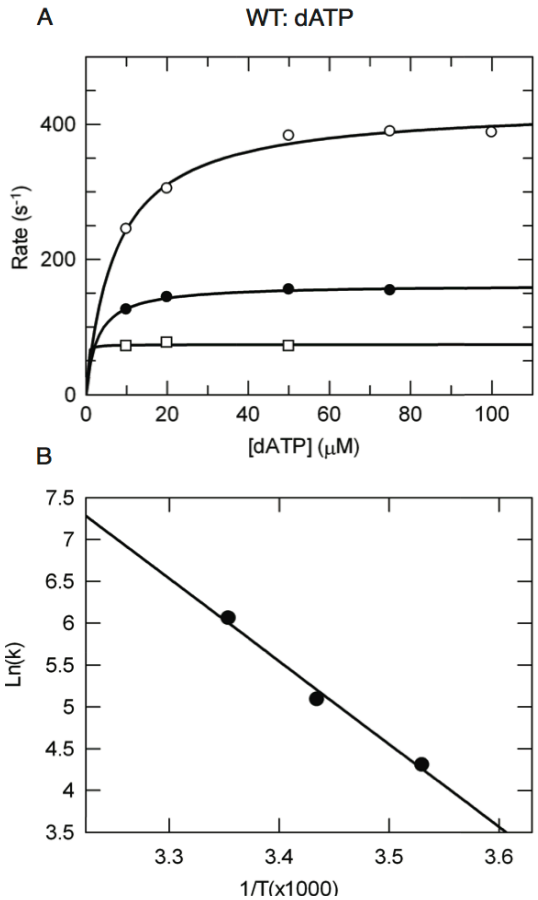

Figure 2.2 Temperature dependence of stopped flow fluorescence measuring the HIVRT conformational change upon dATP binding.

(A) A pre-incubated complex of 50 nM HIVRT MDCC and 75 nM 25/45 DNA was rapidly mixed with various concentrations of dATP (2.5, 5, 7.5, 10, 20, 50, 75, 100 and 200 μM) at 10° (□), 18° (●), 25° (○). The nucleotide concentration dependence of the rate of the fluorescence change upon dATP binding was fit to a hyperbolic equation to obtain the maximum rate of the conformational change (k_2) at low temperatures including 10, 18, and 25°. The k_2 values were obtained as 74 ± 5 s^{-1}, 162 ± 2 s^{-1} and 427 ± 9 s^{-1}, respectively. (B) The temperature dependence of k_2 was analyzed by Arrhenius plot to estimate the maximum rate of the conformational change at 37°.

Table 2.3 Kinetic Constants for TTP, AZT, dATP and TFV Incorporation by K65R, K66R and Wild-Type HIV RT

Enzyme	dNTP	$1/K_1$ (μM)	k_2(s^{-1})	k_{-2} (s^{-1})	K_2	k_3 (s^{-1})
WT[a]	TTP	310 ± 10	2700 ± 100	3.9 ± 0.2	690 ± 67	34 ± 0.5
	AZTTP	110 ± 10	1500 ± 100	15.0 ± 0.5	100 ± 10	30 ± 0.4
K66R	TTP	304 ± 2.7	2680 ± 43	3 ± 0.1	865 ± 11	25 ± 0.4
	AZTTP	60.3 ± 1.7	685 ± 14	40 ± 1	17 ± 0.4	15 ± 0.4
K65R	TTP	207 ± 1	1020 ± 19	1.8 ± 0.1	551 ± 11	4 ± 0.1
	AZTTP	152 ± 16	1560 ± 147	8.3 ± 0.2	188 ± 18	0.5 ± 0.1
WT	dATP	46 ± 0.5	1450 ± 354	77 ± 1.1	19 ± 4.6	30 ± 0.5
	TFV	32 ± 0.7	1410 ± 26	105 ± 1.9	13.4 ± 0.3	5 ± 0.4
K66R	dATP	36 ± 0.4	1450 ± 219	77 ± 1	19 ± 2.9	28 ± 0.3
	TFV	60 ± 1.4	1250 ± 28	111 ± 2.3	11.3 ± 0.3	6 ± 0.5
K65R	dATP	31 ± 0.6	615 ± 28	26 ± 0.5	23.3 ± 1	6 ± 0.4
	TFV	34 ± 5	700 ± 88	13 ± 0.6	54.5 ± 7	0.07 ± 0.01

[a]Data from *Matthew W. Kellinger and Kenneth A. Johnson* (2011) (reference (126))

Table 2.4 Specificity, Discrimination and Resistance for K65R, K66R and Wild-Type HIVRT

Enzyme	dNTP	K_m (μM)	k_{cat} (s^{-1})	k_{cat}/K_m ($\mu M^{-1}s^{-1}$)	D[b]	R[c]
WT[a]	TTP	4.7 ± 0.2	34 ± 1.8	7.3 ± 0.5	0.9± 0.1	1
	AZTTP	3.5 ± 0.3	29 ± 2.7	8.4 ± 1		
K66R	TTP	3.4 ± 0.1	25 ± 0.5	7.3 ± 0.2	2.4 ± 0.1	2.7 ± 0.3
	AZTTP	4.7 ± 0.1	14 ± 0.3	3 ± 0.1		
K65R	TTP	1.2 ± 0.1	4 ± 0.1	3.3 ± 0.1	6 ± 0.9	6.7 ± 1.2
	AZTTP	0.9 ± 0.1	0.5 ± 0.1	0.6 ± 0.1		
WT	dATP	3.5 ± 0.7	28 ± 9.5	8.2 ± 3.2	3.9 ± 1.5	1
	TFV	2.4 ± 0.1	5 ± 0.1	2.1 ± 0.1		
K66R	dATP	2.7 ± 0.4	26 ± 5.5	9.8 ± 2.5	8.9 ± 2.4	2.3 ± 1
	TFV	5.2 ± 0.2	5.9 ± 0.2	1.1 ± 0.1		
K65R	dATP	1.6 ± 0.1	5.3 ± 0.3	3.3 ± 0.2	30 ± 3.2	7.7 ± 3.1
	TFV	0.6 ± 0.1	0.07 ± 0.01	0.11 ± 0.01		

Note: [a] Data from *Matthew W. Kellinger and Kenneth A. Johnson* (2011) (reference (126));

[b]Discrimination was calculated as $D^b=(k_{cat}/K_m)_{dNTP}/(k_{cat}/K_m)_{Drug}$;

[c]Resistance was calculated as: $R^c=D_{mutant}/D_{wild\text{-}type}$

$K_m=(k_2k_3+k_{-1}(k_{-2}+k_3))/k_1(k_2+k_{-2}+k_3)$

$k_{cat}=k_2k_3/(k_2+k_{-2}+k_3)$

$k_{cat}/K_m=k_1k_2k_3/(k_2k_3+k_{-1}(k_{-2}+k_3))$

dATP and Tenofovir Incorporation by HIV-1 K65R and K66R Mutants.

The time dependence of fluorescence change upon dATP binding and incorporation by HIVRT mutants (K65R and K66R) were also monitored by stopped flow experiments (Figure 2.3 and 2.4). The maximum rates of the conformational change at 37° were calculated similarly as shown above (Figure 2.5 and 2.6), and the k_2 values for dATP incorporation by K65R and K66R mutants were 615 s^{-1} and 1450 s^{-1}, respectively (Table 2.1). Compared to the wild type RT, K65R decreases the k_2 value by about 2-fold upon dATP binding, but it also decreases the reverse rates (k_{-2}) of the conformational change by about 3-fold (from 77s^{-1} to 26 s^{-1}) (Table 2.1). Therefore, K65R has no significant effect on the equilibrium constant (K_2) of the conformational change. Similarly, K66R has no significant effect on the conformational change upon dATP binding. For TFV incorporation, K65R decreases the forward rate (k_2) by about 2-fold and the reverse rate (k_{-2}) of the conformational change by about 8-fold, which increases the equilibrium constants (K_2) by 4-fold (Table 2.1). Therefore, K65R actually favors the conformational change of RT upon TFV binding as compared with the wild type enzyme. The results from our study disprove the previous hypothesis that K65R restrains the conformational change of HIVRT upon TFV incorporation due to the rigid molecular platform formed by K65R and R72. K66R slightly weakens the binding of TFV by 2-fold through increasing the value of $1/K_1$ (from 32 μM to 60 μM).

Rapid chemical quench flow experiments were also performed for two mutants and then globally fit with stopped flow experiments to define each rate constant governing dATP and TFV incorporation (Figure 2.3 and 2.4). The rates of chemistry

were calculated and compared with wild type RT. As a result, K65R decreases the rate of chemistry (k_3) for dATP and TFV incorporation by about 5-fold and 70-fold, respectively. K66R shows a comparable k_3 for both dATP and TFV incorporation. Therefore, K65R greatly affect TFV incorporation by decreasing the rate of the chemistry, and K66R has no obvious effect on the chemistry step of TFV incorporation. The result from our study also disproves the hypothesis that the main effect of K65R is on the conformational change of HIVRT upon nucleotide or TFV incorporation.

Specificity Constants Governing dATP and TFV Incorporation

The specificity constants (k_{cat}/K_m) governing dATP and TFV incorporation were calculated. For dATP incorporation, K65R decreases the k_{cat}/K_m value by about 2.5-fold, and K66R mutant shows a comparable k_{cat}/K_m value with that of wild type RT. For TFV incorporation, the mutations of K65R and K66R decrease the k_{cat}/K_m by about 20- and 2-fold, respectively. Therefore, the discrimination values against TFV by two mutants were calculated based on the k_{cat}/K_m values and the results show that K65R and K66R have 30-fold and 9-fold discrimination against TFV incorporation, respectively (Table 2.2). Worth of mentioning, wild type RT also has a 4-fold discrimination against TFV incorporation. Therefore, the drug resistances against TFV incorporation by two mutants are actually not very high, with 7.7-fold and 2.3-fold resistance against TFV incorporation for K65R and K66R, respectively.

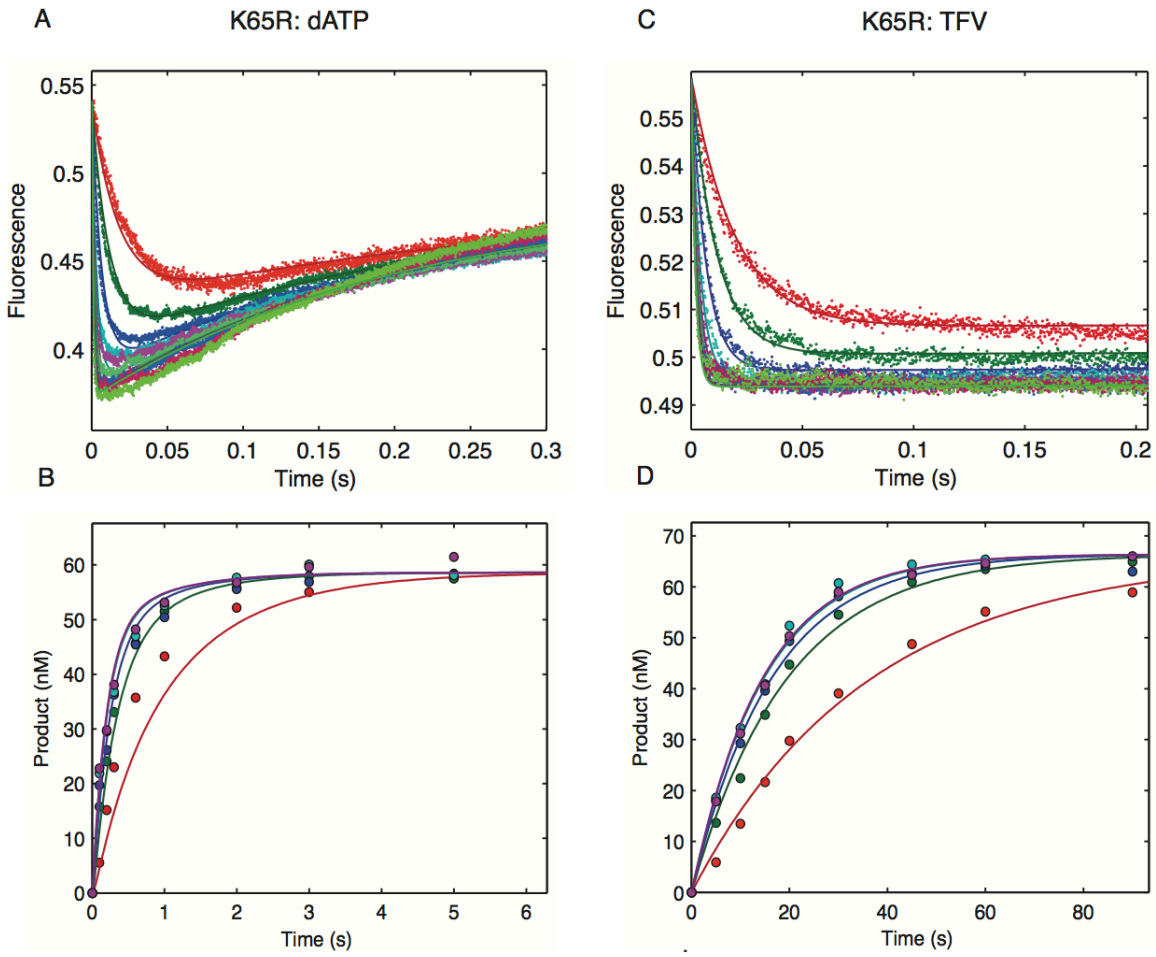

Figure 2.3 Global fitting of dATP and TFV binding and incorporation by MDCC-labeled HIV-1 K65R mutant.

The time dependence of the fluorescence change upon dATP and TFV binding was monitored by stopped flow experiments. The experiments were performed by rapidly mixing various concentrations (2.5, 5, 10, 20, 30, 40, 60, 80, 100 μM) of dATP (A) or TFV (C) with a preformed enzyme-DNA complex (100 nM MDCC-labeled HIV-1 K65R mutant and 150 nM DNA). The time dependence of the fluorescence change was then monitored by the excitation of MDCC fluorophore at 425 nm and monitoring the emission at 475 nm. The rapid chemical quench flow experiments were performed by mixing various concentrations (0.5, 2, 5, 20, 40 μM) of dATP (B) or TFV (D) with a preformed enzyme-DNA complex (100 nM DNA and 150 nM HIV-1 K65R mutant). Global fitting was performed independently for dATP (A and B) and TFV (C and D).

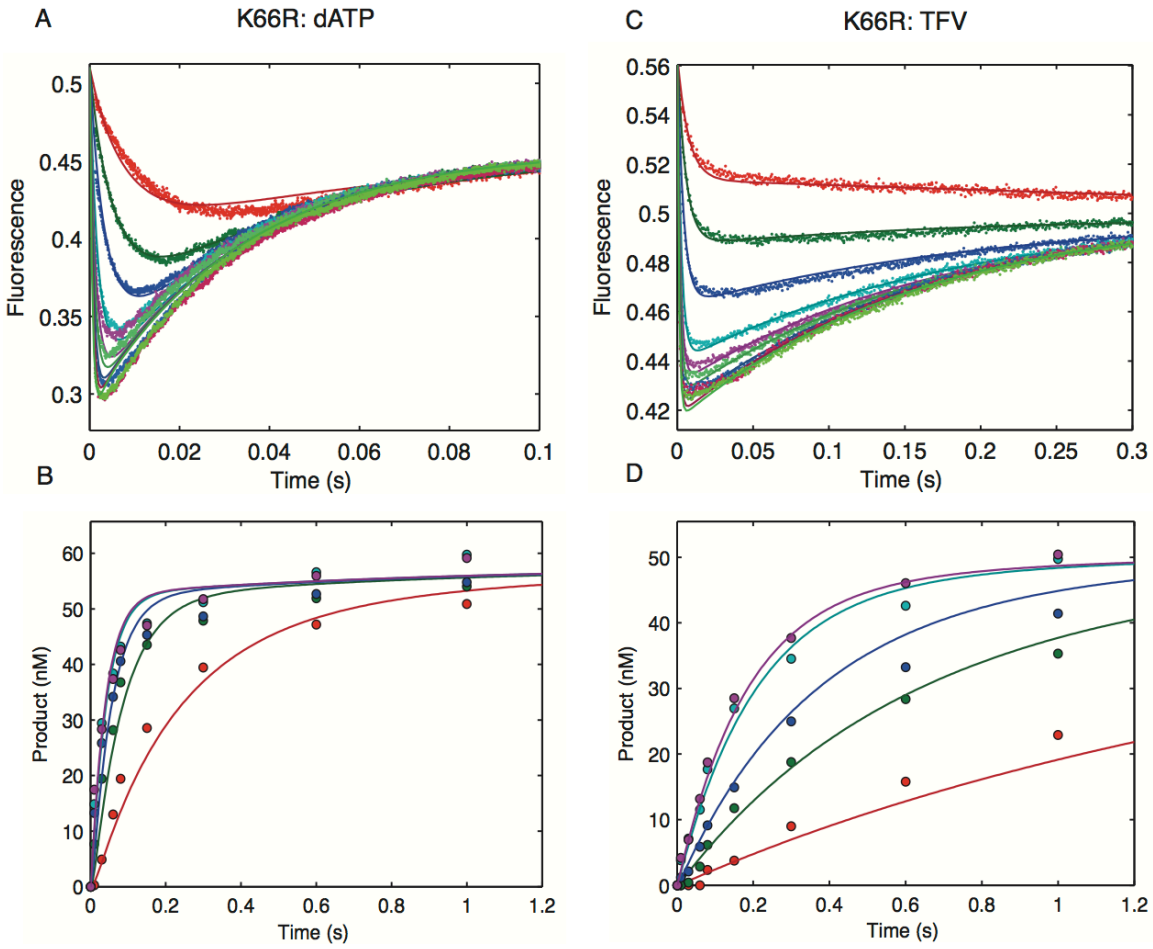

Figure 2.4 Global fitting of dATP and TFV binding and incorporation by MDCC-labeled HIV-1 K66R mutant.

The time dependence of the fluorescence change upon dATP and TFV binding was monitored by stopped flow experiments. The experiments were performed by rapidly mixing various concentrations (2.5, 5, 10, 20, 30, 40, 60, 80, 100 μM) of dATP (A) or TFV (C) with a preformed enzyme-DNA complex (100 nM MDCC-labeled HIV-1 K65R mutant and 150 nM DNA). The time dependence of the fluorescence change was then monitored by the excitation of MDCC fluorophore at 425 nm and monitoring the emission at 475 nm. The rapid chemical quench flow experiments were performed by mixing various concentrations (0.5, 2, 5, 20, 40 μM) of dATP (B) or TFV (D) with a preformed enzyme-DNA complex (100 nM DNA and 150 nM HIV-1 K65R mutant). Global fitting was performed independently for dATP (A and B) and TFV (C and D).

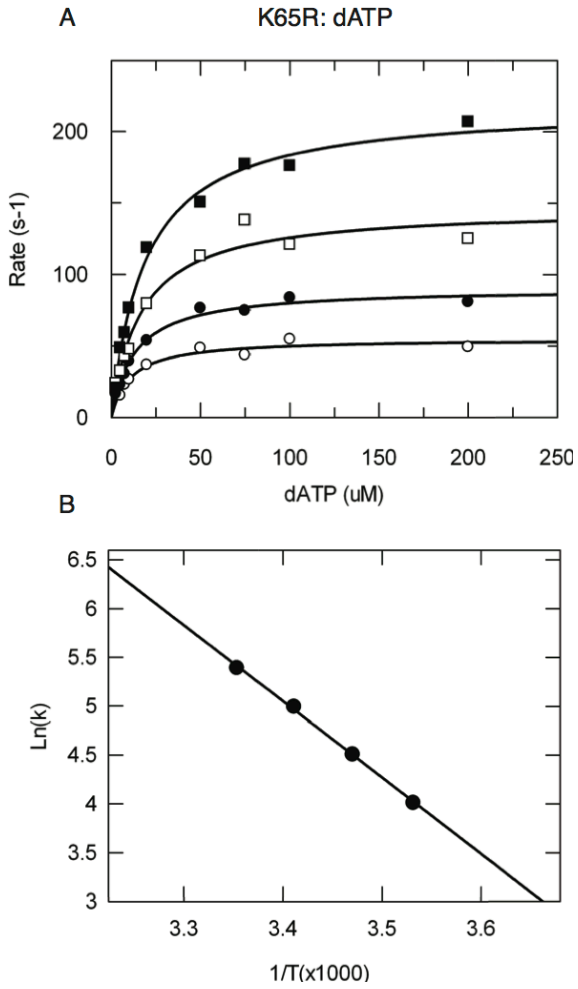

Figure 2.5 Temperature dependence of the HIV K65R RT-MDCC conformational change rate upon dATP binding.

(A) A pre-incubated complex of 50 nM HIV RT MDCC and 75 nM 25/45 DNA was rapidly mixed with various concentrations of dATP (2.5, 5, 7.5, 10, 20, 50, 75, 100 and 200 μM) at 10° (○), 15° (●), 20° (□), 25° (■). The concentration dependence of the rate of the fluorescence decrease upon nucleotide binding was fit to a hyperbolic equation to obtain the maximum rate of the conformational change (k_2) at each temperature resulting in rates of 55 ± 3 s^{-1}, 91 ± 3 s^{-1}, 147 ± 8 s^{-1} and 219 ± 6 s^{-1}, respectively. (B) The temperature dependence of k_2 was analyzed by Arrhenius plot to estimate the maximum rate of the conformational change at 37°.

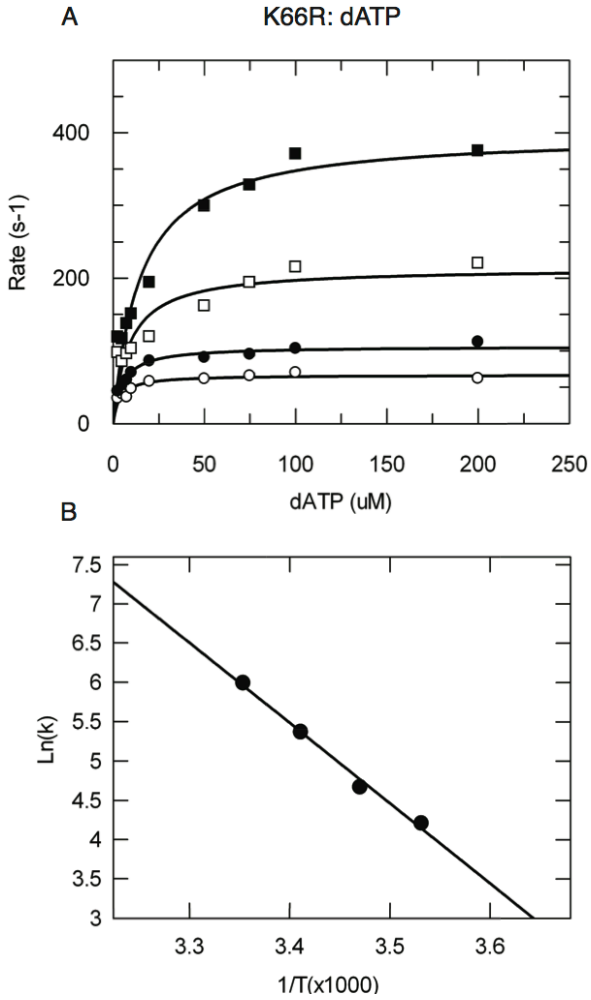

Figure 2.6 Temperature dependence of the HIV K66R RT-MDCC conformational change rate upon dATP binding.

(A) A pre-incubated complex of 50 nM HIV RT MDCC and 75 nM 25/45 DNA was rapidly mixed with various concentrations of dATP (2.5, 5, 7.5, 10, 20, 50, 75, 100 and 200 μM) at 10° (○), 15° (●), 20° (□), 25° (■). The concentration dependences of the rate of the fluorescence decrease upon nucleotide binding was fit to a hyperbolic equation to obtain the maximum rate of the conformational change (k_2) at each temperature resulting in rates of 67 ± 2.8 s^{-1}, 106 ± 3 s^{-1}, 214 ± 17 s^{-1} and 399 ± 24 s^{-1}, respectively. (B) The temperature dependence of k_2 was analyzed by Arrhenius plot to estimate the maximum rate of the conformational change at 37°.

TTP and AZT Incorporation by HIV-1 K65R and K66R Mutants

The kinetics of TTP and AZT incorporation by HIV-1 K65R and K66R mutants were also monitored by stopped-flow and rapid chemical quench-flow methods (Figure 2.7 and 2.8). The data analysis was performed similarly as described above. In addition, the maximum rates of the conformational change at 37° were also calculated as shown above (Figure 2.9 and 2.10). The two experiments were then globally fit to better define each kinetic parameter governing TTP or AZT incorporation shown in scheme 2.1. The results showed that K65R does not affect the equilibrium constant (K_2) governing the conformational change of HIVRT upon TTP incorporation but it affects the rate of chemistry (k_3) by about 8.5-fold. K66R does not affect TTP incorporation through ground state binding to the chemistry (Table 2.1). For AZT incorporation, K65R increase the K_2 by about 2-fold and decreases the k_3 by 60-fold. K66R decreases the K_2 value by about 6-fold and the k_3 value by 2-fold.

Therefore, K65R affects both TTP and AZT incorporation. It affects the TTP incorporation through decreasing the rate of the chemistry by about 9-fold, and affects the AZT incorporation through decreasing the rate of the chemistry by 60-fold. The results from our study demonstrate again that K65R mainly affects the rate of chemistry of nucleotide incorporation, especially the chemistry of AZT incorporation. K66R does not affect TTP incorporation, but it slightly affects AZT incorporation by weakening its binding.

Specificity Constants Governing TTP and AZT Incorporation

The specificity constant (k_{cat}/K_m), discrimination and drug resistance against AZT incorporation were then calculated. The discriminations against AZT incorporation by K65R and K66R are 6 and 2.4, respectively. Because the discrimination against AZT incorporation by the wild type RT is close to 1, the final drug resistance against AZT incorporation by K65R and K66R are 6.7 and 2.7, respectively. Therefore, the drug resistances for AZT and TFV are actually comparable.

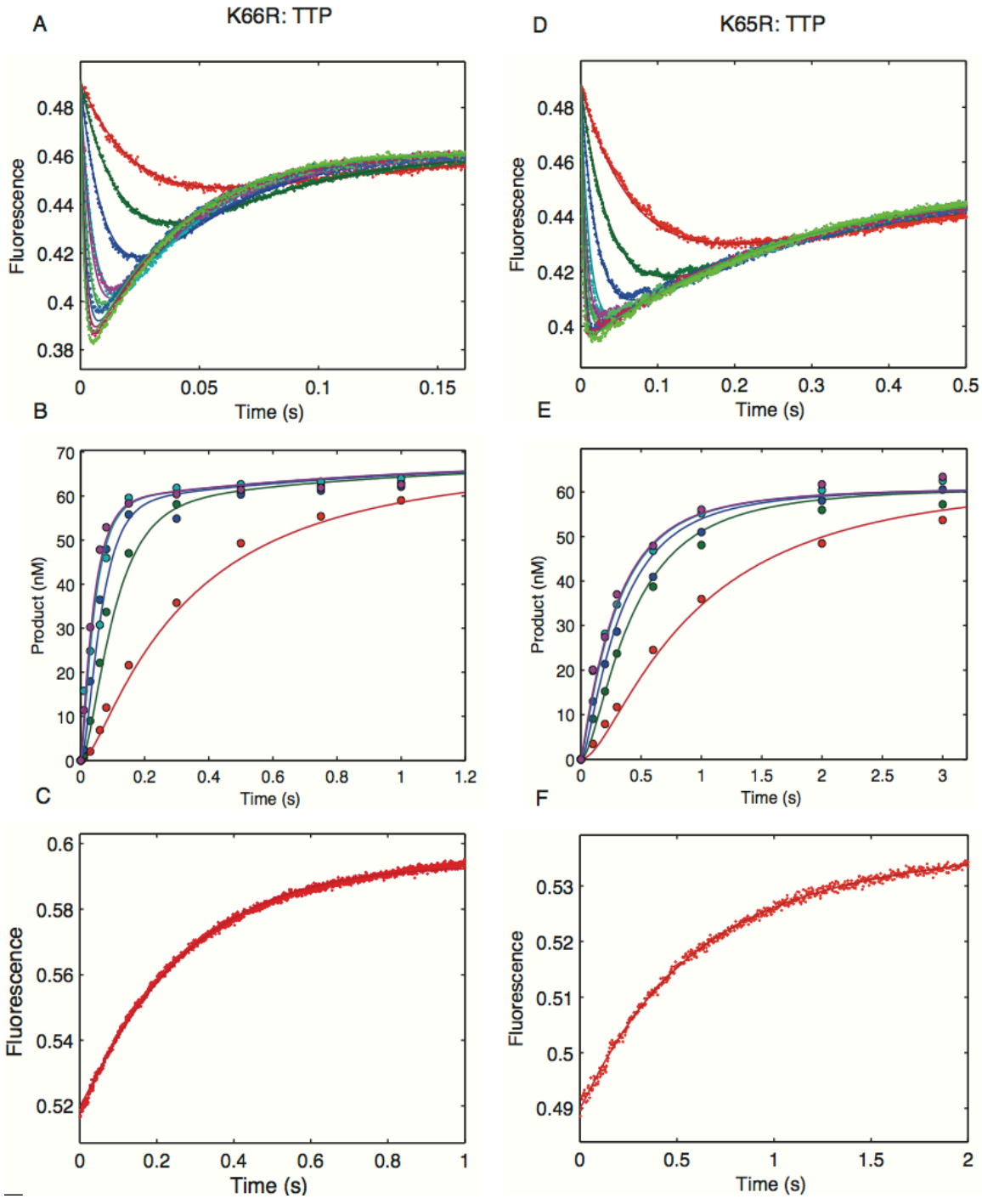
A
K66R: TTP
Fluorescence
Time (s)
B
Product (nM)
Time (s)
C
Fluorescence
Time (s)
D
K65R: TTP
Fluorescence
Time (s)
E
Product (nM)
Time (s)
F
Fluorescence
Time (s)

(Figure 2.7)

Figure 2.7 Global fitting of TTP binding and incorporation by MDCC-labeled HIV-1 K66R and K65R mutants.

The time dependence of the fluorescence change upon TTP binding was monitored by stopped flow experiments. The experiments (A and D) were performed by rapidly mixing various concentrations (2.5, 5, 10, 20, 30, 40, 60, 80, 100 μM) of TTP with preformed enzyme-DNA complex (100 nM MDCC-labeled HIV-1 K65R mutant and 150 nM DNA). The time dependence of the fluorescence change was then monitored by the excitation of MDCC fluorophore at 425 nm and monitoring the emission at 475 nm. The rapid chemical quench flow experiments (B and E) were performed by rapidly mixing various concentrations (0.5, 2, 5, 20, 40 μM) of TTP with preformed enzyme-DNA complex (100 nM DNA and 150 nM HIV-1 K65R mutant). The nucleotide off-rate experiments (C and F) were performed by rapidly mixing preformed enzyme-DNA_{dd}-dNTP complex (200 nM HIV RT-MDCC, 300 nM 25 ddA/45-nt, 5 μM nucleotides) with a nucleotide trap consisting of 5 μM unlabeled enzyme-DNA complex. The rates of the reverse of the conformational change were measured by monitoring the fluorescence change from its closed state to the open state upon the addition of the nucleotide trap. Global fitting was performed independently for K66R (A-C) and K65R (D-F).

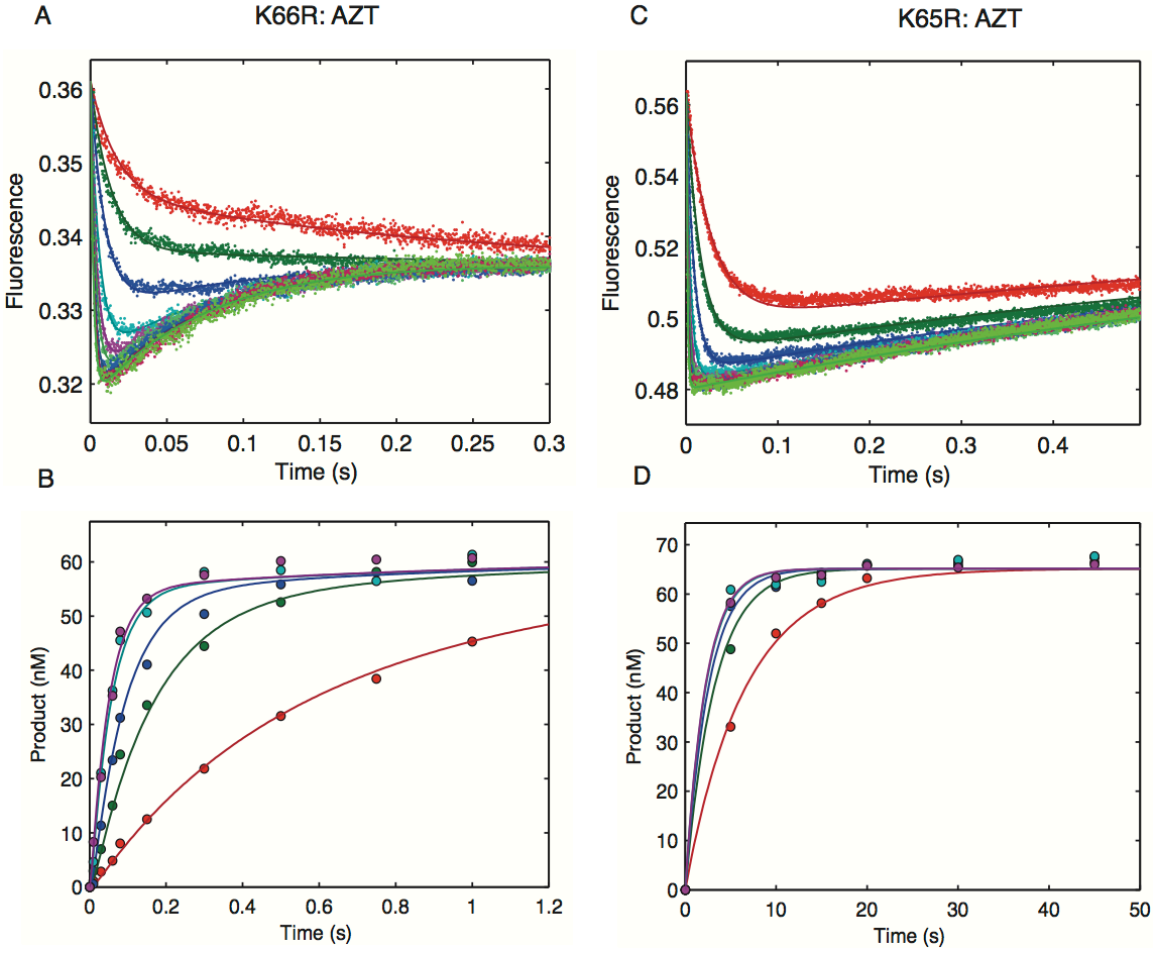

Figure 2.8 Global fitting of AZT binding and incorporation by MDCC-labeled HIV-1 K66R and K65R mutants.

The time dependence of the fluorescence change upon AZT binding was monitored by stopped flow experiments, and the experiments (A and C) were performed by rapidly mixing various concentrations (2.5, 5, 10, 20, 30, 40, 60, 80, 100 μM) of AZT with preformed enzyme-DNA complex (100 nM MDCC-labeled HIV-1 K65R mutant and 150 nM DNA). The time dependence of the fluorescence change was then monitored by the excitation of MDCC fluorophore at 425 nm and monitoring the emission at 475 nm. The rapid chemical quench flow experiments (B and D) were performed by rapidly mixing various concentrations (0.5, 2, 5, 20, 40 μM) of AZT with preformed enzyme-DNA complex (100 nM DNA and 150 nM HIV-1 K65R mutant). Global fitting was performed independently for K66R (A and B) and K65R (C and D).

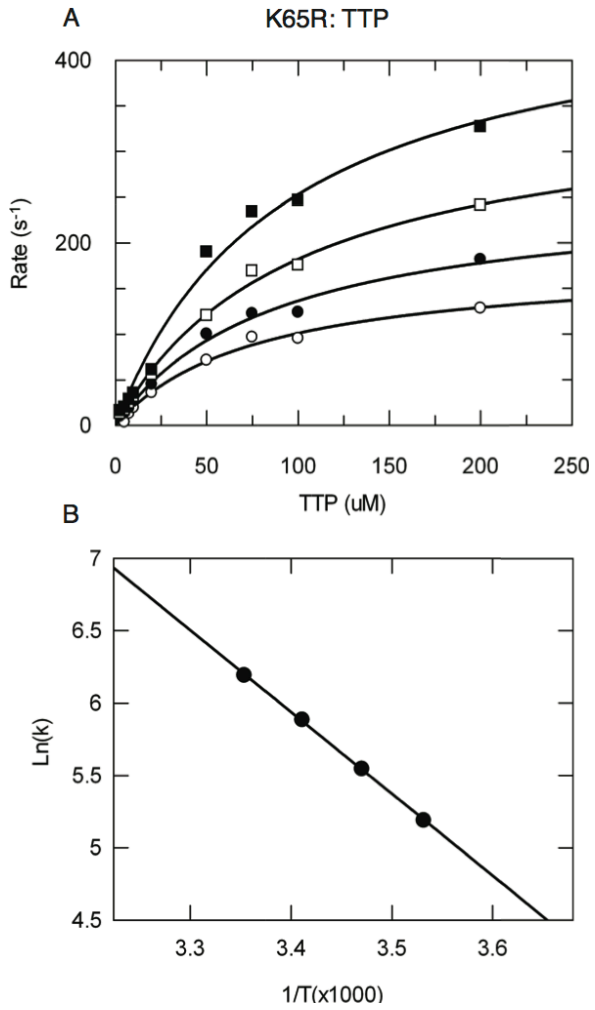

Figure 2.9 Temperature dependence of the HIV K65R RT-MDCC conformational change rate upon TTP binding.

(A) A pre-incubated complex of 50 nM HIV RT MDCC and 75 nM 25/45 DNA was rapidly mixed with various concentrations of TTP (2.5, 5, 7.5, 10, 20, 50, 75, 100 and 200 μM) at 10° (○), 15° (●), 20° (□), 25° (■). The concentration dependences of the rate of the fluorescence decrease upon nucleotide binding was fit to a hyperbolic equation to obtain the maximum rate of the conformational change (k_2) at each temperature resulting in rates of 179 ± 13 s^{-1}, 256 ± 17 s^{-1}, 360 ± 20 s^{-1} and 488 ± 48 s^{-1}, respectively. (B) The temperature dependence of k_2 was analyzed by Arrhenius plot to estimate the maximum rate of the conformational change at 37°.

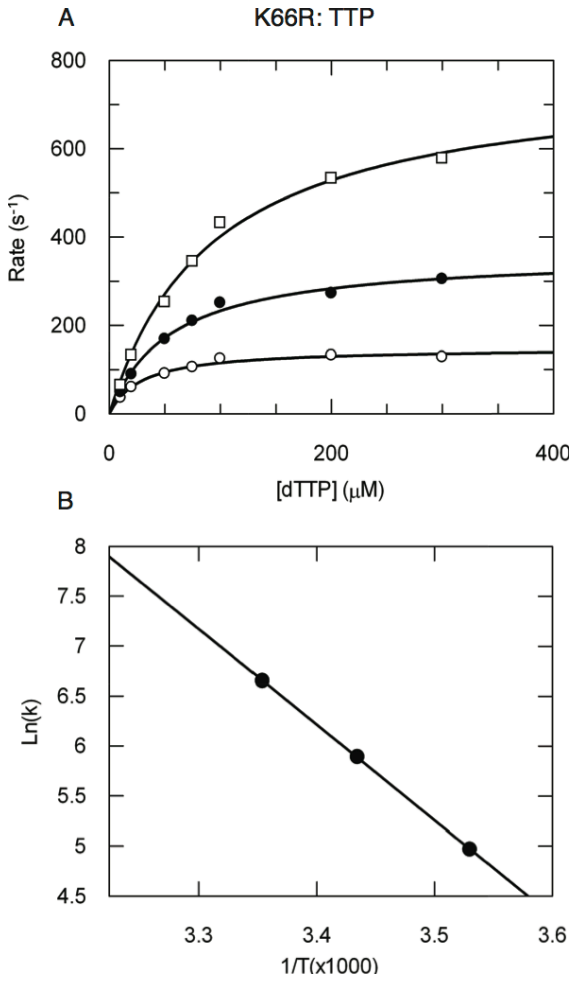

Figure 2.10 Temperature dependence of the HIV K66R RT-MDCC conformational change rate upon TTP binding.

(A) A pre-incubated complex of 50 nM HIV RT MDCC and 75 nM 25/45 DNA was rapidly mixed with various concentrations of TTP (2.5, 5, 7.5, 10, 20, 50, 75, 100 and 200 μM) at 10° (○), 18° (●), 25° (□). The concentration dependences of the rate of the fluorescence decrease upon nucleotide binding was fit to a hyperbolic equation to obtain the maximum rate of the conformational change (k_2) at each temperature resulting in rates of 149 ± 6 s^{-1}, 362 ± 15 s^{-1} and 772 ± 37 s^{-1}, respectively. (B) The temperature dependence of k_2 was analyzed by Arrhenius plot to estimate the maximum rate of the conformational change at 37°.

Activation Energy Calculation and Free Energy Profiles.

Activation energies for dATP and TTP binding have been calculated using the slopes from Arrhenius analysis (Figure 2.11A) and the results are summarized in Table 2.3. Both K65R and K66R decrease the activation energy, indicating that the binding of normal nucleotides is more favorable in the two mutants. Compared with K66R, K65R shows a more obvious impact. It decreases the activation energy for TTP binding down to 47 KJ mol^{-1} (101.6 KJ mol^{-1} in the wild type RT) and the activation energy for dATP binding down to 64.9 KJ mol^{-1} (88.8 KJ mol^{-1} in the wild type RT). In addition, enthalpy change (ΔH) upon nucleotide binding was calculated by using Van't Hoff equation (Figure 2.11B). The K_d values were obtained from temperature dependence stopped flow experiments and the ratio of S/K_d (S=100 μM) was used for calculating the free energy change under the physiological conditions (ΔG' = -RTln([S]/K_d). The results indicate that the reactions of dATP and TTP binding to the RTs in this study are exothermic. Both K66R and K65R mutants decrease the magnitude of the enthalpy change for nucleotide binding, making it less negative. Again, K65R decreases it more significantly.

The free energy profiles for both nucleotides and analog incorporation were plotted (Figure 2.12) by using the equilibrium constants governing each step through the ground state binding to the product release. The information regarding the reverse of chemistry (k_{-3}) and pyrophosphate rebinding were obtained from our previous study (Chapter 3) (127). The results show that all RTs have a higher energy barrier for AZT

and TFV incorporation in steps from the conformational change (FD_nN) to the chemistry ($FD_{n+1}PPi$), indicating that all RTs either increase the rate of the reverse of the conformational change or decrease the rate of the chemistry for AZT and TFV incorporation. The effect of K65R mutant on the chemistry of TFV incorporation could be easily observed by analyzing the amplitude difference between the lowest energy state of $FD_{n+1}PPi$ and the lowest energy state of FD_nN of TFV incorporation in Figure 2.12F. However, the effect of K65R on the chemistry of AZT incorporation could not be easily observed, and the reason is that K65R decreases the k_3 value by only 8-fold in AZT versus TTP incorporation, which is much lower than that in TFV versus dATP incorporation (around 85-fold). If we compare the difference between mutants and wild type RT, we can clearly observe the influence of K65R on the chemistry step for both drugs (Figure 2.13). Actually, by looking the change of k_3 value alone (Table 2.1) for both drugs, they are actually comparable. K65R mutant decreases the k_3 in AZT incorporation by 60-fold (30 s^{-1} for TTP incorporation to 0.5 s^{-1} for AZT incorporation), and k_3 in TFV incorporation by 71-fold (5 s^{-1} for dATP incorporation to 0.07 s^{-1} for TFV incorporation).

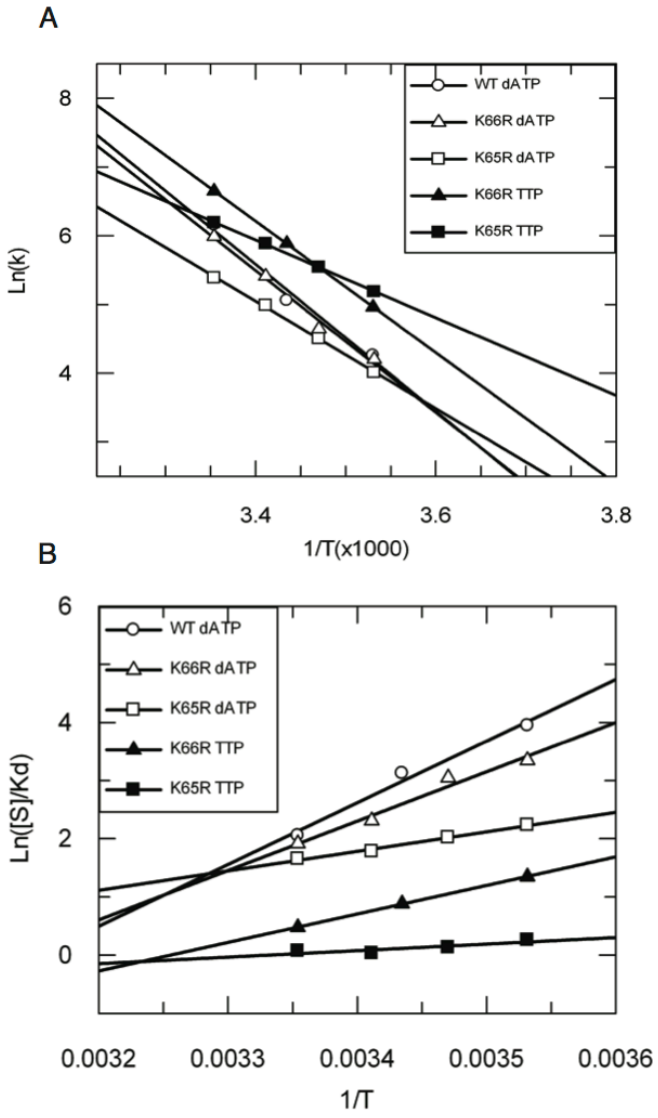

Figure 2.11 Arrhenius plot and Van't Hoff analysis on the temperature dependent stopped flow experiments.

Lines with closed symbol represent the temperature dependence for TTP binding and lines with open symbol represent the temperature dependence for dATP binding. Circle, triangle and square represent wild type RT, K66R mutant and K65R mutant, respectively.

Table 2.5 Thermodynamic Parameters Governing Nucleotide Binding and Conformational Change

dNTP	Enzyme	Δ H (kcal mol^{-1})	E_a (KJ mol^{-1})
TTP	WT[a]	-13.8 ± 6.8	101.6 ± 4.5
	K66R	-9.8 ± 0.2	79.5 ± 0.6
	K65R	-2.2 ± 0.9	47 ± 0.7
dATP	WT	-21 ± 2.6	88.8 ± 12.5
	K66R	-16.9 ± 1.9	85.8 ± 6.3
	K65R	-6.7 ± 0.5	64.9 ± 1.7

Note: [a] value obtained from *Matthew W. Kellinger and Kenneth A. Johnson (2011) (reference (126))*
1 kcal mol^{-1} = 4.184 KJ mol^{-1}

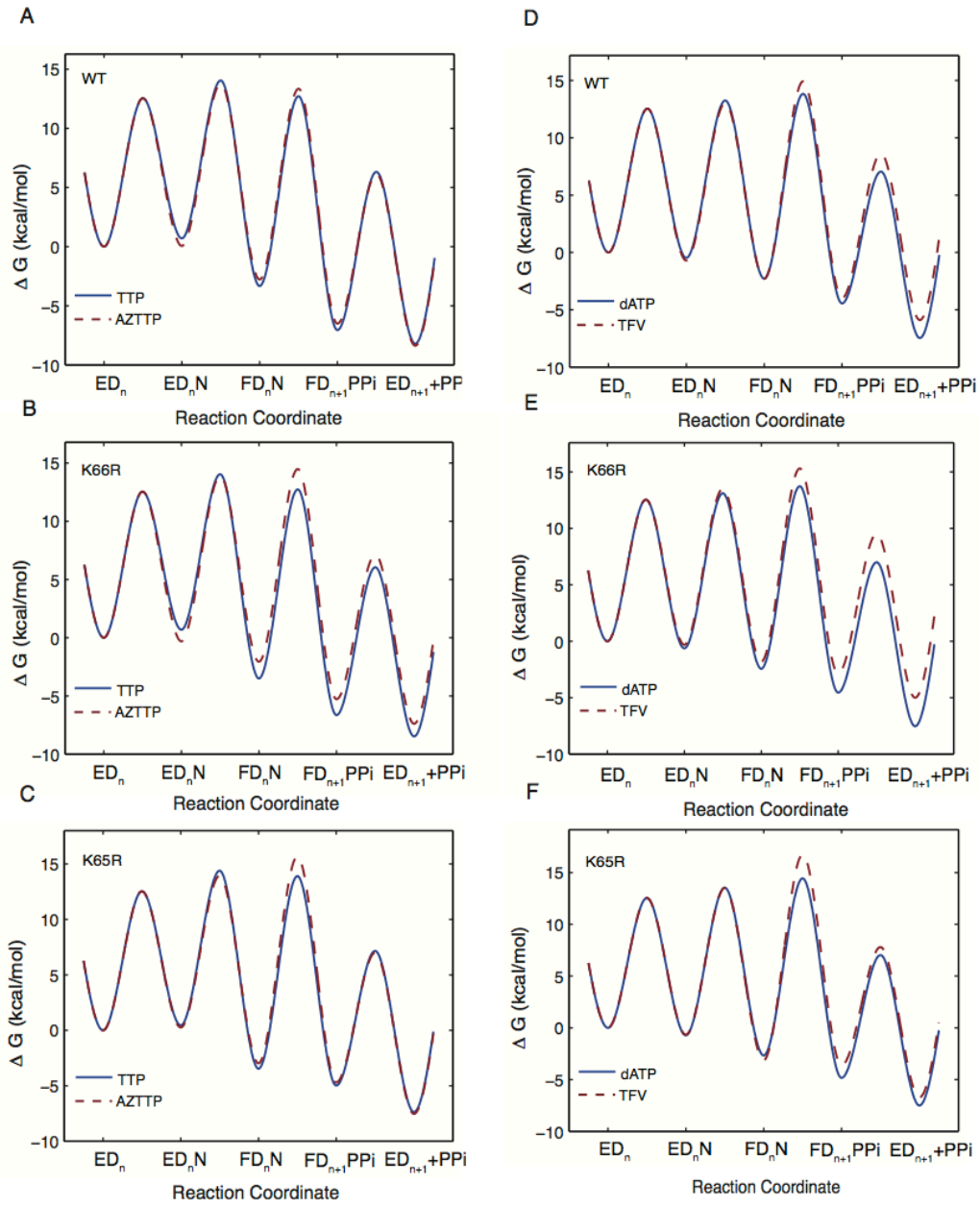

Figure 2.12 Free energy profiles for dATP, TTP, TFV and AZT incorporation.

(A-C) free energy profiles for TTP and AZT incorporation by wild type, K66R and K65R RTs. (B-F) free energy profiles for dATP and TFV incorporation by wild type, K66R and K65R RTs. The free energy was calculated using the equilibrium constants from Table 2.1. The physiological concentrations of nucleotides and pyrophosphate were set as 100 μM and 4 μM, respectively.

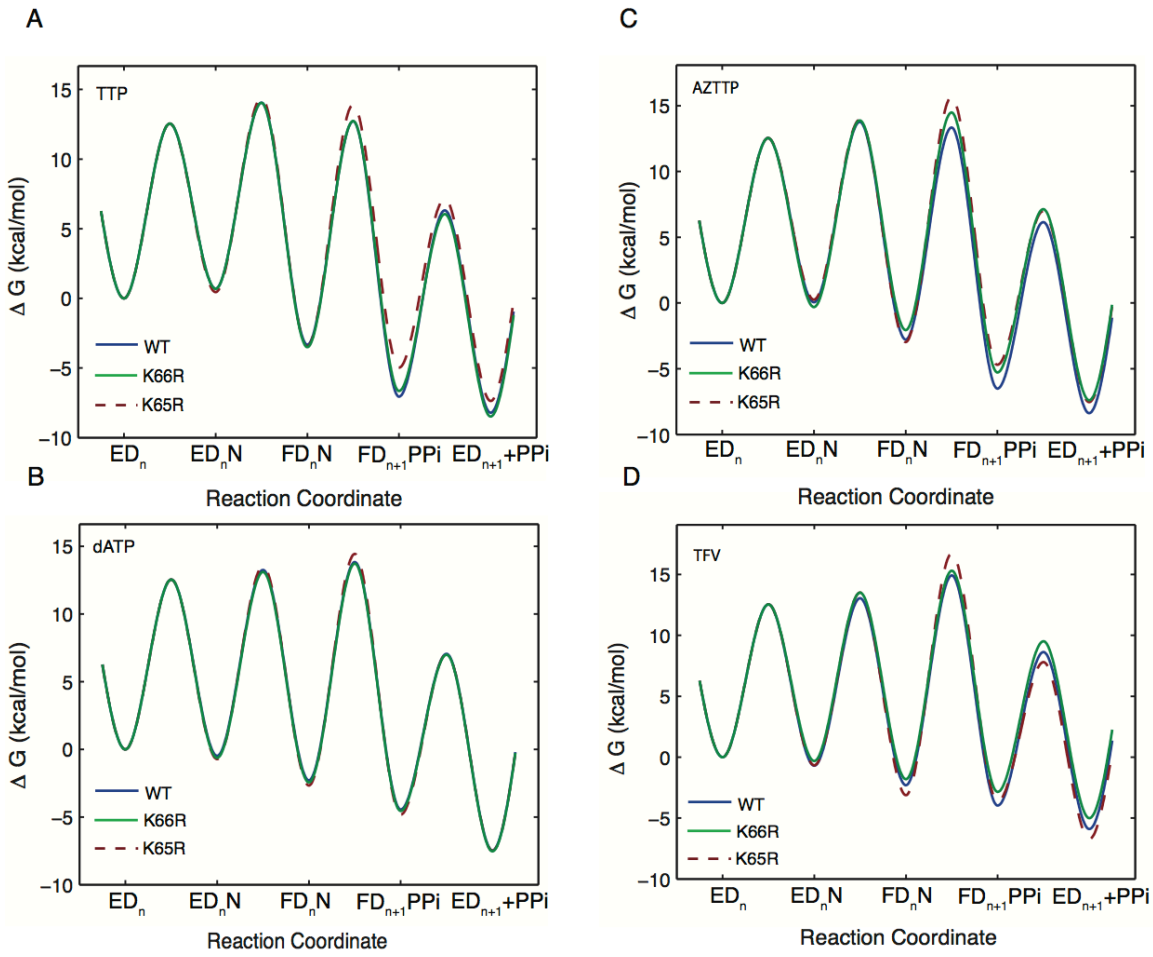

Figure 2.13 Free energy profiles for dATP, TTP, TFV and AZT incorporation.

(A) Free energy profiles for TTP incorporation by wild type, K66R and K65R RTs. (B) Free energy profiles for dATP incorporation by wild type, K66R and K65R RTs. (C) Free energy profiles for AZT incorporation by wild type, K66R and K65R RTs. (D) Free energy profiles for TFV incorporation by wild type, K66R and K65R RTs. The free energy was calculated using the equilibrium constants from Table 2.1. The physiological concentrations of nucleotides and pyrophosphate were set as 100 μM and 4 μM, respectively.

2.4 DISCUSSION

In this chapter, the kinetic effects of K65R and K66R on TFV and AZT incorporation were studied to define the mechanisms for drug resistance. Results from two experimental methods (rapid chemical quench-flow and stopped-flow) were globally fit to a complete model shown in scheme 2.1 to define the rate constants for each individual step from ground state binding to the chemistry. The advantage of rapid chemical quench-flow method is that it allows definition the apparent binding of incoming nucleotide and the rate of the chemistry in the reaction by direct measurement of reactions occurring at the active enzyme site. The advantage of stopped-flow method is that it allows us to directly define the rate of conformational change upon nucleotide binding. In addition, the recovery of the fluorescence could also be used to define the rate of the chemistry under conditions where enzyme opening and pyrophosphate release is fast after chemistry. Global fitting of two experiments therefore provides us an accurate measurement on kinetic parameters governing each kinetically significant individual step as shown in the scheme 2.1, with the exception of the reverse of chemistry (k_{-3}) and pyrophosphate release. The reverse of chemistry (k_{-3}) was defined by experiments designed to measure pyrophosphorolysis (127). Because pyrophosphate release is a very fast under the conditions studied here (128, 129), it does not affect our calculation of k_{cat}/K_m value.

The main effect of K65R was on the rate of the chemistry. It decreases the k_3 values governing dATP and TTP incorporation by 5 and 8.5-fold, respectively. This mutation causes a decrease in the k_3 values for TFV and AZT incorporation by 70 and 60-

fold, respectively. Therefore, the main effect of K65R on NRTIs resistance (TFV and AZT) is to decrease the rate of the chemistry rather than to restrain the conformational change of HIVRT. The non-clinical mutation K66R does not significantly affect natural nucleotide (dATP and TTP) incorporation. It only slightly weakens the binding of NRTIs. For TFV binding, K66R affects the ground state binding by about 2-fold. For AZT binding, it affects the conformational change of HIVRT by about 6-fold.

The kinetic partitioning governed by the relative values of the rate of the reverse of conformational change (k_{-2}) versus the rate of chemistry (k_3) is an important kinetic parameter because it provides the key to understand the role of the conformational change in enzyme specificity. HIVRT holds tightly on to the correct nucleotide, but promotes the dissociation of a mismatch (130). When the rate of chemistry (k_3) is much greater than the rate of the reverse of conformational change (k_{-2}), the specificity is determined only by the rate of binding including the isomerization step. In other words, the specificity constant (k_{cat}/K_m) can be simplified by K_1k_2, and it is not dependent on the rate of chemistry (k_3) so long as $k_3 > k_{-2}$. When the rate of chemistry is much smaller than the rate of the reverse of conformational change ($k_{-2} >> k_3$), the reduced rate of chemistry allows the substrate binding to come to equilibrium prior to chemistry, and then the specificity constants is determined by the product of equilibrium constants and the rate of chemistry ($K_1K_2k_3$). In this case, because the conformational change comes to equilibrium preceding chemistry, the K_m reflects the true $K_{d,net}$ (Table 2.4).

Our results show that the nucleotide off-rates (k_{-2}) are much smaller than the rates of chemistry (k_3) for TTP incorporation. In fitting the data globally, we derived values for

K_m, K_1, K_2, k_2, k_{-2}, and k_3, that are all consistent with the data. When $k_{-2} << k_3$, then $K_m = k_3/K_1k_2$. Accordingly, the validity of this approximation ($k_{-2} << k_3$) can be evaluated from the ratios of K_m divided by k_3/K_1k_2. For wild type, K66R, and K65R RT the ratios are 1.2, 1.2 and 1.5 respectively (Table 2.4), indicating that the approximation is valid especially in K66R and wild type RT. These results lead to the conclusion that the conformational change for TTP incorporation fails to come to equilibrium prior to chemistry, and the specificity constant (k_{cat}/K_m) is largely determined by the apparent second order rate constant for substrate binding defined by K_1k_2.

The effects of the mutations on the kinetics governing AZT incorporation are different than those for TTP incorporation. The K65R mutant increases the ratio (K_m divided by k_3/K_1k_2) to 18.5, because this mutant increases the rate of the reverse of conformational change and decreases the rate of chemistry, which makes the conformational change coming to equilibrium prior to chemistry. Therefore, the specificity constant (k_{cat}/K_m) governing AZT incorporation is determined by the product $K_1K_2k_3$. The K66R mutation also shows a similar but much weaker effect than K65R. A ratio of only 3.6 indicates that K66R does increase the nucleotide off rate or decrease the rate of chemistry for AZT incorporation, but this effect may not be high enough to allow the conformational change to completely come to equilibrium preceding the chemistry. In this case, it is a complicated situation where simplification of specificity constant to K_1k_2 or $K_1K_2k_3$ cannot be used; rather, the intermediate result requires computation of k_{cat}/K_m from the full equation. A similar trend has also been observed in dATP incorporation by all three RTs (the ratios are 3.7, 3.9, 5.3 for wild type, K66R and K65R respectively).

Compared with dATP, TFV have a much higher relative value of K_m versus k_3/K_1k_2 in all three RTs with K65R showing the most obvious trend (the ratio is increased up to 176 by K65R), suggesting that the conformational change of all three RTs (especially K65R) come to equilibrium prior to the chemistry upon TFV incorporation. The K_m values of TFV incorporation by all three RTs are comparable (or equal) to the true $K_{d,net}$, as shown in Table 2.4. A relatively high ratio of K_m versus k_3/K_1k_2 occurred with dATP incorporation not with TTP incorporation and may result from the structural difference between purines and pyrimidines. One of our recent studies on dCTP incorporation also shows that the chemistry is much faster than the nucleotide off rate (ratio of K_m versus k_3/K_1k_2 is close to 1), as shown in TTP incorporation (123).

Table 2.6 Kinetic Constants for Defining the Reverse Rate of Conformational Change

Enzyme	dNTP	K_m/ (k_3/K_1k_2)	K_m (μM)	$K_{d,net}$ (μM)	$k_{-2}(s^{-1})^b$	Lower Limit	Upper Limit
WT[a]	TTP	1.2	4.7 ± 0.2	<0.5	<4	3.8	4.2
	AZT	1.6	3.5 ± 0.3	<1.1	<15.3	13.6	18.4
K66R	TTP	1.2	3.4 ± 0.1	<0.4	<4.9	2.9	6.1
	AZT	3.6	4.7 ± 0.1	3.4 ± 0.2	40 ± 1	40	41
K65R	TTP	1.5	1.2 ± 0.1	<0.4	<2.6	1.3	4.1
	AZT	18.5	0.9 ± 0.1	0.8 ± 0.1	8.3 ± 0.2	7.2	11.2
WT	dATP	3.7	3.5 ± 0.7	2 ± 0.3	77 ± 1.1	77	86
	TFV	21.2	2.4 ± 0.1	2.3 ± 0.1	105 ± 1.9	99.6	127
K66R	dATP	3.9	2.7 ± 0.4	1.8 ± 0.3	75 ± 1	75	85
	TFV	18	5.2 ± 0.2	5 ± 0.2	111 ± 2.3	98.5	134
K65R	dATP	5.3	1.6 ± 0.1	1.3 ± 0.1	26 ± 0.5	23.1	30.7
	TFV	176	0.6 ± 0.1	0.6 ± 0.1	13 ± 0.6	9.9	13

Note: The net K_d as a result of two-step nucleotide binding was calculated as $1/(K_1(1+K_2))$. The $k_{-2}{}^b$ in this table is used to represent the range of accurate k_{-2} obtained from two experiments. The *chi* threshold at boundary was set as 1.02 to define the lower and upper limit of k_{-2}.

Another way of comparing k_{-2} and k_3 values is to perform computer simulation by using *KintTek Explorer* software (KinTek-Corp. Austin, TX). We performed the global fitting for the stopped flow experiments and rapid chemical quench flow experiments by using a complete model including each step in the nucleotide or drug incorporation.

Because stopped flow measurements and the temperature dependence experiments define the values of K_1 and k_2, and rapid chemical quench flow experiments define the maximum rate of polymerization k_{pol} and apparent K_d, which approximates k_3 and K_m, respectively. The computer simulation can directly give us the k_{-2} and k_3 values and then the FitSpace confidence contours from *KintTek Explorer* software (KinTek-Corp. Austin, TX) allow us to evaluate the standard errors on fitted parameters and estimate the lower bound and upper bound for the k_{-2} value (As shown in Table 2.4). If $k_{-2}>>k_3$, the k_{-2} values can be accurately obtained by the global fitting. If $k_{-2}<<k_3$, as shown in our data for TTP incorporation, the global fitting of two experiments only gives a range for k_{-2} value (Table 2.4). In this case, nucleotides off rate experiments were performed to directly observe the k_{-2} value (Figure 2.7). Global fitting all three experiments then gave us a well-constrained value for each kinetic parameter in the incorporation (eg. TTP incorporation). Finally, the data from global fitting and the results from the calculation of the relative values of K_m versus k_3/K_1k_2 are all summarized in Table 2.4, and the results from both methods are actual consistent to each other. The advantage of global fitting is that it not only tells whether k_{-2} is much greater or smaller than k_3 but also gives the accurate number for each kinetic parameter.

It has been reported that K65R mutant decreases the susceptibility to TFV incorporation and other NRTIs, but remains or increases the susceptibility to AZT incorporation (96, 98-100). The results from our studies suggest that K65R mutant does show a higher discrimination against TFV compared with AZT incorporation, but the drug resistances for the two drugs are actually comparable. This result is supported by

reports showing that AZT and TFV are associated with similar reductions in HIV-1 RNA levels in the presence of K65R mutant (101). It is also supported by some clinical reports showing that a complete virologic response was seen in 58% of patients receiving AZT for treatment and in 64 % of the patients receiving TFV in the week 12 after salvage therapy, and AZT and TFV were associated with similar reductions in the viral load (0.6 to 0.9 log copies/mL for AZT and TFV, respectively) (131).

It has been reported that the resistance to TFV is mainly attributed to the ability of K65R to slow the maximum rate of polymerization k_{pol} for both dNTP and TFV (99, 132). However, problems arise when attempting accurately interpret the data from the steady state measurement because they lack the important information regarding each individual kinetic parameter for the reaction. Especially, we do not know the role of the conformational change and the reverse of the conformational change in the TFV drug discrimination and resistance. Our data suggests that the rate of the reverse of the conformational change is much greater than the rate of chemistry in TFV incorporation by all RTs. K65R further increases this trend, allowing the conformational change to come to equilibrium prior to chemistry. Therefore, the specificity constant for TFV incorporation is governed by the product of the equilibrium and the rate of chemistry and k_{cat}/K_m can be simplified by $K_1K_2k_3$. Recently, molecular modeling has suggested that K65R mutation may reduce the conformational mobility of HIVRT by forming a rigid molecular platform with residue R72, from which may discriminate against the incorporation of TFV (96). However, no biochemical experiment has been performed to investigate the role of conformational change in the TFV drug resistance. The results

from our study suggest that K65R does decrease the rate of the forward conformational change for both dATP and TFV incorporation, but it decreases the rates of the reverse of the conformational change as well. Therefore, the equilibrium constant (K_2) for dATP incorporation was not changed too much compared with wild type RT, and the K_2 value for TFV incorporation was actually increased by 4-fold. This favorable effect for conformational change does not agree with the statement that K65R mutation highly restricts the conformational change by forming a rigid molecular platform with R72 residue in the active site. In addition, compared with the change of k_3 (~71-fold) caused by this mutant, the change of K_2 actually is very small which indicates that the main effect of K65R is to decrease the chemistry and make the conformational change coming to equilibrium for TFV incorporation.

The mechanism of drug resistance to AZT incorporation by K65R is actually similar to that of TFV incorporation. AZT incorporation in wild type RT is a complicated situation where the rate of the reverse of conformational change (k_{-2}) is lower than the chemistry (k_3) but the difference is not great enough to allow us to make a conclusion of $k_3 >> k_{-2}$. Therefore, the specificity constant (k_{cat}/K_m) governing AZT incorporation by wild type RT cannot be simplified by K_1k_2 or $K_1K_2k_3$. It is true that the mutation of K65R further decreases the rate of the reverse of conformational change (k_{-2}) by about 2-fold, but it decreases the chemistry (k_3) much greater (by 60-fold). Due to the huge decrease in the rate of the chemistry, $k_{-2} >> k_3$ and the conformational change comes to equilibrium preceding chemistry. Therefore, the specificity constant for AZT incorporation by K65R is governed by the product of the equilibrium constant and the rate of the chemistry.

Lysine 65 and 66 residues are adjacent to each other in the fingers domain of HIVRT. Studies on the drug resistance of K65R mutant have been widely investigated, but studies on the effect of K66R mutant has been very rarely reported. Because K66 lies adjacent to the phosphate of the penultimate nucleotide (97), suggesting the possible significance for this residue in the nucleotide or NRTIs incorporation. In our study, we have investigated the effect of K66R on both AZT and TFV incorporation, and possible mechanisms for the resistance. The results suggest that K66R causes a mild drug resistance against AZT and TFV with an effect weaker than K65R. The resistance against TFV and AZT by K66R mutation mainly results from its influence in weakening the binding of NRTIs. For TFV incorporation, K66R mainly influences the ground state binding step. For AZT incorporation, it influences each steps through ground state binding to the chemistry but the main effect of this mutant is to influence the ground state binding and conformational change. Compared with TTP incorporation, K66R mutant increases the ground state binding for AZT incorporation by about 5-fold, and it decreases the equilibrium constant (K_2) of conformational change by about 50-fold. Therefore, the net K_d ($K_{d,net}$) for AZT incorporation is around 9-fold higher than for TTP incorporation.

In conclusion, our studies provide much more great detail in the understanding of the mechanisms of TFV and AZT resistance by K65R mutation. The results indicate that K65R causes a comparable resistance against TFV and AZT, and the mechanisms for the resistance are actually similar. Because K65R mutation shows bidirectional phenotypic antagonism with TAMs (122, 133) and AZT selects for the TAMs (65, 125),

it is very rare to find K65R mutation associated with AZT resistance. But it does not preclude a role of K65R in resistance against AZT. A better understanding regarding the drug resistance against TFV and AZT by K65R might be achieved by performing ATP and pyrophosphate-mediated AZT/TFV excision experiments. In addition, our studies also provide a better understanding about the role of K66R in AZT and TFV drug discrimination and resistance. Because K66R is a nonclinical mutation, our system and simulation not only allows to define the specific mechanism for clinical occurred drug resistance, but also allows to predict the possible resistance for any not-happened-yet mutations. Therefore, any future possible drug resistance could be predicted by our system, from which better drugs could be designed in future.

Chapter 3: The Roles of HIV Reverse Transcriptase K65R and K66R in NRTIs Resistance by Excision Mechanism

3.1 INTRODUCTION

HIV infection is a process that requires the action of several enzymes. HIV-1 reverse transcriptase (HIVRT), due to its critical role in the viral replication, serves as a target for many HIV drugs. Non-nucleoside reverse transcriptase inhibitors (NNRTIs) and nucleoside reverse transcriptase inhibitors (NRTIs) are two groups of HIV drugs that target at HIVRT. NNRTI binds to the site adjacent to the polymerase active site and the binding of NNRTI decreases the rate of the chemistry for nucleotide incorporation (39, 40). NRTIs bind to the active site of HIVRT, but because they lack the 3'-OH they prevent the incorporation of the following nucleotide and serve as chain terminators (120, 134). HIVRT evolves to escape the efficacy of NRTIs by mutagenesis at multiple residues around the active site (100, 102, 135). For example, tenofovir (TFV) resistance has been reported in the presence of K65R or M184V mutation, and azidothymidine (AZT) resistance has been reported in the presence of a combination of six mutations called thymidine analogue mutations (TAMs mutation) (120). There are two possible mechanisms regarding to the NRTI resistance: discrimination and excision. Discrimination is the mechanism that the mutations of HIVRT discriminate against NRTI by reducing its incorporation efficiency (96). Excision is the mechanism that after NRTI has been incorporated, it can be excised from the end of the DNA primer through ATP or

pyrophosphate-mediated excision. Therefore, the ability of primer extension of HIVRT could also be restored (120, 136).

Lysine 65 interacts with to the γ phosphate of the incoming nucleotide and it is claimed that K65R is a signature mutation leading to TFV resistance (58, 98). It is very rarely reported that the mutation of K65R is associated with AZT resistance (96, 133), and the AZT resistant mutants rarely co-exist with the K65R mutation. Therefore, many believe that K65R may cause hyper-susceptibility to AZT by greatly decreasing the ATP-mediated excision (98, 100, 122, 133, 137, 138). Recently, it was proposed that the rigid molecular platform formed by K65R and R72 restrains the conformational adaptability of the fingers domain to interfere with ATP binding and decrease the efficiency of ATP-mediated excision (96). However, this hypothesis was made solely based on the structural analysis of HIVRT (96) and no biochemical experiments have been reported to test this hypothesis. Although structural analysis is helpful for better understanding of the mechanism in the catalysis, it only provides a static picture of the active site and hence misses the important dynamic movement. Most of all, structural analysis has to be combined with biochemical experiments to investigate the kinetics of nucleotide incorporation in order to quantify the specificity constant governing catalysis. Actually, it is reported that AZT and TFV caused similar reductions in the RNA levels in the presence of K65R mutation (101) and had similar reductions in the viral load of K65R patients (131). In our previous study, it was shown that the mutation of K65R causes significant discrimination against TFV and AZT. Therefore, this raises a question

regarding to the effect of K65R mutation on ATP or pyrophosphate-mediated excision. In this chapter, the effects of this mutation on the excision of NRTIs were investigated.

It has been reported that mutations in K66 influence both the mismatch extension and misinsertion rates of HIV-1 reverse transcriptase (97). Therefore, the significance of K66R mutation on NRTIs drug resistance should not be overlooked. Recently, it was shown that the mutation of K66R causes a mild drug resistance against TFV and AZT incorporation (Chapter 2). Because this residue is adjacent to the penultimate nucleotide of the primer, and excision reaction occurs by attacking the phosphodiester bond between the penultimate nucleotide and the NRTI at the 3' end of the primer using ATP or pyrophosphate (102), it is necessary to investigate the effects of K66R on ATP-mediated excision and pyrophosphate-mediated excision.

Although NRTI excision is an important mechanism of drug resistance, the primary substrate for NRTI excision is still unknown. Many believe that ATP is the primary substrate for excision *in vivo* (102, 120, 134, 135), because the rates for ATP-mediated AZT excision are quite different in wild type RT and TAMs mutations, and the rates for pyrophosphate-mediated AZT excision are comparable in two RTs (120, 135). However, the efficiencies of two substrates (ATP and pyrophosphate) in the excision of AZT have never been directly compared. In this chapter, we investigated the effects of two substrates not only for AZT excision, but also for TFV excision. In addition, we directly compared the efficiencies of two excision reactions with the efficiency of the nucleotide incorporation. Because it is known that the physiological concentrations of ATP, pyrophosphate and dNTP are known as 3.2 mM, 150 μM and 30 μM, respectively

(136, 139), the effects of all three reactions were calculated by using the physiological concentrations of substrates times the specificity constants (k_{cat}/K_m) of the reaction. This is the first time that the contributions from all three reactions could be directly compared. Therefore, our study provides a better understanding of the effects of K65R and K66R on the NRTIs excision, the roles of each primary substrate in the NRTIs excision, and the contribution of each reaction *in vivo* including nucleotide incorporation, ATP-mediated excision and pyrophosphate-mediated excision.

3.2 MATERIALS AND METHODS

Purification of K65R and K66R Mutants

Mutations of K65R and K66R were introduced to HIV wild type reverse transcriptase using Quickchange Site Directed Mutagenesis kit. Protein was expressed and purified as previous described (123). Briefly, two subunits (p51 and p66) of the mutants were separately expressed, sonicated and co-purified. Proteins were purified by using the tandem Q-Sepharose and Bio-Rex70 columns, and followed by single-stranded DNA (ssDNA) affinity column. The active site concentrations of purified protein were determined by active site titration experiments by measuring the burst of product formation as a function of DNA concentration using KinTek RQF-3 instrument (KinTek-Corp. Austin, TX).

DNA Substrates for Kinetic Studies

To prepare the DNA substrates for kinetic studies, the 25-nt and 45-nt oligonucleotides (Table 3.1) were purchased from Integrated DNA Technologies. The 25/45-nt DNA substrates were annealed by heating at 95° for 5 minutes and slowly cooling down to the room temperature. The 25-nt DNA substrate was labeled at the 5' end by γ-^{32}P for use in the quench flow kinetic assays. The 26/45-nt DNA substrates were prepared by allowing the incorporation of the next incoming nucleotide (dTTP), followed by purifying the 26-nt oligonucleotide and annealing the 26/45-nt-20AGC DNA substrates using the method described above. The 26-nt terminated with AZT or TFV primer were prepared by allowing the incorporation of the next incoming nucleotide analogs (AZT or TFV) into 25/45-nt-20AGC or 25/45-nt-20TGC DNA substrates, followed by purifying the 26-nt AZT or 26-nt TFV oligonucleotides and annealing the 26Z/45-nt (26-nt AZT/45-nt-20AGC) or 26V/45-nt (26-nt TFV/45-nt-20TGC) using the method described above.

Table 3.1 DNA Substrates for Kinetic Studies in Excision Experiments

25/45-nt-20AGC	
25-nt:	5′-GCCTCGCAGCCGTCCAACCAACTCA-3′
45-nt:	5′-CGGAGCGTCGGCAGGTTGGTTGAGT**A**GCAGCTAGGTTACGGCAGG-3′
26/45-nt-20AGC	
26-nt:	5′-GCCTCGCAGCCGTCCAACCAACTCAT-3′
45-nt:	5′-CGGAGCGTCGGCAGGTTGGTTGAGT**A**GCAGCTAGGTTACGGCAGG-3′
26AZT/45-nt-20AGC	
26-nt:	5′-GCCTCGCAGCCGTCCAACCAACTCAZ-3′
45-nt:	5′-CGGAGCGTCGGCAGGTTGGTTGAGT**A**GCAGCTAGGTTACGGCAGG-3′
26TFV/45-nt-20TGC	
26-nt:	5′-GCCTCGCAGCCGTCCAACCAACTCAV-3′
45-nt:	5′-CGGAGCGTCGGCAGGTTGGTTGAGT**T**GCAGCTAGGTTACGGCAGG-3′

Pyrophosphorolysis Experiments

Pyrophosphorolysis experiments were performed by mixing a preformed enzyme-DNA complex (75 nM enzyme and 50 nM ^{32}P labeled DNA substrates) with various concentrations of pyrophosphate at 37 °. The reaction was quenched by addition of 0.5 M EDTA at varying time points. Products were collected and separated on 15% denaturing PAGE (acrylamide (1:19 bisacrylamide), 7M Urea). Results were then analyzed by ImageQuant 6.0 software (Molecular® Dynamics).

ATP-mediated AZT or TFV Excision (Direct Excision)

ATP-mediated AZT or TFV excision experiments were performed by mixing preformed enzyme-DNA complex (150 nM enzyme and 100 nM ^{32}P labeled 26Z/45-nt or 26V/45-nt DNA substrates) with various concentrations of ATP at 37 °. The reaction was quenched by addition of 0.5 M EDTA at varying time points. Products were collected and separated on 15% denaturing PAGE (acrylamide (1:19 bisacrylamide), 7M Urea). Results were then analyzed by ImageQuant 6.0 software (Molecular® Dynamics).

ATP-mediated AZT or TFV Excision and Extension

ATP-mediated AZT or TFV *Excision and Extension* experiments were performed by mixing preformed enzyme-25/45-nt DNA (20AGC or 20TGC) complex (150 nM enzyme and 100 nM ^{32}P labeled DNA substrates) with 25 μM AZT or TFV at 37 ° for 5 min, followed by adding various concentrations of ATP, 100 μM of the next incoming nucleotides and 1 μM dCTP into the reaction. The reaction was quenched by addition of 0.5 M EDTA at varying time points. Products were collected and separated on 15% denaturing PAGE (acrylamide (1:19 bisacrylamide), 7M Urea). Results were then analyzed by ImageQuant 6.0 software (Molecular® Dynamics).

Global Analysis of Kinetic Data

The kinetic constants defining pyrophosphorolysis reactions were derived by fitting data to the model shown in scheme 3.1 and 3.2 by *KinTek Explorer* software (KinTek-Corp.). The kinetic constants defining ATP-mediated AZT or TFV excision were globally fit to the model shown in scheme 3.3 or 3.4 by *KinTek Explorer* software

(KinTek-Corp.). FitSpace confidence contours were performed for each analysis to assess errors on fitted parameters.

Scheme 3.1 Pyrophosphorolysis of natural nucleotide

$$ED_n pdA + PP_i \underset{}{\overset{K_{pp}}{\rightleftharpoons}} ED_n pdA \cdot PP_i \underset{k_{-a}}{\overset{k_a}{\rightleftharpoons}} ED_n + dATP$$

Scheme 3.2 Pyrophosphorolysis of NRTIs and followed natural nucleotide

$$ED_n pX + PP_i \underset{}{\overset{K_{pp1}}{\rightleftharpoons}} ED_n pX \cdot PP_i \underset{k_{-a1}}{\overset{k_{a1}}{\rightleftharpoons}} ED_n + XTP$$

$$ED_n pdA + PP_i \underset{}{\overset{K_{pp2}}{\rightleftharpoons}} ED_n pdA \cdot PP_i \underset{k_{-a2}}{\overset{k_{a2}}{\rightleftharpoons}} ED_n + dATP$$

Scheme 3.3 ATP-mediated excision

$$ED_n pX + ATP \underset{}{\overset{K_{ATP}}{\rightleftharpoons}} ED_n pX \cdot ATP \underset{k_{-b}}{\overset{k_b}{\rightleftharpoons}} ED_n + Xp4A$$

Scheme 3.4 Complete model for AZT mediated excision

$$ED_n pX + ATP \underset{}{\overset{K_{ATP}}{\rightleftharpoons}} ED_n pX \cdot ATP \underset{k_{-b}}{\overset{k_b}{\rightleftharpoons}} ED_n + Xp4A \quad (Excision)$$

$$\Updownarrow^{dCTP} \qquad\qquad \Updownarrow^{TTP\ or\ dATP}$$

$$ED_n pX \cdot dCTP \qquad\qquad ED_{n+1}$$

(Dead End Complex)

$$\Updownarrow^{dCTP}$$

$$ED_{n+2} \quad (Extension)$$

3.3 RESULTS

Pyrophosphorolysis of dATP- and TFV- terminated primers

Pyrophosphorolysis of dATP-terminated primer experiments were performed by mixing various concentrations of pyrophosphates with preformed enzyme-DNA complex (25/45-nt DNA substrate) using rapid chemical quench flow instrument (KinTek Corp. Austin, TX). The product formation (the formation of 24-nt) versus time was plotted for each concentration of pyrophosphate (Figure 3.1). Then, the global fitting were performed using the model in scheme 3.1 by *KinTek Explorer* software (KinTek Corp) where K_{pp} represents the dissociate constant ($K_{d,app}$) for pyrophosphate, k_a represents the maximum rate of pyrophosphorolysis of dATP-terminated primer (k_{pyro}) and k_{-a} represents the second order rate constant for the reverse of pyrophosphorolysis. The values of k_a (k_{pyro}), K_{pp} ($K_{d,app}$), and the specificity constant ($k_{pyro}/K_{d,app}$) for pyrophosphorolysis of dATP-terminated primer are all well defined in the global fitting. The results showed that K65R mutant decreases the maximum rate of pyrophosphorolysis of dATP-terminated primer (k_{pyro}) by 5-fold and the apparent pyrophosphate dissociate constant ($K_{d,app}$) by 1.8-fold (Table 3.1), as compared with wild type RT. As a result, K65R has 2.5-fold decrease on the specificity constant ($k_{pyro}/K_{d,app}$) for pyrophosphorolysis of dATP-terminated primer. K66R mutant has no obvious effect on both k_{pyro} and $K_{d,app}$, and hence it does not significantly affect pyrophosphorolysis of dATP-terminated primer.

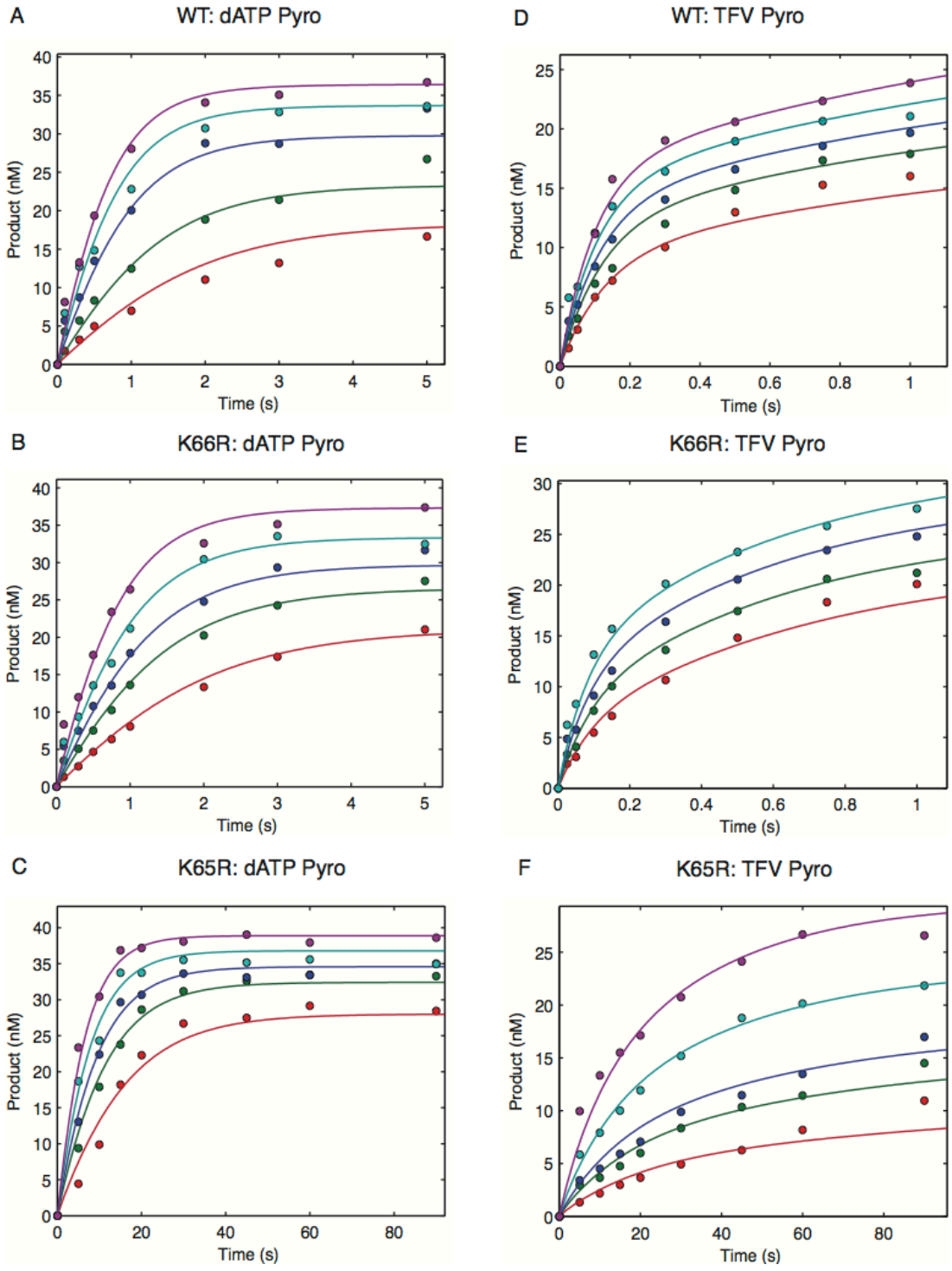
A
WT: dATP Pyro
B
K66R: dATP Pyro
C
K65R: dATP Pyro
D
WT: TFV Pyro
E
K66R: TFV Pyro
F
K65R: TFV Pyro
Product (nM)
Time (s)

(Figure 3.1)

Figure 3.1. The concentration dependence of pyrophosphorolysis of dATP- and TFV-pyrophosphorolysis.

Pyrophosphorolysis experiments were performed by mixing preformed enzyme-DNA complex (75 nM enzyme and 50 nM DNA) with various concentrations of pyrophosphates (100, 200, 300, 500, 1000 μM) at 37 °C. The reaction was quenched by addition of 0.5 M EDTA at various time points. The reactions for pyrophosphorolysis of dATP-terminated primer by wild type, K66R and K65R RT are shown in Figures 2A, 2B, and 2C, respectively. The reactions for pyrophosphorolysis of TFV-terminated primers by wild type, K66R and K65R RT are shown in Figures 2D, 2E, and 2F, respectively.

Pyrophosphorolysis of TFV-terminated primers were measured (Figure 3.1) using the same method described above. Because sequential pyrophosphorolysis of TFV- and dATP- terminated primers were observed, the time course of pyrophosphorolysis of TFV-terminated primers was fit to a sequential model shown in the scheme 3.2, where X and dA represent TFV and dATP, respectively. K_{pp1}, k_{a1}, *and* k_{-a1} represent the apparent dissociate constant ($K_{d,app}$) for pyrophosphate (PP_i) binding to TFV-terminated primer, the maximum rate of pyrophosphorolysis (k_{pyro} for TFV), and the second order rate constant for the reverse reaction (rebinding and reaction of TFV-diphosphate), respectively. K_{pp2}, k_{a2} and k_{-a2} represent the apparent dissociate constant ($K_{d,app}$) for pyrophosphate binding to dATP-terminated primer, the maximum rate of pyrophosphorolysis of dATP-terminated primer (k_{pyro} for dATP), and the second order rate constant for the reverse of pyrophosphorolysis of dATP-terminated primer, respectively. The values of K_{pp2}, k_{a2} and k_{-a2} were obtained directly from pyrophosphorolysis of dATP-terminated primer and then input into the global fitting of pyrophosphorolysis of TFV terminated primer. Kinetic parameters regarding pyrophosphorolysis of TFV terminated primer (K_{pp1}, k_{a1} and k_{a1}/K_{pp1}) are well defined in the global fitting. The result showed that K65R decreases the maximum rate of pyrophosphorolysis of TFV terminated primer (k_{pyro}) by 11-fold while increasing the dissociate constant ($K_{d,app}$) by about 6.7-fold (0.15-fold decrease). Therefore, the results in our study showed that K65R decreases the specificity constant ($k_{pyro}/K_{d,app}$) for pyrophosphorolysis of TFV terminated primer by about 72-fold. Different from K65R,

K66R actually increases the specificity constant ($k_{pyro}/K_{d,app}$) of pyrophosphorolysis of TFV terminated primer. However, the effect of K66R mutant on pyrophosphorolysis of TFV terminated primer is mild (Table 3.1).

Table 3.2 Kinetic Constants for Pyrophosphorolysis

dNTP	Enzyme	k_{pyro} (s^{-1})	F[d]	$K_{d,app}$ (μM)	F[d]	$k_{pyro}/K_{d,app}$ ($\mu M^{-1}s^{-1}$ x 10^{-3})	F[d]
TTP	WT	0.08 ± 0.01		26 ± 5		3.1 ± 0.7	
	K66R	0.15 ± 0.01	0.5 ± 0.08	78 ± 9	0.3 ± 0.07	1.9 ± 0.25	1.6 ± 0.4
	K65R	0.34 ± 0.05	0.2 ± 0.04	195 ± 22	0.1 ± 0.02	1.7 ± 0.3	1.8 ± 0.5
AZTTP	WT	0.07 ± 0.01		83 ± 16		0.8 ± 0.2	
	K66R	0.08 ± 0.01	0.9 ± 0.17	123 ± 23	0.7 ± 0.19	0.7 ± 0.16	1.1 ± 0.4
	K65R	0.03 ± 0.004	2.3 ± 0.45	400 ± 27	0.2 ± 0.04	0.07 ± 0.01	11± 3
dATP	WT	0.9 ± 0.18		545 ± 75		1.7 ± 0.4	
	K66R	0.9 ± 0.15	1 ± 0.26	506 ± 54	1.1 ± 0.2	1.8 ± 0.36	0.9 ± 0.3
	K65R	0.18 ± 0.03	5 ± 1.3	305 ± 47	1.8 ± 0.4	0.6 ± 0.14	2.5 ± 0.8
TFV	WT	0.33 ± 0.004		91 ± 8		3.6 ± 0.3	
	K66R	1.1 ± 0.1	0.3 ± 0.03	133 ± 18	0.7 ± 0.11	8.3 ± 1.4	0.4 ± 0.07
	K65R	0.03 ± 0.002	11 ± 0.74	597 ± 30	0.15 ±0.02	0.05 ± 0.004	72 ± 8

[d] Fold changes compared with the wild-type enzyme (F[d]: fold decreased)

Pyrophosphorolysis of TTP- and AZT- terminated primers

Pyrophosphorolysis of TTP- and AZT- terminated primers (Figure 3.2) were investigated similarly as described above. DNA substrates 26/45-nt and 26Z/45-nt were used for TTP and AZT, respectively. Both 24-nt DNA and 25-nt DNA were observed on

the gel indicating the reaction here is also a sequential two-step reaction. The data of pyrophosphorolysis of TTP or AZT-terminated primer were fit to a sequential model shown in the scheme 3.2, where X represents TTP or AZT, K_{pp1} represents the apparent dissociate constant ($K_{d,app}$) for pyrophosphate binding to TTP- or AZT-terminated primer, k_{a1} represents the maximum rate of pyrophosphorolysis (k_{pyro} for TTP or AZT) and k_{-a1} represents the second order rate constant for the reverse of pyrophosphorolysis of TTP- or AZT- terminated primer. The values of K_{pp2}, k_{a2} and k_{-a2} were obtained directly from pyrophosphorolysis of dATP-terminated primer and then input into the global fitting. Kinetic parameters regarding pyrophosphorolysis of TTP- or AZT-terminated primers (K_{pp1}, k_{a1} and k_{a1}/ K_{pp1}) are well defined in the global fitting. The results suggested that K65R increases the k_{pyro} of Pyrophosphorolysis of TTP-terminated primer by 5-fold and the $K_{d,app}$ by about 10-fold. Therefore, this mutant decreases the specificity constant ($k_{pyro}/K_{d,app}$) of pyrophosphorolysis of TTP-terminated primer by about 1.8-fold, as compared with wild type RT. The mutation of K66R also has a similar effect on pyrophosphorolysis of TTP-terminated primer. For pyrophosphorolysis of AZT-terminated primer, K65R decreases the specificity constant ($k_{pyro}/K_{d,app}$) by about 11-fold through decreasing the rate of k_{pyro} by 2.3-fold and increasing the rate of $K_{d,app}$ by about 5-fold. K66R does not have obvious effect on both k_{pyro} and $K_{d,app}$, and hence it does not influence the efficiency for pyrophosphorolysis of AZT-terminated primer.

In conclusion, K65R does not significantly affect the efficiency of pyrophosphate-mediated excision in the natural DNA substrate, but it does affect the efficiency of pyrophosphate-mediated excision if DNA substrate is terminated with

NRTIs. The results in our study showed that K65R decreases the efficiency of pyrophosphate-mediated TFV excision by 72-fold, and decreases the efficiency of pyrophosphate-mediated AZT excision by 11-fold. On the other hand, K66R seems does not affect the efficiency of pyrophosphate-mediated excision no matter with natural DNA substrate or with NRTIs terminated DNA substrate.

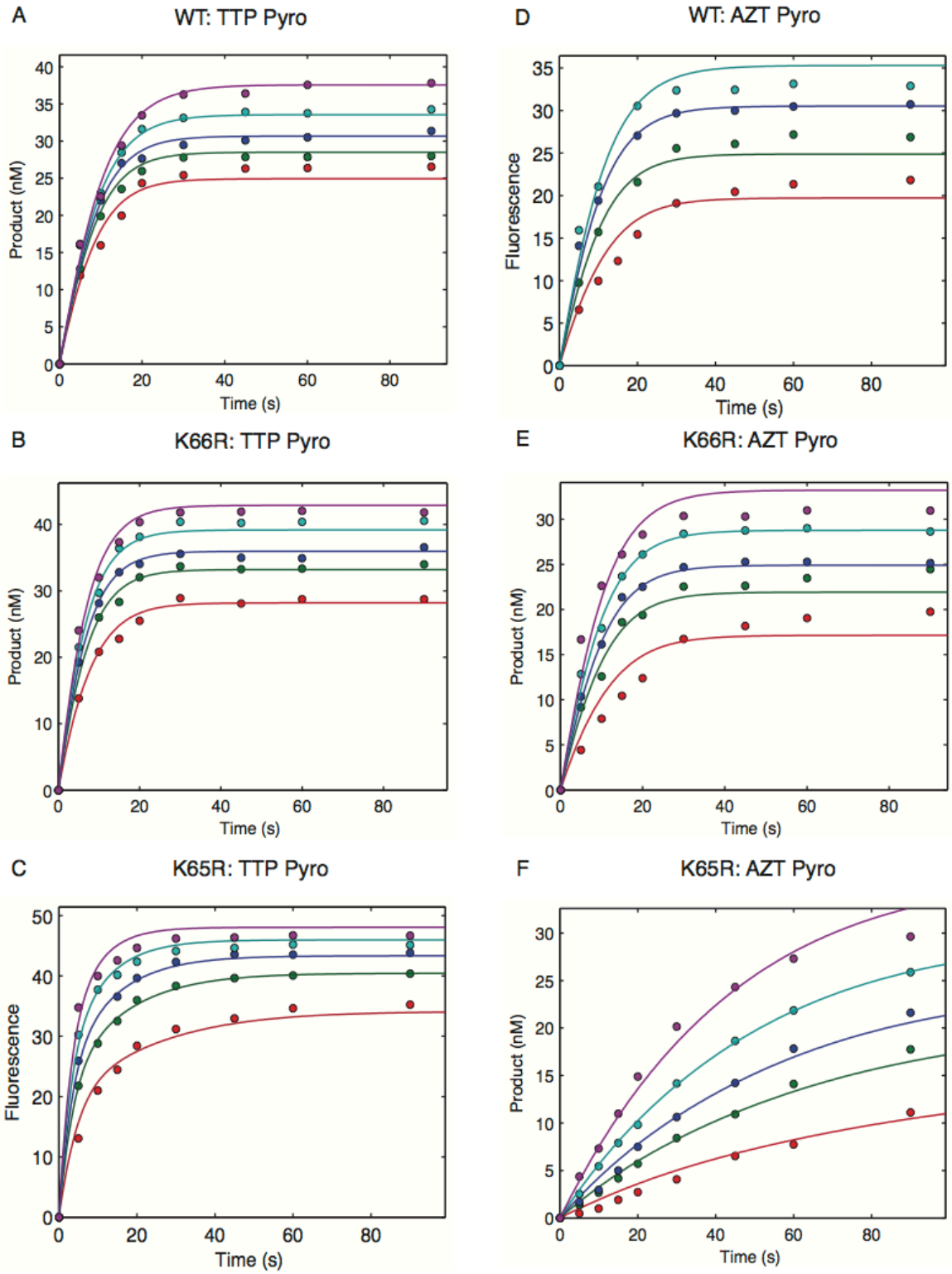
A
WT: TTP Pyro
Product (nM)
Time (s)
D
WT: AZT Pyro
Fluorescence
Time (s)
B
K66R: TTP Pyro
Product (nM)
Time (s)
E
K66R: AZT Pyro
Product (nM)
Time (s)
C
K65R: TTP Pyro
Fluorescence
Time (s)
F
K65R: AZT Pyro
Product (nM)
Time (s)

(Figure 3.2)

Figure 3.2 The concentration dependence of pyrophosphorolysis of TTP- and AZT-terminated primer.

Pyrophosphorolysis experiments were performed by mixing preformed enzyme-DNA complex (75 nM enzyme and 50 nM DNA) with various concentrations of pyrophosphates (100, 200, 300, 500, 1000 μM) at 37 °C. The reaction was quenched by addition of 0.5 M EDTA at various time points. The reactions for pyrophosphorolysis of TTP-terminated primer by wild type, K66R and K65R RT are shown in Figures 1A, 1B, and 1C, respectively. The reactions for pyrophosphorolysis of AZT-terminated primer by wild type, K66R and K65R RT are shown in Figures 1D, 1E, and 1F, respectively.

ATP-mediated AZT Excision

ATP-mediated AZT excision was first investigated by using a *Direct Excision* method (Figure 3.3), which was performed by directly mixing preformed enzyme-DNA complex (26AZT/45-nt DNA substrate) with various concentrations of ATP. The reaction was then measured by monitoring the formation of 25-nt DNA substrate resulting from the ATP-mediated excision of 26-nt AZT. ATP-mediated excision of AZT was also investigated by using the *Excision and Extension* method (Figure 3.3). The experiment was performed by adding AZT into the preformed enzyme-DNA complex (25/45-nt-20AGC DNA substrate) to allow the formation of 26AZT/45-nt. Then, various concentrations of ATP along with 100 μM TTP and 1 μM dCTP were added to allow ATP-mediated excision and primer extension to occur. Production formation was measured by quantifying the formation of 27-nt. Because ATP-mediated excision is rate-limiting relative to the rate of polymerization (k_{cat}/K_m for dNTP incorporation is ~3 to 7 $\mu M^{-1}s^{-1}$) (140), the observed rate here is limited by the rate of ATP-mediated AZT excision. Then, global fitting of two experiments (eg. Figure 3A and 3D) was performed and the data were fit to the model shown in scheme 3.4 where X represents AZT; K_{ATP} represents the apparent dissociate constant ($K_{d,app}$) for ATP binding, k_b represents the maximum rate of excision (k_{exo}) and k_{-b} represents the second order rate constant for the reverse of the excision. All kinetic parameters are well constrained in the global fitting. The results show that K65R mildly decreases the excision efficiency ($k_{exo}/K_{d,app}$) by 1.3-

fold and K66R mildly increases the excision efficiency of ATP-mediated ATP excision by about 1.3-fold. Therefore, both K65R and K66R mutations do not significantly affect the ATP-mediated AZT excision, although their effects are different. The results from our study argue against the hypothesis that K65R significantly decreases the ATP-mediated AZT excision. Although it does affect the binding of ATP by decreasing the $K_{d,app}$ value by 14-fold (Table 3.2), the effect is to increase the apparent ATP binding affinity. Again, because it also decreases the maximum rate of excision (k_{exo}) by 18-fold, the effect of K65R on the efficiency of ATP-mediated AZT excision is not significant.

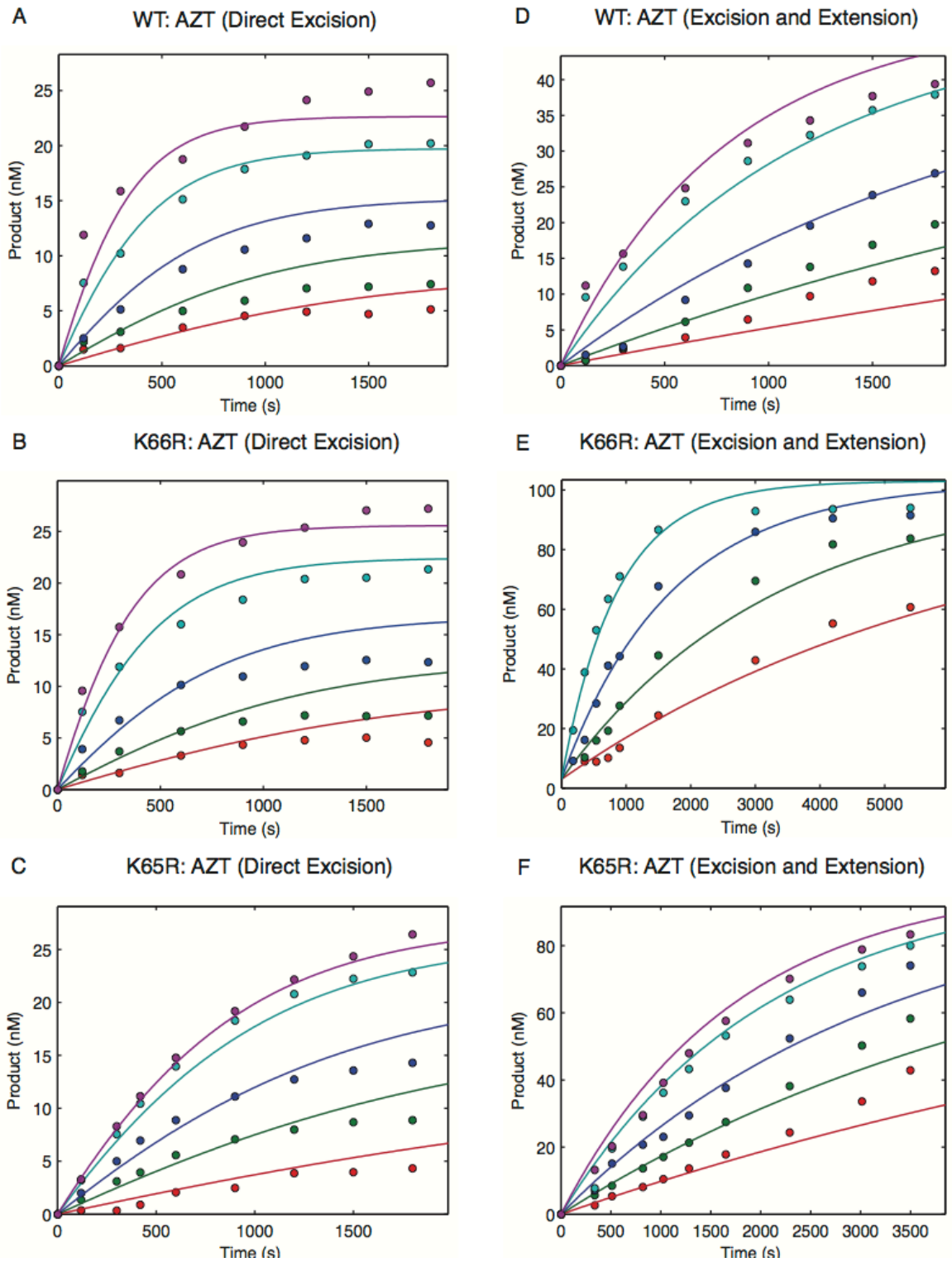
A
WT: AZT (Direct Excision)
D
WT: AZT (Excision and Extension)
B
K66R: AZT (Direct Excision)
E
K66R: AZT (Excision and Extension)
C
K65R: AZT (Direct Excision)
F
K65R: AZT (Excision and Extension)
Product (nM)
Time (s)

(Figure 3.3)

Figure 3.3 The concentration dependence of ATP-mediated AZT excision.

Direct Excision (A, B and C) was performed by mixing preformed enzyme-DNA complex (150 nM enzyme and 100 nM DNA) with various concentrations of ATP (400, 800, 1600, 3200, 4800 μM) at 37 °C. The reaction was quenched by addition of 0.5 M EDTA at various time points. *Excision and Extension* (D, E and F) was performed by mixing preformed enzyme - 25/45-nt DNA complex (150 nM enzyme and 100 nM DNA) with 25 μM AZT at 37 °C for 5 min, followed by adding various concentrations of ATP (400, 800, 1600, 3200, 4800 μM), 100 μM TTP and 1 μM dCTP at 37 °C. The reaction was quenched by addition of 0.5 M EDTA at various time points.

Table 3.3 Kinetic Constants for ATP-mediated AZT and TFV Excision

Drug	Enzyme	k_{exo} (s^{-1} x 10^{-3})	F[d]	$K_{d,app}$ (μM x 10^3)	F[d]	$k_{exo}/K_{d,app}$ ($\mu M^{-1}s^{-1}$ x 10^{-6})	F[d]
AZT	WT	21.2 ± 8.3		50 ± 7.4		0.42 ± 0.18	
	K66R	40 ± 15	0.5 ± 0.3	81 ± 15.7	0.6 ± 0.2	0.5 ± 0.2	0.8 ± 0.5
	K65R	1.2 ± 0.3	18 ± 8	3.67 ± 0.5	14 ± 0.2	0.33 ± 0.09	1.3 ± 0.6
TFV	WT	1.5 ± 0.3		0.31 ± 0.07		4.8 ± 1.7	
	K66R	3.5 ± 0.7	0.43 ± 0.28	0.66 ± 0.13	0.47 ± 0.3	5.3 ± 1.5	0.9 ± 0.4
	K65R	2.1 ± 0.3	0.7 ± 0.24	0.7 ± 0.08	0.44 ± 0.25	3 ± 0.5	1.6 ± 0.4

[d] Fold changes compared with the wild-type enzyme (F[d]: fold decreased)

ATP-mediated TFV Excision

The ATP-mediated TFV excision was investigated by *Excision and Extension* method (Figure 3.4). Experiments were performed by adding TFV into the preformed enzyme-DNA complex (25/45-nt-20TGC DNA substrate) to allow the formation of 26V/45-nt. Then, various concentrations of ATP along with 100 μM dATP and 1 μM dCTP were added to allow the excision and primer extension to occur. The production formation was measured by quantifying the formation of 27-nt and above. The experiment was then fitted to the model shown in scheme 3.4 where X represents TFV,

K_{ATP} represents the apparent dissociate constant ($K_{d,app}$) for ATP binding, k_b represents the maximum rate of excision (k_{exo}) and k_{-b} represents the reverse of the excision. The results in our study show that K65R decreases the specificity constant ($k_{exo}/K_{d,app}$) for TFV excision by 1.6-fold and K66R increases the excision efficiency of TFV by only 1.1-fold. Again, both K65R and K66R mutations do not significantly affect the ATP-mediated TFV excision. Different from ATP-mediated AZT excision, K65R does not significantly affect the binding of ATP. Therefore, our data suggested that NRTI-terminated DNA primer seems to affect ATP binding. Actually, there is more than a 150-fold difference of the apparent dissociation constants ($K_{d,app}$) for ATP binding between the AZT-terminated primer (50 μM) and the TFV-terminated primer (0.3 μM). However, because the value of k_{exo} in ATP-mediated TFV excision is much lower than the value of k_{exo} in ATP-mediated AZT excision, the final difference of $k_{exo}/K_{d,app}$ values between ATP-mediated TFV excision and ATP-mediated AZT excision is reduced to ~10-fold.

In addition, the results in our study suggested that ATP-mediated TFV excision is more efficient than ATP-mediated AZT excision in all three HIVRTs (Table 3.2). A similar trend could also be found in pyrophosphate-mediated excision (Table 3.1), suggesting that pyrophosphorolysis reaction is also more efficient in TFV-terminated primer. Therefore, the results in our study indicated that TFV is more easily excised by HIVRT. Because K65R mutation does not change this property, the enzyme (HIVRT) has to select other mutations, which are specialized on the excision of AZT.

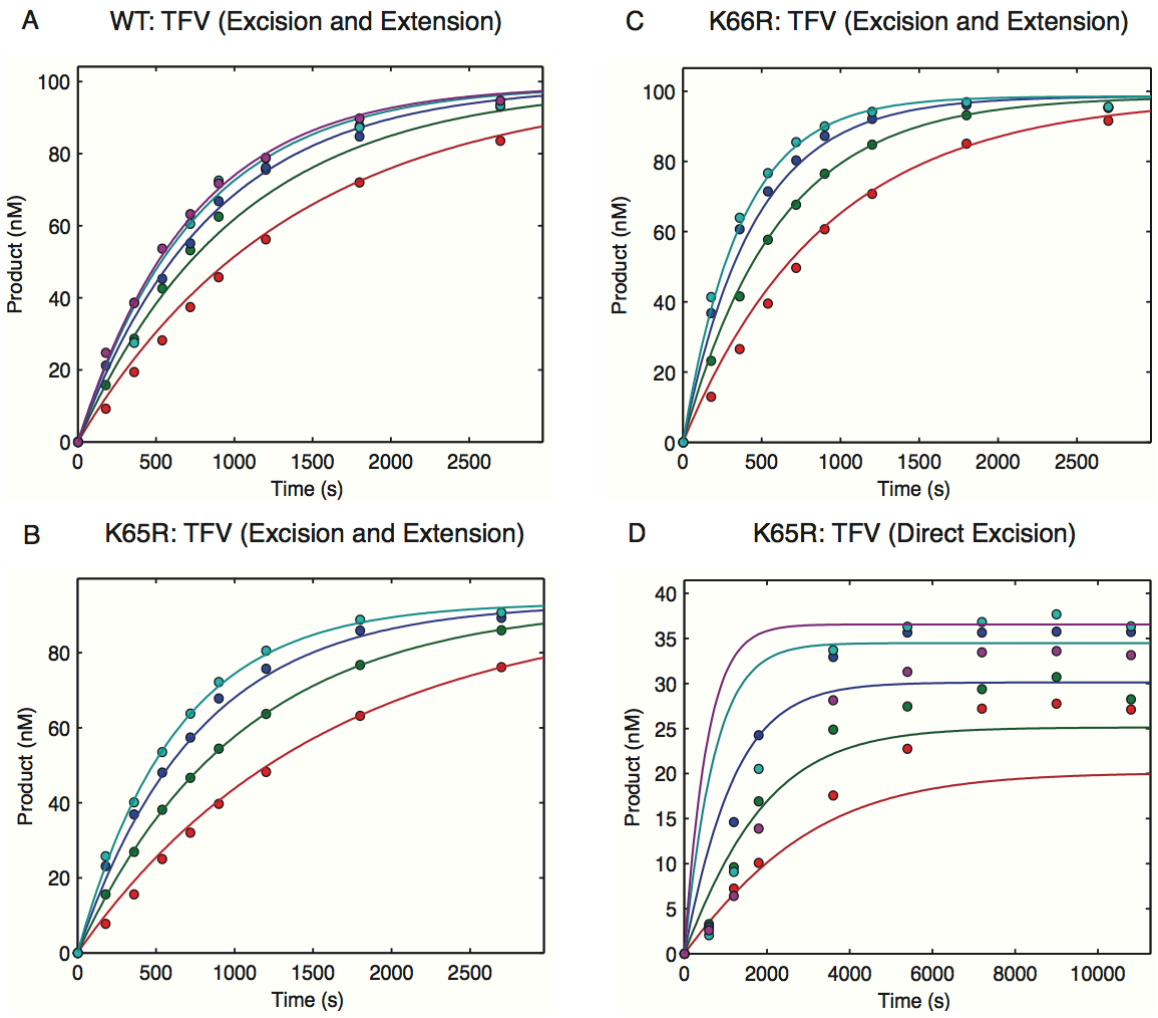

Figure 3.4 The concentration dependence of ATP-mediated TFV excision.

Direct Excision (D) was performed by mixing preformed enzyme-DNA complex (150 nM enzyme and 100 nM DNA) with various concentrations of ATP (400, 800, 1600, 3200, 4800 μM) at 37 °C. The reaction was quenched by addition of 0.5 M EDTA at various time points. *Excision and Extension* (A, B and C) was performed by mixing preformed enzyme - 25/45-nt DNA complex (150 nM enzyme and 100 nM DNA) with 25 μM TFV at 37 °C for 5 min, followed by adding various concentrations of ATP (400, 800, 1600, 3200, 4800 μM), 100 μM dATP and 1 μM dCTP at 37 °C. The reaction was quenched by addition of 0.5 M EDTA at various time points.

Figure 3.5 ATP-mediated TFV excision (Direct excision experiment).

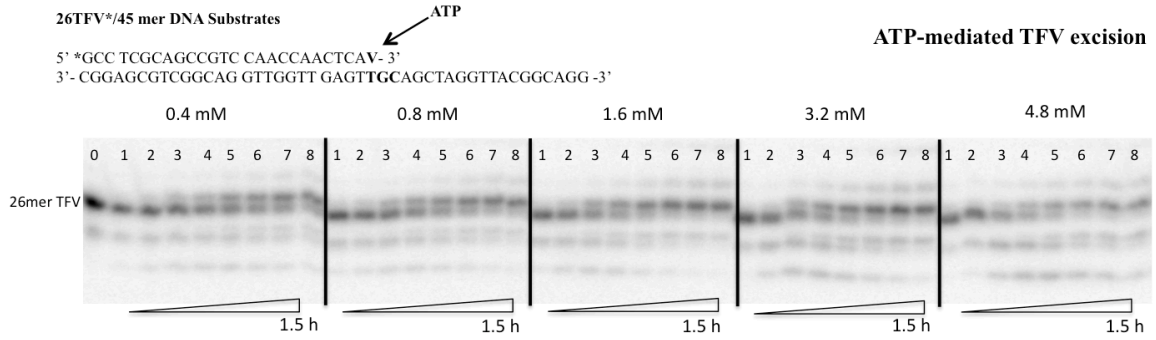

Figure 3.6 ATP incorporation into DNA template.

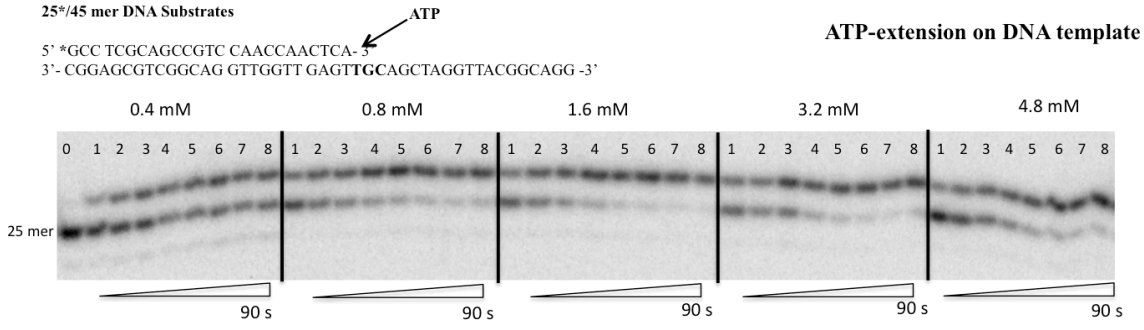

3.4 DISCUSSION

In this chapter, we investigated the effects of two HIVRT mutants (K65R and K66R) on the excision of NRTIs. The results were analyzed using both the conventional fitting and the data simulation. The efficiencies of ATP-mediated TFV excision obtained from conventional fitting were 3.1 x 10^{-6} $\mu M^{-1}s^{-1}$, 3.4 x 10^{-6} $\mu M^{-1}s^{-1}$, and 2.1 x 10^{-6} $\mu M^{-1}s^{-1}$ by wild type, K66R and K65R, respectively. These data show that K65R decreases the efficiency of ATP-mediated TFV excision by about 1.5-fold and K66R increases the efficiency of ATP-mediated TFV excision by about 1.1-fold. Although the results obtained from our data simulation were slightly different from conventional fitting (4.8 x 10^{-6} $\mu M^{-1}s^{-1}$, 5.3 x 10^{-6} $\mu M^{-1}s^{-1}$, and 3 x 10^{-6} $\mu M^{-1}s^{-1}$ by wild type, K66R and K65R, respectively), the conclusions derived from both methods were similar. The slightly different results obtained by conventional fitting are due to errors in fitting to equations derived with simplifying approximations, whereas the global fitting based upon numerical integration of the rate equations is free of such errors. In some instances the data analysis from conventional fitting may not be useful. For example, in the *Direct Excision* experiments, it was seen that the ATP-mediated AZT excision was amplitude dependent, suggesting that the reaction is a highly reversible. If the k_{obs} obtained from the conventional fitting directly was used to calculate the efficiency for excision, the results would be inaccurate because the observed rate here actually includes both the forward rate and the reverse rates. Therefore, the conclusion obtained from the conventional analysis in this case would be misleading. In addition, conventional fitting may not be convenient in defining a complicated situation. For example, a sequential two-steps

reaction in pyrophosphorolysis of AZT-terminated primer (pyrophosphorolysis of AZT-terminated primer followed by pyrophosphorolysis of dATP-terminated primer) could not be easily derived for the conventional fitting. The whole process would be lengthy and error prone. In the data simulation using *KinTek Explorer* software, the results from our experiment were simply fitted to a sequential two-steps model (shown in scheme 2) to directly obtain each kinetic parameter governing pyrophosphorolysis of AZT-terminated primer. More importantly, standard errors for each fitted parameter could be estimated by FitSpace confidence contours analysis. Therefore, the results obtained from data simulation are more accurate and robust.

In the ATP-mediated AZT excision, the *Direct Excision* and *Excision and Extension* experiments were globally fit to define each kinetic parameter governing ATP-mediated AZT excision. In ATP-mediated TFV excision, the *Direct Excision* and *Excision and Extension* experiments could not be globally fit very well as shown in Figure 4B and 4D, due to the challenge of accurately quantifying the excision products from overlapped bands on the gel (Figure 3.5). The reason for the formation of overlapped bands on the gel is that ATP might incorporate into the DNA substrate (25/45-nt-20TGC) after it was formed by the excision of TFV from the end of the primer. We tested this hypothesis by adding various concentrations of ATP directly to a preformed enzyme-DNA complex (using 25/45-nt-20TGC as the DNA substrate) and allowed the reaction to occur at 90s time scale. As a result, about 50% of the 25-nt DNA substrate were extended to 26-nt under 0.4 mM ATP, and almost all of the DNA substrates were extended to 26-nt under 1.6 mM or above concentrations of ATP at 90s

(Figure 3.6), indicating that ATP did incorporate into the DNA strand. The efficiency of ATP incorporation was calculated as 2 x 10^{-4} $\mu M^{-1}s^{-1}$. This efficiency is much lower than the efficiency of dATP incorporation (3.3 $\mu M^{-1}s^{-1}$ in K65R) (140) but much higher than the efficiency of ATP-mediated TFV excision by K65R which is 3 x 10^{-6} $\mu M^{-1}s^{-1}$. Therefore, a complicated situation occurs where ATP also incorporates into the excised DNA template after the excision. Similar phenomenon was not observed in ATP-mediated AZT excision because 26Z/45-nt was used as the DNA substrate in the experiment. In this case, the excised DNA template (25/45-nt-20AGC) was not a good substrate for ATP incorporation because ATP:dATP in theory is a mismatch. *Excision and Extension* method allows us to bypass this problem. After the formation of 26V/45-nt or 26Z/45-nt, various concentrations of ATP were added to the reaction along with 100 μM of the next incoming nucleotide and 1 μM dCTP. Because of the large difference (~ 10^4-fold) in the incorporation efficiencies between ATP and dNTP (TTP or dATP), the excised product extends to 27-nt instead of forming 25-nt-ATP/45-nt and the formation of 27-nt allows us to differentiate the excised and extended product from the pre-excised DNA substrate 26Z/45-nt. Although the next incoming nucleotide (dCTP) of 26V/45-nt or 26Z/45-nt may inhibit the ATP-mediated excision by forming a dead end complex (DEC), the inhibitory effect of the next incoming nucleotide (1 μM dCTP) in this case was small considering its weak binding to 26Z/45-nt ($K_{d,app}$ for dCTP binding to 26Z/45-nt in wild type RT is 273 μM) (An Li and Johnson, Unpublished). We also included the formation of DEC in our complete model (scheme 4) by global fitting to simulate the real

situation in the excision reaction. Therefore, the specificity constant (k_{cat}/K_m) for the forward reaction of ATP-mediated excision was accurately obtained by this method.

Many questions regarding TFV and AZT drug resistance by K65R remain unsolved. It is proposed that a rigid molecular platform formed by R72 and K65R may restrain the conformational adaptability of the HIV reverse transcriptase to discriminate against the incorporation of TFV (96). The hypothesis was tested in our previous study, and the results showed that the main effect of K65R is not to restrain the conformational change of RT upon TFV incorporation, rather to decrease the rate of the chemistry (Chapter 2). In addition, it is also proposed that the rigid molecular platform formed by R72 and K65R may interfere with the positioning of β' and γ' phosphates of the ATP at the active site and hence reduces the efficiency of ATP-mediated excision (96). In this study, we investigated the effect of K65R mutation on ATP-mediated excision by using two NRTIs. The results indicate that K65R does not significantly affect the efficiency of ATP-mediated NRTIs excision, but rather affects the efficiency of pyrophosphate-mediated NRTIs excision. In addition, the result in our study showed that K65R does affect the binding of ATP on ATP-mediated AZT excision but it does not affect the binding of ATP on TFV excision, suggesting NRTIs in the end of DNA primer has some effects on the binding of ATP. Different from what has been proposed, our data suggested that K65R does not weaken the binding of ATP, but tightens ATP binding by about 14-fold in the ATP-mediated AZT excision. However, a tighter binding does not necessarily lead to a more efficient catalysis in this case. K65R decreases the value of k_{exo} by around 18-fold, which make the final $k_{exo}/K_{d,app}$ value of this mutant comparable to

that of wild type enzyme. It has been suggested that the mutation of K65R increases the susceptibility for AZT by highly decreasing ATP-mediated excision, which leads to the phenomenon that K65R only displays resistance to TFV but not to AZT (96, 98-100). The results in our previous study indicated that the mutation of K65R has a similar drug resistance against TFV and AZT incorporation from discrimination mechanism (Chapter 2). The results in this study show again that the mutation of K65R has a similar effect on ATP-mediated TFV and AZT excision.

ATP-mediated excision occurs by attacking the phosphodiester bond between the penultimate nucleotide and the NRTI at the 3' end of the primer (102). It is also reported that K66 locates adjacent to the penultimate nucleotide and K66 mutations influence both the mismatch extension and mis-insertion rates of HIV-1 reverse transcriptase (97). Therefore, the significance of this mutation on drug resistance, especially for excision, should not be overlooked although there were a few reports suggesting drug resistance associated with K66R. The results from this study showed that K66R mutation does not significantly affect ATP-mediated TFV or AZT excision. The study performed here also provides a good method to estimate any possible future resistance.

Pyrophosphorolysis (or pyrophosphate-mediated excision) is the reaction that pyrophosphate attacks the monophosphate group between the last and penultimate nucleotides in the 3' end of the primer, causing the excision of the last nucleotide. If the last nucleotide is replaced by NRTIs in a chain termination reaction, pyrophosphorolysis will excise the inhibitor from the template and restore the polymerization ability of RT. In this study, we investigated pyrophosphorolysis of both normal nucleotides (TTP and

dATP) and NRTIs (AZT and TFV) terminated primers by three HIVRTs. The results showed that the efficiencies of pyrophosphorolysis of AZT-terminated primer are lower than that of pyrophosphorolysis of TTP-terminated primer. Compared with wild type and K66R, this trend is most obvious in K65R (around 24-fold difference). Although the efficiencies of pyrophosphorolysis of TFV-terminated primer are comparable to or higher than that of pyrophosphorolysis of dATP-terminated primer in wild type and K66R, it is about 12-fold lower in K65R. Therefore, the mutation of K65R highly decreases the efficiencies of pyrophosphorolysis in NRTIs (TFV and AZT) terminated primers, suggesting that K65R may not prefer the pyrophosphate-mediated excision to excise NRTIs and cause the drug resistance in the physiological condition. In addition, the results in our study suggest that there are no big differences of the efficiency of ATP-mediated excision between K65R mutant and wild type HIVRT, suggesting that K65R may not prefer ATP-mediated excision to excise NRTIs in the physiological condition. The results from our study partially explained why K65R was selected as the most common mutation for discrimination rather than excision.

Our data also show that the efficiencies of pyrophosphorolysis are around 10^3 fold lower than the efficiencies of the incorporation. Because of the physiological concentrations of pyrophosphate and dNTP are about 150 μM and 30 μM, respectively (136, 139), the incorporation of a natural nucleotide is around several hundred more likely than its removal by pyrophosphorolysis. Therefore, in the presence of the next incoming nucleotide, the enzyme chooses to perform polymerization rather than pyrophosphorolysis. And in the absence of the next incoming nucleotide or in the

conditions that the next incoming nucleotide could not be incorporated (i.e NRTIs terminated primer), the enzyme performs pyrophosphate-mediated excision to remove the terminal dNTP or NRTIs.

The identity of the specific substrate for NRTI excision has long been debated. Many believe that ATP-mediated excision is the primary excision *in vivo* (102, 120, 134, 135), because the observed rates for ATP-mediated NRTIs excision in wild type RT and TAMs mutant were quite different while the observed rates for pyrophosphate-mediated NRTIs excision were comparable (120, 135). However, most of the prior experiments were performed under only one concentration of ATP or pyrophosphate and therefore their conclusions were based the specific excision rates calculated under that special concentration. It is true that the maximum excision rate (k_{exo}) is an important kinetic parameter, but the specificity constant ($k_{exo}/K_{d,app}$) for excision is a more important parameter because it directly tells the efficiency of the excision reaction. Our recent studies show that there is only around 5-fold difference in the efficiencies of ATP-mediated AZT excision between wild type RT and TAMs mutants (An Li and Johnson, unpublished). On the other hand, the results from this study suggest that the efficiency of pyrophosphate-mediated excision is around 10^3-fold higher than the efficiency of ATP-mediated excision. Therefore, even considering the fact that the physiological concentration of ATP (~3.2 mM) is much higher than pyrophosphate (~150 μM) (136, 139), pyrophosphate still seems to be a better substrate for excision than ATP. Some others claimed that ATP-mediated NRTIs excision is the primary excision *in vivo* because the product of pyrophosphate-mediated excision is NRTIs which could be

efficiently reincorporated back into the viral DNA by RT, but the product of ATP-mediated excision (AZTp4A) could not (134). However, it is also reported that the product of ATP-mediated excision (AZTp4A) is also a very efficient substrate for incorporation (141). In addition, the cellular enzyme asymmetric diadenosine 5′, 5‴-P1, P4-tetraphosphatase (Ap4A) hydrolase could catalyze the hydrolysis of AZTp4A to regenerate AZT (142). Therefore, ATP seems to not have much advantage over pyrophosphate serving as the primary substrate for the excision reaction. In addition, the efficiencies of TTP and AZTTP incorporation are actually comparable. Considering the local TTP concentration is much higher than the excised AZTPP concentration, the possibility for AZTTP reincorporation would be very small. Therefore, the results in our study suggested that the primary donor for NRTIs excision may not be always be ATP. In other words, both pyrophosphate-mediate excision and ATP-mediated excision might contribute to the NRTIs excision. The specific contribution from each excision could be calculated by using the specificity constants (Table 3.4) times the physiological concentrations of excision substrates. For the excision of AZT in the wild type RT, we found that pyrophosphate-mediated excision is about 90-fold more likely to be the primary excision than the ATP-mediated excision. For the excision of TFV in the wild type RT, pyrophosphate-mediated TFV excision is about 35-fold more likely to be the primary excision than the ATP-mediated TFV excision. But for TFV excision by K65R mutant, the contributions of two excisions are actually comparable. The rates for pyrophosphate-mediated excision and ATP-mediated excision are 7.5×10^{-3} s^{-1} and 9.6×10^{-3} s^{-1}, respectively. Therefore, our data suggested that either pyrophosphate or ATP

could be the primary substrate for excision, and different enzymes may have different primary excision substrates.

Table 3.4 Specificity Constants Comparison for WT, K66R, and K65R

E	dNTP	Incorporation k_{cat}/K_m ($\mu M^{-1}s^{-1}$)	Pyrophorolysis k_{cat}/K_m ($\mu M^{-1}s^{-1}$ x 10^{-3})	$K_{eq,Incorp}$ x 10^3	Excision, ATP, (F) k_{cat}/K_m ($\mu M^{-1}s^{-1}$ x 10^{-6})	Excision, ATP, (R) k_{cat}/K_m ($\mu M^{-1}s^{-1}$)	$K_{eq,Exo}$ x 10^3
WT	TTP	7.3 ± 0.5	3.1 ± 0.7	2.4	–	–	–
	AZT	8.4 ± 1	0.8 ± 0.2	10.5	0.42 ± 0.18	0.065 ± 0.002	155
K66R	TTP	7.3 ± 0.2	1.9 ± 0.25	3.8	–	–	–
	AZT	3 ± 0.1	0.7 ± 0.16	4.3	0.5 ± 0.2	0.073 ± 0.018	146
K65R	TTP	3.3 ± 0.1	1.7 ± 0.3	1.9	–	–	–
	AZT	0.6 ± 0.1	0.07 ± 0.01	8.6	0.33 ± 0.09	0.018 ± 0.004	55
WT	dATP	8.2 ± 3.2	1.7 ± 0.4	4.8	–	–	–
	TFV	2.1 ± 0.1	3.6 ± 0.3	0.6	4.8 ± 1.7	–	–
K66R	dATP	9.8 ± 2.5	1.8 ± 0.36	5.4	–	–	–
	TFV	1.1 ± 0.1	8.3 ± 1.4	0.1	5.3 ± 1.5	–	–
K65R	dATP	3.3 ± 0.2	0.6 ± 0.14	5.5	–	–	–
	TFV	0.11 ± 0.01	0.05 ± 0.004	2	3 ± 0.5	–	–

Note: "E" is short for "Enzyme"; "$K_{eq,incorp}$" indicates the calculated K_{eq} (k_{cat}/K_m for dNTP or drugs incorporation divided by k_{cat}/K_m for dNTP or drugs pyrophosphorolysis) for Incorporation; "Excision, ATP, (F)" indicates the ATP-mediated excision; "Excision, ATP, (R)" indicates the reverse of ATP-mediated excision or the incorporation of Xp4A; "$K_{eq,Exo}$" indicates the calculated K_{eq} (k_{cat}/K_m for the Xp4A incorporation divided by k_{cat}/K_m for ATP-mediated excision) for excision.

Finally, we calculated the apparent equilibrium constants (K_{eq}) governing nucleotide and NRTI incorporation, and ATP-mediated NRTIs excision (Table 3.4). Although AZT and TFV are analogs of TTP and dATP, the apparent K_{eq} values for AZT and TFV incorporations are different from TTP and dATP incorporations. In addition, the apparent K_{eq} values for AZT and TFV incorporations are also different between wild type RT and mutants. The reason that we use the terminology of apparent K_{eq} instead of K_{eq} is that K_{eq} value for a reaction is solely determined by the equilibrium concentrations of reagents and products. The value of K_{eq} cannot be changed by enzyme. In our case, the apparent K_{eq} for normal nucleotide incorporation is determined by the ratio of $[ED_{n+1}]/[ED_n]$ times the ratio of $[PP_i]/[dNTP]$, and the apparent K_{eq} for AZT incorporation is determined by the ratio of $[ED_{n+AZT}]/[ED_n]$ times the ratio of $[PP_i]/[AZT]$. Therefore, NRTIs (AZT and TFV) and mutants may influence the apparent K_{eq} by changing translocation dynamic between the pre-translocation site (nucleotide-binding site or N site) and post-translocation site (primer-binding site or P site). For example, our recent studies show that AZT terminated primer shifts the translocation equilibrium to favor the pre-translocation complex (143), and TAMs mutations also influence the translocation equilibrium (An Li and Johnson, unpublished). In addition, we found that the apparent K_{eq} for ATP-mediated AZT excision is much higher than the apparent K_{eq} for nucleotide and NRTIs incorporation. This is reasonable because the incorporation and ATP-mediated excision are different reactions. Even if we compare the reverse of ATP-mediated AZT excision with AZT incorporation, they are also different

because the incorporation substrate for the reverse of ATP-mediated AZT (AZTp4A) is actually a chemical combination of ATP and AZT and therefore the reaction of AZTp4A incorporation is similar to a combination of two chemical reactions of AZT or dNTP incorporation.

In summary, we studied the effects of two mutants (K65R and K66R) on both pyrophosphate-mediated and ATP-mediated excision. The result in our study suggested that both mutants do not significantly affect the excision of a natural nucleotide in the normal DNA template. If the DNA template is terminated with an NRTI, K65R does not affect the efficiency of ATP-mediated NRTIs excision, but does affect the efficiency of pyrophosphate-mediated NRTIs excision. In addition, the efficiencies of pyrophosphate-mediated excision and ATP-mediated excision were also compared. As a result, it is suggested that pyrophosphate-mediated excision is about 10^3-fold more efficient than ATP-mediated excision. But this does not necessary suggest that pyrophosphate is a better excision substrate *in vivo* than ATP. Actually, either pyrophosphate or ATP could be the primary substrate for excision, and different situation may have different primary excision substrate. Finally, the apparent equilibrium constants (K_{eq}) values for each reaction were calculated. The results from our studies indicated that NRTIs or RT mutants may influence the apparent K_{eq} by changing the translocation equilibrium. Our studies performed here not only facilitated a better understanding on the effects of K65R on NRTIs (AZT and TFV) resistance, but also provided valuable information to compare the efficiencies of different chemical reactions in many enzymes.

Chapter 4: Kinetics Thermodynamics Governing the Roles of Two Metal Ions in Nucleotide Specificity by DNA Polymerases

4.1 INTRODUCTION

Metal ions play critical roles in many cell biological activities including DNA replication, DNA repair, and transcription. They stabilize the structures of proteins and nucleic acids, and promote the catalytic activities of many enzymes (144). Magnesium (Mg^{2+}) ion, due to its natural abundance *in vivo* and limited coordination geometry conferring high specificity, serves as the primary metal ion for catalysis by many enzymes (145). The function of metal ions in DNA polymerization and hydrolysis was described by Thomas A. Steitz and Joan A. Steitz in 1993 (105) as a general two-metal-ion mechanism. In this proposal, metal ions A and B are referred to as the catalytic and nucleotide bound metal ions, respectively. Metal ion A reduces the pKa of the 3'-OH group for polymerization or a H_2O molecule for hydrolysis, thereby activating the nucleophile and bringing it close to the α phosphate at the reaction center. During DNA polymerization, metal ion B forms a tight complex with the incoming nucleotide (K_d = 28.7 μM) and binds to the enzyme as a $[Mg\text{-}dNTP]^{2-}$ coordinating with all three phosphates (α, β, and γ) (146, 147). The coordination among two metal ions, water molecules, and several surrounding acidic residues helps to stabilize the transition state by neutralizing the developing negative charge. After product formation, metal ion B is also thought to facilitate pyrophosphate release (105). The two-metal-ion mechanism is supported by many crystal structures in DNA polymerases. However, crystal structures in most cases only provide a stationary picture for the active site and therefore do not reveal the dynamic movement of the metal ions during the catalysis. In addition, dideoxy-

terminated primer, calcium ions, or non-hydrolysable nucleotide analogs are usually used in crystal structures to prevent catalysis, which disrupts the active site geometry and may affect the conformational change of the enzyme. To further investigate the two-metal-ion mechanism, studies on dynamics of the metal ions in biological relevant conditions are required.

DNA polymerases are divided into seven families (A, B, C, D, X, Y and RT). It appears to be universal that most of the DNA polymerases use the two-metal-ion mechanism to perform catalysis. HIV reverse transcriptase (HIVRT), due to its own advantages, serves as a good candidate for studying the two-metal-ion mechanism. First, many crystal structures of HIVRT have been published in the past decades, which allows us to directly observe the coordination of the two Mg^{2+} ions in the active site. In addition, the biochemical characterization of single nucleotide incorporation has been well established in HIVRT (124, 126), which provides a basis for studying the effects of the Mg^{2+} on nucleotide incorporation. Recently, we have developed a method where HIVRT was labeled with an environmentally-sensitive fluorophore at a position in the fingers domain so that the dynamics of the enzyme conformational changes upon nucleotide binding and incorporation can be directly observed (126, 148). This method allows us to monitor the conformational change of HIVRT during a single nucleotide incorporation event. In this chapter, we studied the effects of Mg^{2+} on nucleotide incorporation by investigating each step including ground state binding, conformational change, chemistry and pyrophosphate release.

Nucleotide specificity, as one of the most important kinetic parameters, has also been studied very well in HIVRT to establish the following minimal pathway shown below.

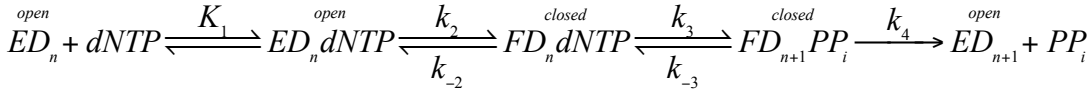

Scheme 4.1 Pathway of DNA polymerization.

The minimal reaction pathway is shown where ED_n and FD_n represent the enzyme-DNA complex in the open and closed states, respectively, as observed in crystal structures and monitored by the fluorescent probe attached to the fingers domain.

The conformational change is much faster than chemistry, but the specificity constant (k_{cat}/K_m) is modulated by the rate of the reverse of the conformational change (k_{-2}) relative to the rate of the chemistry (k_3). If $k_{-2} >> k_3$, the ground state binding and conformational change come to equilibrium and the specificity constant is governed by the product of binding constants and the rate of chemistry ($k_{cat}/K_m = K_1K_2k_3$). If $k_{-2} << k_3$, the nucleotide binding fails to comes to equilibrium and the rate of chemistry does not contribute to the specificity constant ($k_{cat}/K_m = K_1k_2$) (126). In this chapter, the effects of Mg^{2+} on the nucleotide specificity will be studied.

For decades, it was very challenging to dissect roles of the two Mg^{2+} ions due to the convoluted concentration dependence for Mg^{2+} binding to the enzyme and nucleotide (Table 4.2). In this chapter, we present a method to accurately define concentrations of free Mg^{2+} and free $[Mg.dNTP]^{2-}$ in solution using a Mg-EDTA buffer in order to examine the activities and roles of each Mg^{2+}. It is known that two Mg^{2+} are bound in the active site and involved in the catalysis, but many details about their activities are still unknown. For example, what is the binding affinity and order of binding the two Mg^{2+}? How does each of the Mg^{2+} ion affect the natural nucleotide incorporation each step including ground state binding, conformational change, chemistry, and pyrophosphate release? Finally, how does the Mg^{2+} affect the nucleotide specificity? In this study, we addressed

these questions by examining the Mg^{2+} concentration dependence of each step in the reactions pathway. The studies performed here provide new insights toward understanding the classical two-metal-ion mechanism.

4.2 METHODS

Mutagenesis, Expression and Purification of MDCC-labeled HIVRT

HIVRT protein was expressed, purified and labeled as previous described (123). Briefly, the p51 and p66 subunits of HIVRT were separately expressed and then cells were combined to yield a 1:1 ratio of the two subunits, lysed, sonicated and then the heterodimer was purified. The protein was first purified by using the tandem Q-Sepharose and Bio-Rex70 columns, and further purified by using single-stranded DNA (ssDNA) affinity column. Then, the protein was labeled by MDCC fluorophore and the unreacted MDCC was removed by Bio-Rex70 column. After purification, 'Coomassie Plus' protein assay was used to determine the purified protein concentration. In addition, an active site titration experiment was also performed to determine the active site concentrations of the purified protein (148).

Prepare DNA Substrates for Kinetic Studies

The 25/45nt and 25ddA/45nt DNA substrates (Table 4.1) were purchased from Integrated DNA Technologies. The oligonucleotides were annealed by heating at 95°C for 5 minutes and followed by slow cooling to room temperature. For making radiolabeled primer, the 25-nt oligonucleotide was labeled at the 5' end by γ-^{32}P ATP (PerkinElmer) using T4 polynucleotide kinase (NEB).

Table 4.1 DNA substrates for kinetic studies

25/45nt	
25nt:	5′-GCCTCGCAGCCGTCCAACCAACTCA-3′
45nt:	5′-CGGAGCGTCGGCAGGTTGGTTGAGT**A**GCAGCTAGGTTACGGCAGG-3′
25ddA/45nt	
25nt:	5′-GCCTCGCAGCCGTCCAACCAACTCA$_{dd}$-3′
45nt:	5′-CGGAGCGTCGGCAGGTTGGTTGAGT**A**GCAGCTAGGTTACGGCAGG-3′

Quench Flow Kinetic Assays

Quench flow experiment was performed by rapidly mixing a preformed enzyme-DNA complex (using radio-labeled DNA substrate) with various concentrations of incoming nucleotide using KinTek RQF-3 instrument (KinTek Corp.). The reaction was quenched by the addition of 0.5 M EDTA at varying time points. Products were collected and separated on 15% denaturing PAGE (acrylamide (1:19 bisacrylamide), 7M Urea). Results were then analyzed by ImageQuant 6.0 software (Molecular® Dynamics).

Stopped Flow Kinetic Assays

The stopped flow measurements were performed by rapidly mixing an enzyme-DNA complex (MDCC-labeled HIVRT) with various concentrations of incoming nucleotide. The time dependence of fluorescence change upon nucleotide binding and incorporation was monitored using an AutoSF-120 stopped-flow instrument (KinTek Corp., Austin, TX) by exciting the fluorophore at 425 nm and monitoring the fluorescence change at 475 nm using a single band-pass filter with a 25 nm bandwidth (Semrock).

Global Fitting of Multiple Experiments

The kinetic parameters governing each step in nucleotide incorporation obtained from all four experiments (stopped flow, chemical quench, nucleotide off-rate, and pyrophosphate release) were globally fitted to the model shown in scheme 4.1 by *KinTek Explorer* software (KinTek Corp., Austin, TX). FitSpace confidence contours were also performed for standard error estimation.

Free Mg^{2+} Concentration Calculation

To calculate the free Mg^{2+} concentration in solution, EDTA (500 μM) was added to serve as a buffering system. The main equilibria that affect free Mg^{2+} concentration are the equilibrium constants for Mg^{2+} binding to dNTP, Mg^{2+} binding to EDTA, and the equilibrium for protons binding to dNTP (shown in Table 4.2). Calculation of the free Mg^{2+} concentration from starting total concentrations of Mg^{2+}, dNTP and EDTA and the pH requires an iterative approach to solve simultaneously the equilibria involved (reference). However, we simplified the problem by specifying the free Mg^{2+} concentration and total EDTA concentration, and then calculating the total concentrations of Mg^{2+} and dNTP that are required to add to the solution using a simplified equation (shown in equation 4.1 and 4.2). To confirm the accuracy of our calculation, the reactions were simulated with all equilibria (shown in Table 4.2) (146, 147) using *KinTek Explorer* software. In this case, starting total concentrations of Mg^{2+}, dNTP and EDTA were inputted, and the free Mg^{2+} concentration in the solution was directly observed after the system reached equilibrium.

Scheme 4.2 Main equilibria that affect free Mg^{2+} concentration in solution

$$Mg + dNTP \overset{K_1}{\rightleftharpoons} Mg.dNTP$$

$$Mg + EDTA \overset{K_2}{\rightleftharpoons} Mg.EDTA$$

$$H + dNTP \overset{K_3}{\rightleftharpoons} H.dNTP$$

Equation 4.1 Equations for calculating free Mg^{2+} concentrations 1

$$[Mg.dNTP] = \frac{[Mg] \cdot [dNTP]}{K_1}$$

$$[Mg.EDTA] = \frac{[Mg] \cdot [EDTA]}{K_2}$$

$$[H.dNTP] = \frac{[H] \cdot [dNTP]}{K_3}$$

Equation 4.2 Equations for calculating free Mg^{2+} concentrations 2

$$[Mg]_0 = [Mg] + [Mg.dNTP] + \frac{[EDTA]_0}{1 + K_2 / [Mg]}$$

$$[dNTP]_0 = [Mg.dNTP] \cdot (1 + (K_1 / [Mg]) \cdot (1 + [H] / K_3))$$

Table 4.2 Kinetic Constants Used for the Calculation of Free Magnesium Concentration in Solution

Equilibria	K_a (M^{-1})	K_d (μM)
$Mg^{2+} + ATP^{4-} \rightleftharpoons [Mg.ATP]^{2-}$	34800	28.7
$H^{+} + ATP^{4-} \rightleftharpoons [H.ATP]^{3-}$	1.09×10^{7}	9.17×10^{-2}
$H^{+} + [HATP]^{3-} \rightleftharpoons [H_2.ATP]^{2-}$	8500	118
$Mg^{2+} + EDTA^{4-} \rightleftharpoons [Mg.EDTA]^{2-}$	4×10^{8}	0.25×10^{-2}
$H^{+} + EDTA^{4-} \rightleftharpoons [H.EDTA]^{3-}$	1.66×10^{10}	6×10^{-5}
$H^{+} + [HEDTA]^{3-} \rightleftharpoons [H_2.EDTA]^{2-}$	1.58×10^{6}	0.633
$Mg^{2+} + [HATP]^{3-} \rightleftharpoons [Mg.HATP]^{-}$	542	1845

Note: In the presence of 500 μM EDTA and at pH 7, main equilibria in solution affect free magnesium concentration are shown above. The association constant (K_a) and dissociation constant (K_d) are obtained from (Storer AC, *et al.,* 1976; Martell *et al.,* 1964) (reference (146, 147)).

4.3 RESULTS

Nucleotide bound Mg^{2+} binds much tighter than catalytic Mg^{2+}

To study the binding of $[Mg.TTP]^{2-}$ to HIVRT, we first labeled HIVRT with N-[2-(1-maleimidyl)ethyl]-7-(diethylamino) coumarin-3-carboxamide (MDCC) at the fingers domain as described before (126). The fluorescence change upon nucleotide binding was recorded using a stopped flow instrument by rapidly mixing various concentrations of $[Mg.TTP]^{2-}$ (0.5, 1, 2, 4, 10, and 20 μM) with a preformed enzyme-DNA complex (100 nM MDCC-labeled HIV-1 wild type RT and 150 nM 25ddA/45nt DNA) in the presence of 10 mM Mg^{2+}. Because the primer of the DNA template is a dideoxy-terminated, it only allows the binding of $[Mg.TTP]^{2}$, preventing chemistry. The $[Mg.TTP]^{2-}$ binding is hence indicated by the time dependent the fluorescence change (Figure 4.1A). To better define the binding affinity of $[Mg.TTP]^{2-}$ to HIVRT, an equilibrium titration assay was also performed. The experiment was performed by titrating the preformed enzyme-DNA complex with varying concentrations of $[Mg.TTP]^{2-}$ ranging from 0 to 20 μM. The amplitude of fluorescence signal decreases as $[Mg.TTP]^{2-}$ concentration increases (Figure 4.1B). Global fitting of two experiments simultaneously to the model shown in scheme 4.3 allows us to accurately define the dissociation constant (K_d) for $[Mg.TTP]^{2-}$ as well as the rate constants governing binding. The net K_d value was calculated as 0.67 μM using equation 4.3 to account for the two-step binding reaction.

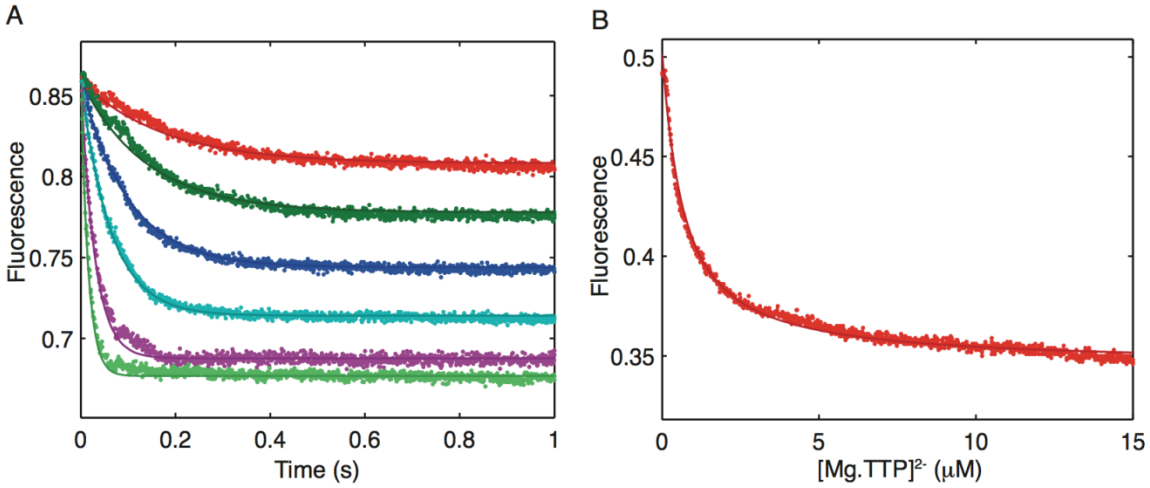

Figure 4.1 $[Mg.TTP]^{2-}$ binding and dissociation in the presence of 10 mM Mg^{2+}.

Binding of $[Mg.TTP]^{2-}$ (on-rate) was measured by stopped flow assay (A). The experiments were performed by rapidly mixing various concentrations (0.5, 1, 2, 5, 10, and 20 μM) of $[Mg.TTP]^{2}$ with a preformed enzyme-DNA complex (100 nM MDCC-labeled HIV-1 wild type RT and 150 nM DNA) in the presence of large excess of free Mg^{2+} (10 mM). Binding of $[Mg.TTP]^{2-}$ to HIVRT was also measured by equilibrium titration (B). The experiment was performed by titrating the preformed enzyme-DNA complex with varying concentrations of $[Mg.TTP]^{2-}$ ranging from 0 to 20 μM. Global fitting of two experiments simultaneously to the model shown in Scheme 4.1 allows us accurately defining the binding affinity of $[Mg.TTP]^{2-}$.

Scheme 4.3 Simplified model for $[Mg.TTP]^{2-}$ binding

$$ED_{dd} + [Mg.TTP]^{2-} \underset{}{\overset{K_1}{\rightleftharpoons}} ED_{dd}.[Mg.TTP]^{2-} \underset{}{\overset{K_2}{\rightleftharpoons}} FD_{dd}.[Mg.TTP]^{2-}$$

Equation 4.3 The net K_d calculation for two-steps binding

$$K_{d,net} = \frac{1}{K_1\left(1+K_2\right)}$$

The binding of the catalytic Mg^{2+} to HIVRT was measured by examining the Mg^{2+} concentration dependence of the rate of catalysis in a single turnover. The experiment was performed by mixing enzyme and DNA with $[Mg.TTP]^{2-}$ solutions containing a fixed concentration of $[Mg.TTP]^{2-}$ (150 μM) and various concentration of free Mg^{2+} (ranging from 0.25 to 10 mM). The rates of chemistry, measured by rapid-quench and stopped flow methods, were observed for each reaction and plotted as a function of free Mg^{2+} concentrations (Figure 4.2). The data were fit to a hyperbola and the apparent dissociation constant ($K_{d,\ app}$) of catalytic Mg^{2+} binding to HIVRT was

obtained as 3.7 mM. Compared with the binding of $[Mg.TTP]^{2-}$, the binding affinity of catalytic Mg^{2+} ion is more than 5000-fold weaker.

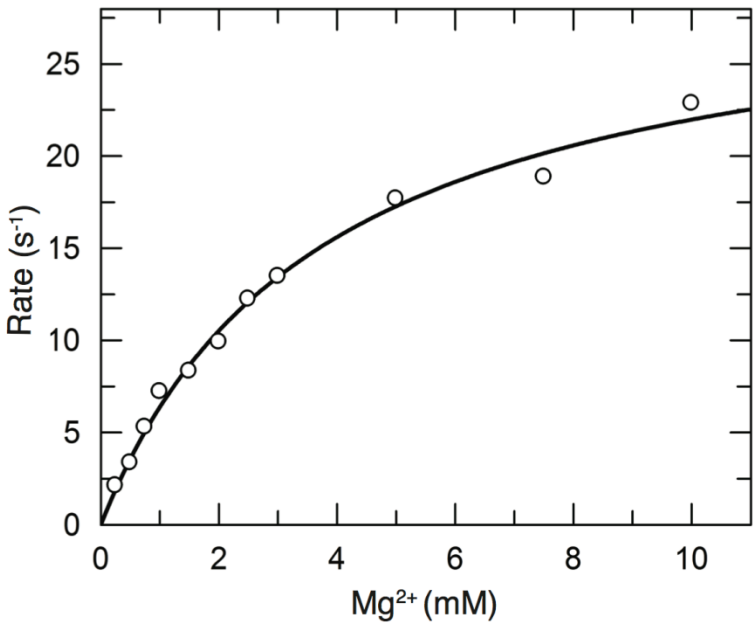

Figure 4.2 Mg^{2+} dependent catalytic activity of HIVRT.

The experiment (stopped flow) was performed by first mixing enzyme and DNA to form an ED complex, followed by rapid mixing with solutions containing a fixed concentration of $[Mg.TTP]^{2-}$ (150 μM) and various concentrations of Mg^{2+} ions (ranging from 0.25 to 10 mM). The observed rate of chemistry as a function of free Mg^{2+} concentrations was fit to a hyperbolic equation to obtain the maximal rate of Mg^{2+} dependent chemistry and the apparent dissociation constant ($K_{d,\,app}$) for Mg^{2+} binding to the enzyme to catalyze the reaction.

Nucleotide bound Mg^{2+} is required for the enzyme closing.

To study whether the nucleotide bound Mg^{2+} is required for the nucleotide-induced conformational change from the open to the closed state, a preformed enzyme-DNA complex (100 nM MDCC-labeled HIV-1 wild type RT and 150 nM 25ddA/45nt DNA) was rapidly mixed with either 50 μM TTP or $[Mg.TTP]^{2-}$. The change of fluorescence upon TTP or $[Mg.TTP]^{2-}$ binding was monitored by stopped flow methods. The results showed that it is $[Mg.TTP]^{2-}$ rather than TTP that induces the conformational change of HIVRT (Figure 4.3). In addition, the experiment was repeated with 2 μM $[Rh.TTP]^{2-}$, and the decrease of the fluorescence was also observed (Figure 4.4), indicating that nucleotide bound metal ion is required for the enzyme closing. Because $[Rh.TTP]^{2-}$ is exchange inert, it also indicates that nucleotide bound Mg^{2+} itself is sufficient for inducing the enzyme closing. Our results suggest that nucleotide bound Mg^{2+} plays a critical role in the conformational change of the enzyme. Another interesting question is that whether catalytic Mg^{2+} also plays a role in the conformational change.

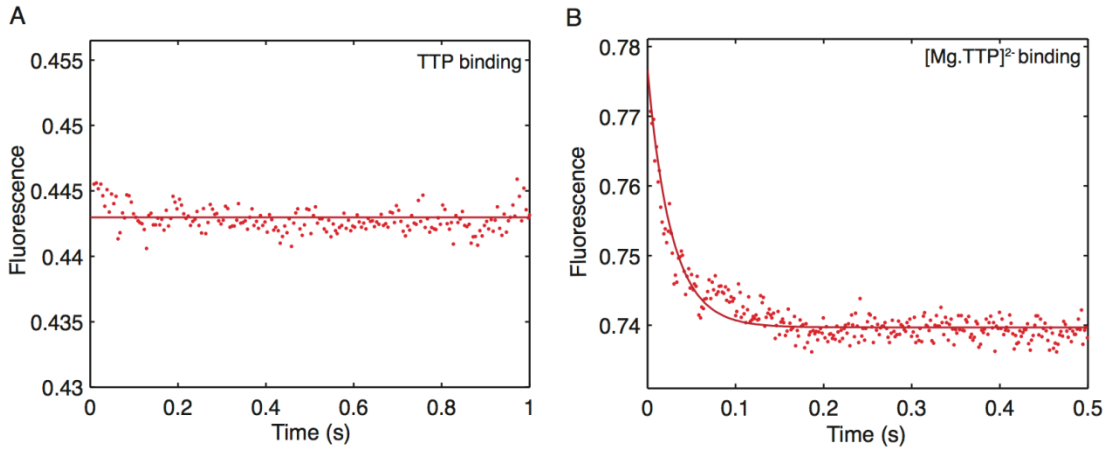

Figure 4.3 $[Mg.TTP]^{2-}$ is required for enzyme closing of HIVRT.

The experiment was performed by rapidly mixing TTP (50 μM) and preformed enzyme-DNA (ED_{dd}) complex (0.1 μM) (A), or rapid mixing $[Mg.TTP]^{2-}$ (50 μM) and preformed enzyme-DNA complex (0.1 μM) (B). The changes of fluorescence upon TTP or $[Mg.TTP]^{2-}$ binding were monitored by stopped flow instrument. Similar results were obtained with 500 μM TTP.

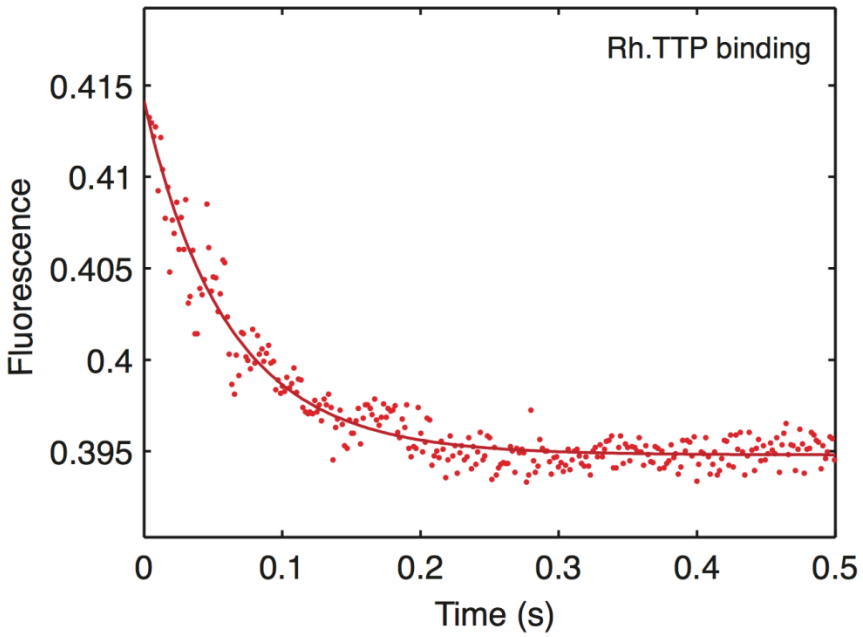

Figure 4.4 $[Rh.TTP]^{2-}$ induces enzyme closing of HIVRT.

The experiment was performed by rapid mixing $[Rh.TTP]^{2-}$ (2 μM) and preformed enzyme-DNA (ED_{dd}) complex (0.1 μM). The change of the fluorescence intensity as a function of time was monitored by stopped flow instrument.

Catalytic Mg^{2+} is not required for the enzyme closing.

We next examined the role of catalytic Mg^{2+} in the conformational change by using double mixing experiment (Figure 4.5). The experiment was performed by first mixing enzyme-DNA complex (100 nM MDCC-labeled HIV-1 wild type RT and 150 nM 25/45nt DNA) with 10 μM $[Mg.TTP]^{2-}$ in the presence of very few free Mg^{2+} (25 μM) for 0.2s (t1), followed by secondary mixing with a large excess of free Mg^{2+} (10 mM) (t2). The fluorescence change upon secondary mixing was monitored by stopped flow assay. Our previous data suggested that the efficiency of nucleotide incorporation ($k_{pol}/K_{d,app}$ for TTP incorporation) is less than 1.5 x 10^{-2} $\mu M^{-1}s^{-1}$ in 80 μM free Mg^{2+} condition (Chapter 5). From the calculation, we know that the $k_{pol}/K_{d,app}$ for TTP incorporation in 25 μM free Mg^{2+} condition would be much less than 1.5 x 10^{-2} $\mu M^{-1}s^{-1}$, and the rate of chemistry at 10 μM $[Mg.TTP]^{2-}$ would be much less than 0.15 s^{-1}, which gives a half life of TTP incorporation much longer than 4.6 s. Therefore, chemistry merely did not occur at the first mixing on 0.2s time scale. On the other hand, because catalytic Mg^{2+} binds to HIVRT very weakly with $K_{d,app}$ of 3.7 mM, it merely did not bind at the first mixing at 25 μM free Mg^{2+} condition. At the secondary mixing of adding a large excess of free Mg^{2+} (10 mM), the catalytic Mg^{2+} binds to HIVRT. In this case, the enzyme would make a decision for going forward to chemistry or continuing on its conformational change. If catalytic Mg^{2+} is not required for the conformational change, we would observe the direct increase of the fluorescence signal upon secondary mixing, indicating that the reopening of the enzyme (the chemistry and pyrophosphate release) occurs immediately after

mixing with catalytic Mg^{2+}. If $[Mg.TTP]^{2-}$ alone is not enough for enzyme closing and catalytic Mg^{2+} is required for assisting the closing of the enzyme, we would observe a first decrease followed by an increase of fluorescence indicating that the enzyme closing is not finished without the assistance of catalytic Mg^{2+}. As a result, we found that the reopening of the enzyme directly occurs after secondary mixing (Figure 4.5). Therefore, our results suggested that the catalytic Mg^{2+} does not contribute the enzyme closing, and $[Mg.TTP]^{2-}$ alone is enough for the enzyme closing of HIVRT.

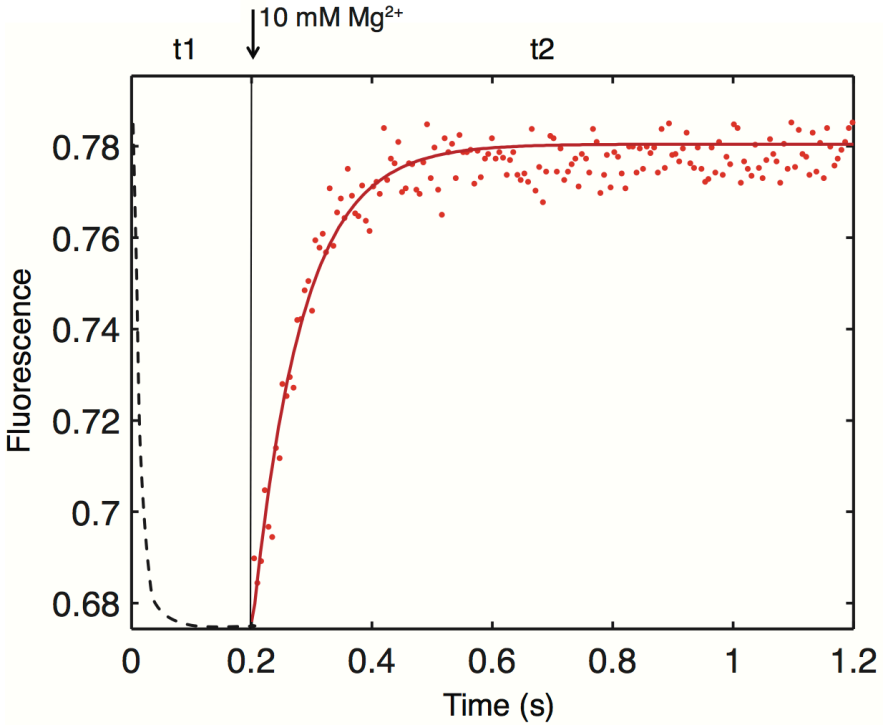

Figure 4.5 Conformational change of HIVRT occurs prior to the binding of the catalytic Mg^{2+}.

Double mixing experiment was performed by pre-mixing ED complex (100 nM) with $[Mg.TTP]^{2-}$ (10 μM) in the presence of 25 μM free Mg^{2+} for 0.2s (t1), followed by secondary mixing with a large excess of free Mg^{2+} (10 mM) (t2). The fluorescence change upon secondary mixing was monitored by stopped flow assay.

Catalytic Mg^{2+} affects the chemistry step of nucleotide incorporation.

To systematically study the effects of Mg^{2+} on each individual step of the nucleotide incorporation, several experiments were preformed to define each kinetic parameter governing the nucleotide incorporation including ground-state binding, conformational change, chemistry, and pyrophosphate release.

First, a stopped flow assay was performed to define the rate of the conformational change. The experiment was performed by rapidly mixing a preformed enzyme-DNA complex (MDCC-labeled HIVRT) with various concentrations of incoming nucleotide. Because natural DNA substrate was used in the stopped flow assay, the change of fluorescence provides useful information to define not only the rate of the conformational change but also the rate of the chemistry when pyrophosphate release is fast. The decrease of fluorescence occurs when the enzyme closes following nucleotide binding while the subsequent increase in fluorescence indicates the reopening of the enzyme after product formation (Figure 4.6A). The rate of the conformational change is too fast to measure directly at 37°. Therefore, to estimate the rate of the forward conformational change at 37°, stopped flow assays were performed as a function of temperature to allow extrapolation to 37°. The enzyme-DNA complex was rapidly mixed with various concentrations of TTP at 5, 10, 18, and 25°. At each concentration the fluorescence time course was biphasic. The concentration dependence of the fast phase of the fluorescence change was fitted to a hyperbolic equation to obtain the maximum rate of the forward conformational change (k_2) at each temperature (Table 4.3). The experiments were then repeated at various concentrations of free Mg^{2+} conditions including 0.25 mM (Figure

4.7A), 1 mM (Figure 4.7C) and 10 mM (Figure 4.7E). Finally, the values of k_2 at 37° at three different free Mg^{2+} conditions were estimated by Arrhenius plot (Figure 4.7B, 4.7D and 4.7F). The results in our study indicate that Mg^{2+} concentrations (from 0.25 mM to 10 mM) do not affect the rate of the forward conformational change (or enzyme closing) (Table 4.4). This result is also consistent with the results from double mixing and $[Rh.TTP]^{2-}$ binding, suggesting that catalytic Mg^{2+} binds after the enzyme closing.

Table 4.3 Temperature Dependence of HIVRT Conformational Change upon TTP Binding at Various Concentrations of Free Mg^{2+}

$[Mg^{2+}]$,mM	k_2 value at 5°, (s^{-1})	k_2 value at 10°, (s^{-1})	k_2 value at 18°, (s^{-1})	k_2 value at 25°, (s^{-1})
0.25	104 ± 10	157 ± 7	343 ± 34	707 ± 69
1	110 ± 12	163 ± 14	388 ± 56	702 ± 27
10	150 ± 6	225 ± 13	461 ± 17	805 ± 68

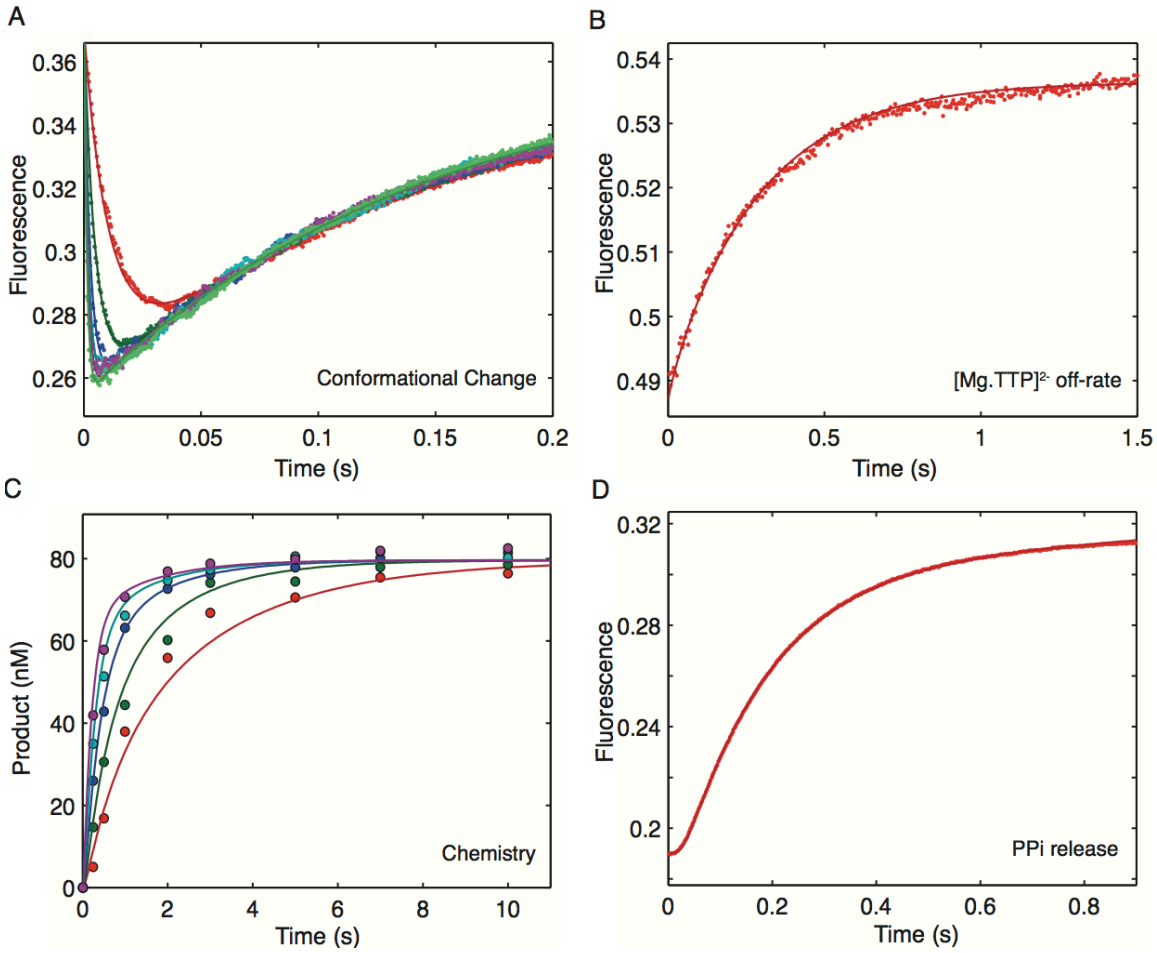

Figure 4.6 Correct nucleotide incorporation in the presence of 1 mM Mg^{2+}.

The time dependence of the fluorescence change upon TTP incorporation was monitored by stopped flow assay (A). The experiment was performed by rapidly mixing a preformed ED complex (100 nM) with various concentrations (10, 25, 50, 75, 100, and 150 μM) of TTP. The nucleotide off-rate experiment (B) was performed by rapidly mixing a preformed enzyme-DNA_{dd}-dNTP complex (100 nM ED_{dd} complex, 1 μM nucleotides) with a nucleotide trap consisting of 2 μM unlabeled ED complex. The rapid chemical quench flow experiment (C) was performed by rapidly mixing a preformed ED complex (100 nM) with various concentrations (0.25, 0.5, 1, 2, and 5 μM) of TTP. The rate of pyrophosphate release (D) was measured using a coupled pyrophosphatase/phosphate sensor assay as described in the text. Four experiments were fit simultaneously to rigorously define each kinetic parameter governing nucleotide incorporation as shown in Scheme 4.1.

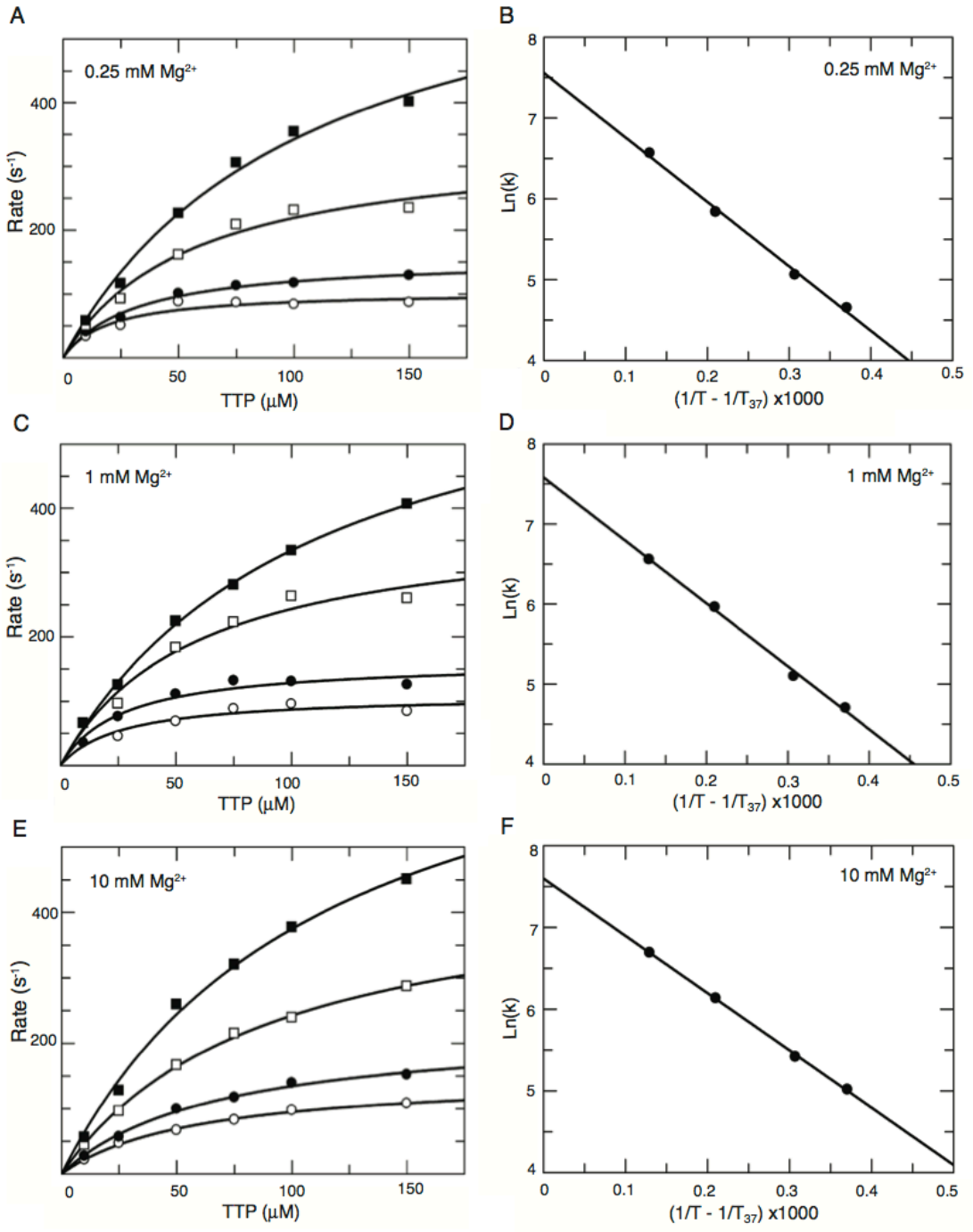
A
0.25 mM Mg2+
Rate (s-1)
TTP (µM)
B
0.25 mM Mg2+
Ln(k)
(1/T - 1/T37) x1000
C
1 mM Mg2+
Rate (s-1)
TTP (µM)
D
1 mM Mg2+
Ln(k)
(1/T - 1/T37) x1000
E
10 mM Mg2+
Rate (s-1)
TTP (µM)
F
10 mM Mg2+
Ln(k)
(1/T - 1/T37) x1000

(Figure 4.7)

Figure 4.7 Mg^{2+} does not affect the rate of forward conformational change.

Temperature dependence of HIVRT conformational change upon TTP incorporation were measured by stopped flow at 0.25 mM (A and B), 1 mM (C and D) and 10 mM (E and F) free Mg^{2+} condition. (A) An ED complex (50 nM) was rapidly mixed with various concentrations of TTP (10, 25, 50, 75, 100 and 150 μM) at 5° (○), 10° (●), 18° (□), 25° (■). The concentration dependences of the fluorescence decrease upon nucleotide binding was fit to a hyperbolic equation to obtain the maximum rate of the conformational change (k_2) at each temperature. The temperature dependence of k_2 was analyzed by Arrhenius plot to estimate the maximum rate of the conformational change at 37° for each free Mg^{2+} condition.

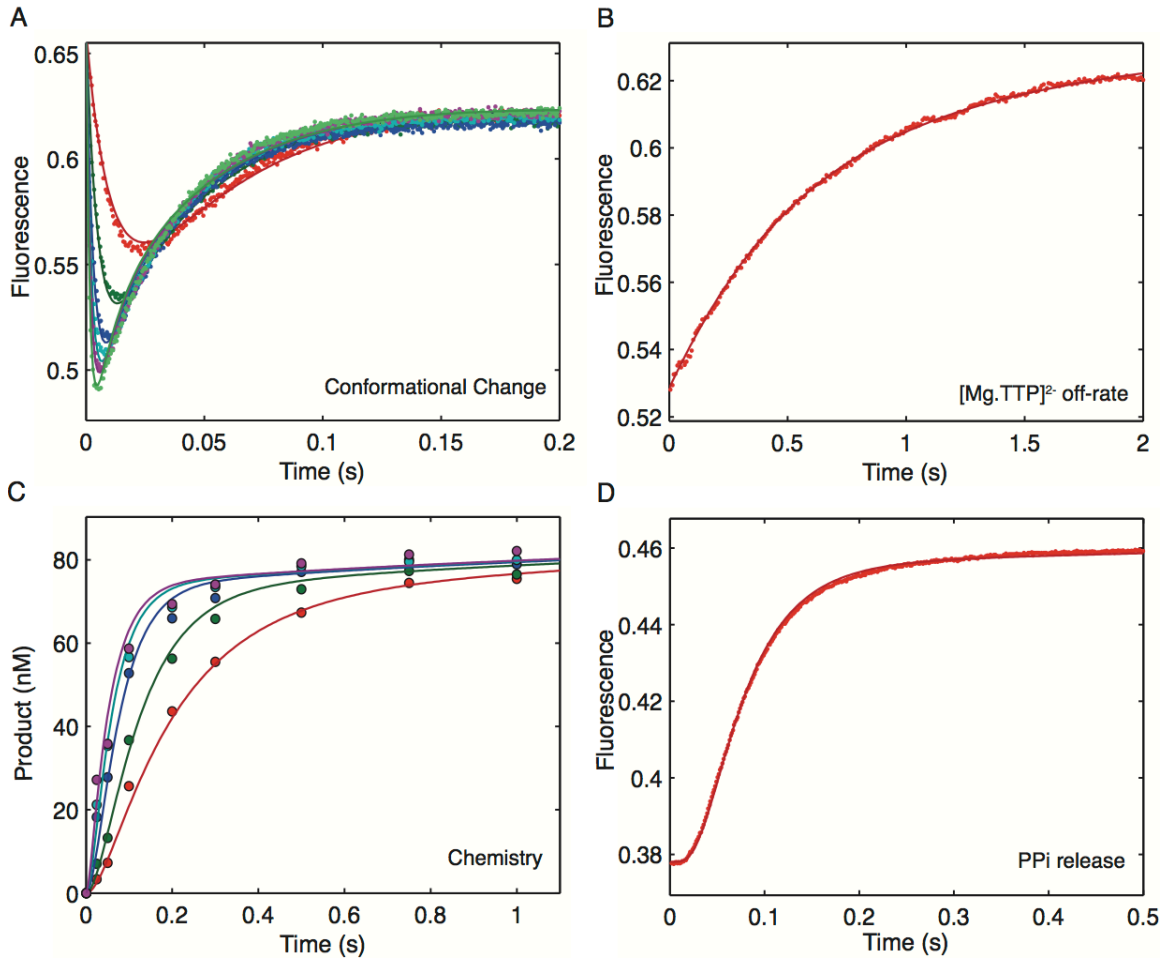

Figure 4.8 Correct nucleotide incorporation in the presence of 10 mM Mg^{2+}.

The time dependence of the fluorescence change upon TTP incorporation was monitored by stopped flow assay (A). The experiment was performed by rapidly mixing preformed ED complex (100 nM) with various concentrations (10, 25, 50, 75, 100, and 150 μM) of TTP. The nucleotide off-rate experiment (B) was performed by rapidly mixing preformed enzyme-DNA_{dd}-dNTP complex (100 nM ED_{dd} complex, 1 μM nucleotides) with a nucleotide trap consisting of 2 μM unlabeled ED complex. The rapid chemical quench flow experiment (C) was performed by rapidly mixing preformed ED complex (100 nM) with various concentrations (1, 2, 5, 10 and 20 μM) of TTP. The rate of pyrophosphate release (D) was measured by a coupled pyrophosphatase/phosphate sensor assay as described in the text. Four experiments were fit simultaneously to rigorously define each kinetic parameter governing nucleotide incorporation as shown in Scheme 4.1.

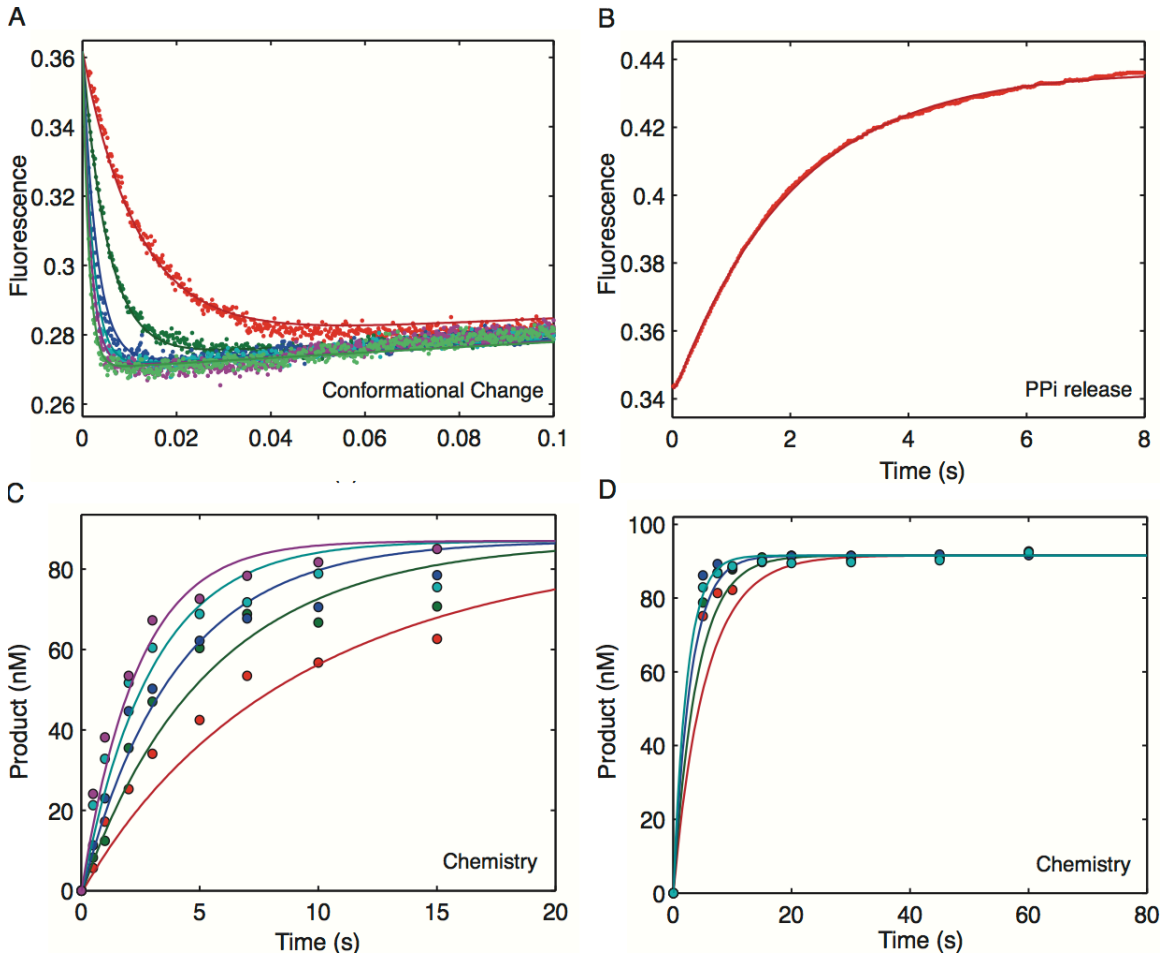

Figure 4.9 Correct nucleotide incorporation in the presence of 0.25 mM Mg^{2+}.

The time dependence of the fluorescence change upon TTP incorporation was monitored by stopped flow assay (A). The experiment was performed by rapidly mixing preformed ED complex (100 nM) with various concentrations (10, 25, 50, 75, 100, and 150 μM) of TTP. The rate of pyrophosphate release (B) was measured by a coupled pyrophosphatase/phosphate sensor assay as described in the text. The rapid chemical quench flow experiment (C) was performed by rapidly mixing preformed ED complex (100 nM) with various concentrations (0.25, 0.5, 1, 2, and 5 μM) of TTP. The chemical quench experiment was repeated at longer time scale (D). Four experiments were fit simultaneously to rigorously define each kinetic parameter governing nucleotide incorporation as shown in Scheme 4.1.

Table 4.4 Kinetic Constants for TTP Incorporation at Low and High Concentrations of Free Magnesium Ion

$[Mg^{2+}]$, mM	$1/K_1$ (μM)	k_2 (s^{-1})	k_{-2} (s^{-1})	K_2	k_3 (s^{-1})	k_4 (s^{-1})
10	275 ± 3	2000 ± 67	3.9 ± 0.1	513 ± 22	21 ± 0.1	> 102
1	213 ± 3	1960 ± 173	9.4 ± 0.2	209 ± 19	6 ± 0.1	> 159
0.25	216 ± 2	1910 ± 178	9.7± 0.2	197 ± 19	0.6 ± 0.01	> 20.3

To better define the rate of the chemistry, quench flow kinetic assay was then performed. An enzyme-DNA complex (^{32}P-labeled primer) was rapidly mixed with varying concentrations of incoming nucleotide and the rate of product formation as a function of nucleotide concentration was used to define the maximum polymerization rate (k_{cat}) of the reaction and the apparent binding affinity ($K_{d,app}$) of incoming nucleotide.

To estimate the rate of the reverse of the conformational change, a nucleotide off-rate experiment were performed by rapidly mixing a preformed enzyme-DNA_{dd}-dNTP complex (100 nM MDCC-labeled HIVRT, 150 nM 25ddA/45-nt, 1 μM nucleotides) with a nucleotide trap consisting of 2 μM unlabeled enzyme-DNA complex. Because DNA primer is dideoxy-terminated, premixing ED_{dd} complex with incoming nucleotide only allows the binding but not the chemistry. After the addition of the large excess of the nucleotide trap (unlabeled enzyme-DNA complex) was added, the rate of

the fluorescence change defines the rate for the reverse of the conformational change which limits the rate of release of the nucleotide. Because these data were fit based upon computer simulation, it was not necessary to perform this experiment at multiple concentrations of the nucleotide trap.

To study the rate of pyrophosphate release, a coupled pyrophosphatase/phosphate sensor assay was performed as described previously (128, 129). The experiment was conducted by pre-mixing the ED complex with the MDCC-labeled pyrophosphate binding protein (MDCC-PBP), pyrophosphatase (PPase), and *phosphate mop* containing purine nucleoside phosphorylase (PNPase) and 7-methylated guanosine (7-MEG). After mixing with TTP, the incoming nucleotide was incorporated into the primer and the released pyrophosphate was quickly degraded to phosphates by PPase which were then captured by MDCC-PBP. The presence of *phosphate mop* helps to reduce the background contamination. Because there is a large fluorescent change upon phosphate binding to MDCC-PBP and the kinetics of phosphate binding to PBP is much faster than that of the pyrophosphate release from HIVRT (149), the time course of the fluorescent change could be used to define the rate of pyrophosphate release (129). According to our simulation, the rate of pyrophosphate release could be accurately defined even if the rate of pyrophosphate release were only 5-fold faster than the rate of the chemistry. However, because the rate of the pyrophosphate release in our experiment was much faster (> 5-fold of the rate of the chemistry) (Table 4.3), only a range (lower limit) of the rate could be defined. That is, in these experiments, the kinetics of phosphate release tracked exactly with the chemical reaction, implying that pyrophosphate release followed chemistry but

was much faster. In fitting the data by simulation, the minimum rate of pyrophosphate release is defined by the value sufficient to make the two processes appear to be coincident.

Finally, four experiments were fit simultaneously to rigorously define each kinetic parameter governing nucleotide incorporation as shown in Scheme 4.1. Similar experiments and analyses were also repeated at various Mg^{2+} conditions (0.25 mM, 1 mM and 10 mM free Mg^{2+} conditions) to investigate the effects of free Mg^{2+} on each individual step of nucleotide incorporation (Figure 4.6, Figure 4.8 and Figure 4.9). The results in our study showed that Mg^{2+} concentrations (from 0.25 mM to 10 mM) do not affect the ground state binding (K_1) and the rate of the conformational change (or enzyme closing) (k_2), but does affect the rate of the chemistry (k_3) and the reverse of the conformational change (or enzyme reopening) (k_{-2}). Although it seems that Mg^{2+} concentrations affect the rate of pyrophosphate release, our simulation only gives a lower limit at this time and therefore no direct conclusion was possible.

Catalytic Mg^{2+} also affects the reverse of the conformational change.

The rate of the reverse of the conformational change (Figure 4.10A) was monitored by stopped flow assay as mentioned above. The rates of nucleotide off-rate (k_{-2}) as a function of Mg^{2+} concentrations were fit to a hyperbola equation (Figure 4.10B), with a $K_{d,app}$ of 3.7 mM. The Mg^{2+} dependent nucleotide off-rates indicated that the binding of the second Mg^{2+} actually stabilizes the ternary complex of enzyme-DNA-Mg^{2+}-dNTP by decreasing the k_{-2} value. The calculated value of $K_{d,app}$ for the second

Mg^{2+} in the Mg^{2+} dependent nucleotide off-rate experiments (Figure 4.10) is the same as that of $K_{d,app}$ for catalytic Mg^{2+} in the Mg^{2+} dependent catalysis experiment (Figure 4.2), suggesting that binding of the catalytic Mg^{2+} stabilizes the closed complex.

The value of k_{-2} at 0.25 mM Mg^{2+} was also measured using a different method due to the low efficiency of the nucleotide trap at low Mg^{2+} concentration (Figure 4.11). We used a combination of two enzymes (unlabeled HIVRT-DNA and apyrase) to trap and digest free nucleotides in solution. The k_{-2} value obtained by this method was 9.9 ± 0.4 s^{-1}. In addition, $[Mg.TTP]^{2-}$ concentration dependent kinetics of binding was measured by stopped flow to define the on-rate and an equilibrium titration assay was performed to define the net dissociation constant (K_d) of $[Mg.TTP]^{2-}$ binding. By global fitting two experiments simultaneously to the model shown in scheme 4.3 with fixed k_2 value (obtained from temperature dependent stopped flow assay), the k_{-2} value of $[Mg.TTP]^{2-}$ finally was defined as 9.7 ± 0.2 s^{-1}. The calculated value is consistent with the estimation of the k_{-2} value from the Mg^{2+} dependent $[Mg.TTP]^{2-}$ off-rate experiment shown in figure 4.10B, which is around 10 s^{-1} at 0.25 mM free Mg^{2+}. Therefore, the results in our study support the conclusion that catalytic Mg^{2+} stabilizes the binding of $[Mg.TTP]^{2-}$ after the enzyme closing. It is the first time that the interplay between two Mg^{2+} ions has been identified by using biochemical experiments, which supports the coordination found in crystal structures.

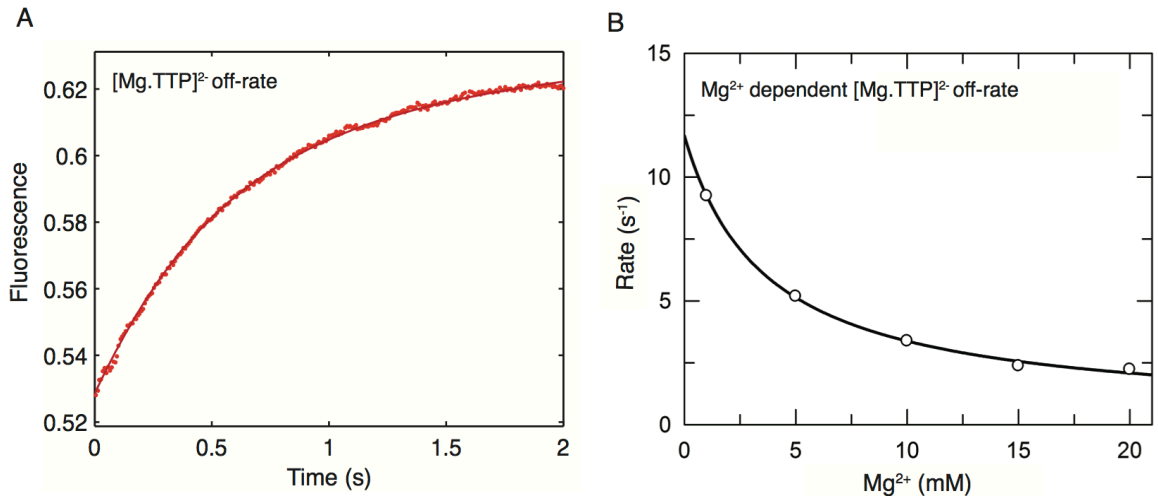

Figure 4.10 Mg^{2+} affects the rate of the reverse of conformational change.

The rate of the reverse of the conformational change (A) was monitored by stopped flow assay mentioned in the text. The rates of nucleotide dissociation rate were plotted as a function of Mg^{2+} concentration (B) to define the $K_{d,app}$ of Mg^{2+} in reducing the rate of the reverse of conformational change.

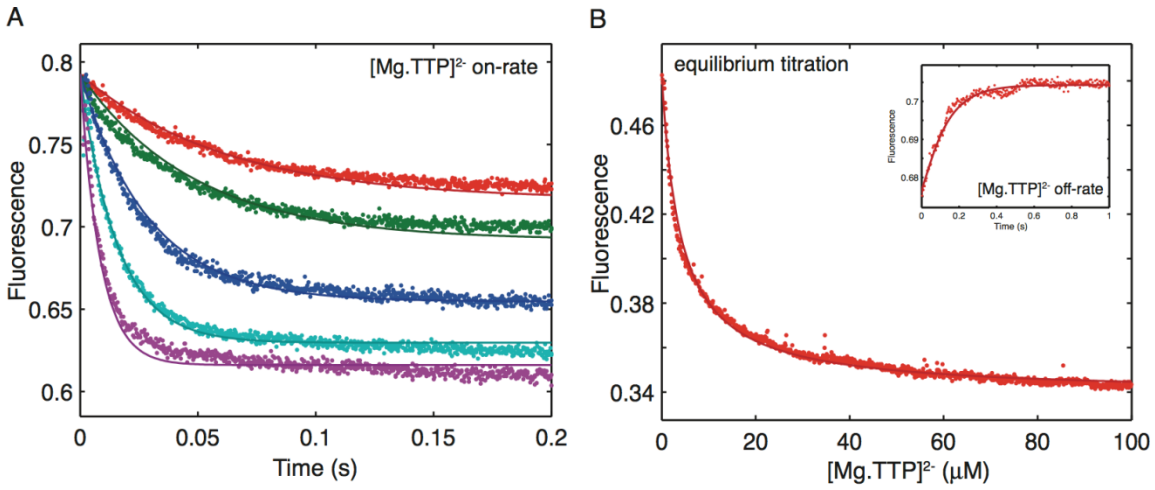

Figure 4.11 Measurement of the rate of nucleotide dissociation at 0.25 mM Mg^{2+}.

Binding of $[Mg.TTP]^{2-}$ (on-rate) was measured by stopped flow assay (A). The experiments were performed by rapidly mixing various concentrations (3, 5, 10, 25 and 50 μM) of $[Mg.TTP]^{2}$ with a preformed enzyme-DNA complex in the presence of 0.25 mM free Mg^{2+}. Binding of $[Mg.TTP]^{2-}$ to HIVRT was also measured by equilibrium titration assay (B). The experiment was performed by titrating the preformed enzyme-DNA complex with varying concentrations of $[Mg.TTP]^{2-}$ ranging from 0 to 100 μM. Global fitting of two experiments simultaneously to the model shown in scheme 4.3 to accurately define the rate of the nucleotide dissociation (k_{-2}) at 0.25 mM free Mg^{2+}. The rate of nucleotide dissociation at 0.25 mM free Mg^{2+} (inset of B) was measured by rapidly mixing preformed enzyme-DNA_{dd}-dNTP complex (100 nM ED_{dd} complex, 1 μM nucleotides) with a nucleotide trap consisting of 3 μM unlabeled ED complex and 5 units of apyrase.

Mg^{2+} concentration affects on nucleotide specificity.

Nucleotide specificity (k_{cat}/K_m) is the most important kinetic parameters for defining the efficiency of substrate binding and incorporation. It is best understood as the second-order rate constant for substrate binding times the probability that once bound, the substrate goes forward to finish the production formation. Our results showed that the value of the specificity constant is decreased by 12-fold as the free Mg^{2+} concentration is changed from 10 to 0.25 mM, showing that the efficiency of nucleotide incorporation is Mg^{2+} dependent. In addition, the results in our study suggested that nucleotide specificity is re-defined as the free Mg^{2+} concentration is altered. Because the release of pyrophosphate is a fast step, k_{cat}/K_m is defined by the steps leading up to pyrophosphate release. Moreover, because the rate of the conformational change (k_2) is much faster than chemistry (k_3), the specificity constant depends on the kinetic partitioning governed by the relative values of k_{-2} versus k_{-3} (126). If $k_{-2} >> k_3$, the ground state binding and conformational change come to equilibrium and the specificity constant is governed by the product of binding equilibria and the rate of chemistry ($k_{cat}/K_m = K_1K_2k_3$). If $k_{-2} << k_3$, the nucleotide binding fails to comes to equilibrium and the rate of chemistry does not contribute to the specificity constant ($k_{cat}/K_m = K_1k_2$). With the normal nucleotide (TTP) incorporation at 0.25 mM Mg^{2+}, the value of k_{-2} ($9.7 \pm 0.2\ s^{-1}$) is much greater than that of k_3 ($0.6 \pm 0.01\ s^{-1}$), suggesting that the k_{cat}/K_m value is governed by the product of binding and the rate of chemistry ($k_{cat}/K_m = K_1K_2k_3$). As the free Mg^{2+} concentration was increased to 10 mM, the value of k_{-2} ($3.9 \pm 0.1\ s^{-1}$) is much smaller than that of k_3 ($21 \pm 0.1\ s^{-1}$) and therefore k_{cat}/K_m is only governed only by the nucleotide binding ($k_{cat}/K_m = K_1k_2$). Clearly, nucleotide specificity is a function of the free Mg^{2+} concentration.

To better investigate the effects of free Mg^{2+} on nucleotide specificity, free energy profiles of nucleotide incorporation at three different free Mg^{2+} concentrations (0.25 mM, 1 mM, and 10 mM) were plotted (Figure 4.12). The k_{cat}/K_m value is determined by the energy barrier between its highest peak relative to its unbound state. At 0.25 mM free Mg^{2+}, the highest peak is the state between FD_nN and $FD_{n+1}PPi$ (or chemistry step). Therefore, nucleotide specificity is determined by all of the steps from its unbound state to the chemistry ($k_{cat}/K_m = K_1K_2k_3$). At 10 mM free Mg^{2+}, the highest peak is the state between ED_nN and FD_nN (or conformational change step). Thus, nucleotide specificity is determined by only two steps including ground state binding and the conformational change ($k_{cat}/K_m = K_1k_2$). At 1 mM free Mg^{2+}, the highest peak is not obvious and therefore a simplified equation for defining nucleotide specificity does not work in this case. To accurately define the nucleotide specificity, a complete equation containing each parameter has to be used (Equation 4.4). Again, the free energy profiles showed that nucleotide specificity is re-defined as the free Mg^{2+} concentration is altered from 0.25 mM to 10 mM. Because the $K_{d,app}$ of catalytic Mg^{2+} is 3.7 mM, it also suggests that catalytic Mg^{2+} re-defines the nucleotide specificity as it binds to the enzyme.

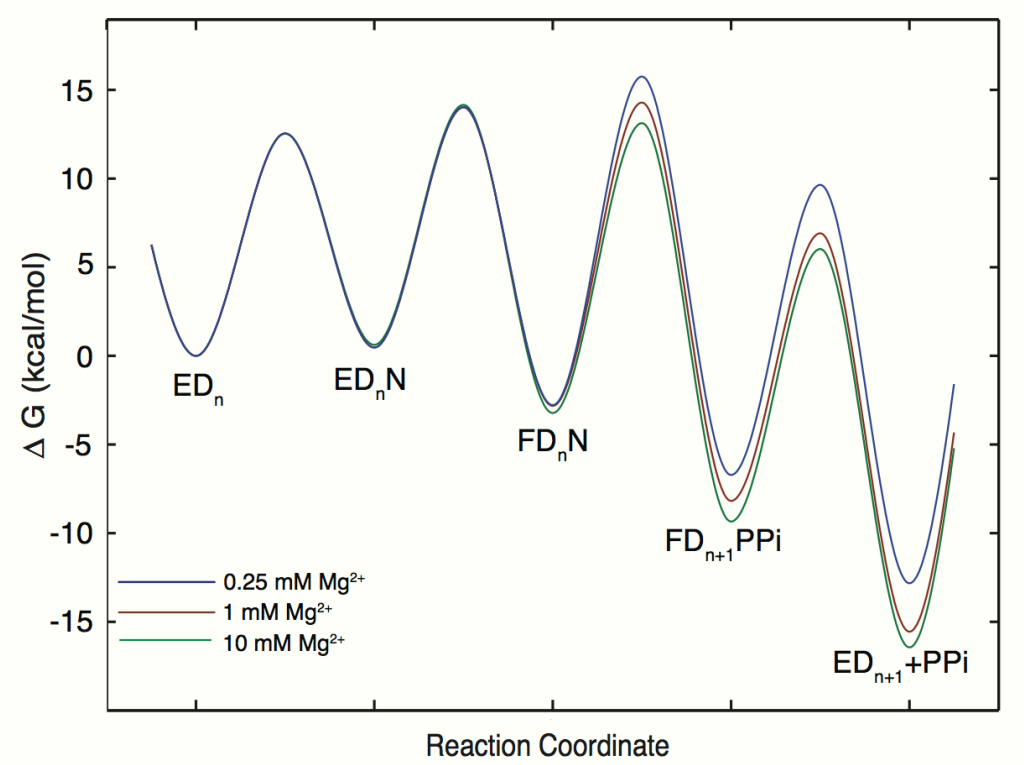

Figure 4.12 Mg^{2+} affects the specificity constant governing nucleotide incorporation.

The free-energy diagrams for TTP incorporation at 0.25, 1, and 10 mM free Mg^{2+} condition were shown in blue, brown and green colors. The free energy was calculated as $\Delta G = RT[\ln(kT/h)-\ln(k_{obs})]$ kcal/mol using rate constants derived from global fitting, where the constant k is the Boltzmann constant, T is 310 K, h is Planck's constant, and k_{obs} is the first-order rate constant. The nucleotide concentration was set equal to 100 μM to calculate k_{obs} for nucleotide binding.

Equation 4.4:

$$k_{cat} = \frac{k_2 k_3}{k_2 + k_{-2} + k_3}$$

$$K_m = \frac{k_2 k_3 + k_{-1}(k_{-2} + k_3)}{k_1(k_2 + k_{-2} + k_3)}$$

$$k_{cat} / K_m = \frac{k_1 k_2 k_3}{k_2 k_3 + k_{-1}(k_{-2} + k_3)}$$

4.4 DISCUSSION

It has been more than 22 years since the general two-metal-ion mechanism was proposed. Although the metal ions could be directly observed in many crystal structures, biochemical experiments are still required to establish the kinetic and thermodynamic basis for the roles of the two metal ions in specificity. Especially, what is the difference between the two metal ions? Do they bind to the enzyme with the same affinity? Do they bind sequentially or simultaneously? The $[Mg.dNTP]^{2-}$ complex is stable thermodynamically (K_d is around 28 μM) but the metal ions exchange rapidly, complicating analysis of the roles of the two metal ions.

One approach toward dissecting the role of the two metal ions is based on the use of the exchange-inert $[Rh.dNTP]^{2-}$ complex that can be purified and then mixed with enzyme to examine the kinetics of the conformational change in the absence of Mg^{2+} (150, 151). Here we repeat these observations, confirming the conclusion that the $[Me.dNTP]^{2-}$ complex induces a change in structure of the enzyme from the open to the

closed state before the second metal ion binds. However, the amplitude of the observed conformational change is lower with $[Rh.dNTP]^{2-}$ than we observed with $[Mg.dNTP]^{2-}$ (Table 4.13). Our analysis supports the conclusions derived using $[Rh.dNTP]^{2-}$, but also support concerns about the use of $[Rh.dNTP]^{2-}$ because the reactions are different from those seen with $[Mg.dNTP]^{2-}$. Actually, different $[Me.dNTP]^{2-}$ complex has different binding kinetics. For example, the binding of $[Ca.dNTP]^{2-}$ or $[Mn.dNTP]^{2-}$ is much slower than that of $[Mg.dNTP]^{2-}$ (Figure 4.13). Therefore, experiments using physiological relevant $[Mg.dNTP]^{2-}$ are needed for studying the two-metal-ion mechanism. By accurate calculation of the concentrations of free Mg^{2+} and free $[Mg.dNTP]^{2-}$ we show that it is not necessary to purify $[Mg.dNTP]^{2-}$ to resolve the roles of the two Mg^{2+}. The much weaker binding of the catalytic metal ion affords resolution of the roles of the two metal ions using the natural Mg^{2+} by titrations of activity versus free $[Mg^{2+}]$ where all concentrations were above those needed to saturate the $[Mg.dNTP]^{2-}$ complex. Here, we show kinetically that the $[Mg.dNTP]^{2-}$ complex binds to induce the conformational change to the closed state and that the catalytic Mg^{2+} binds after the conformational change. Because Mg^{2+} ion is the natural substrate for catalysis in many enzymes, the studies performed here also provided more physiological relevant information about the role of each Mg^{2+} ion *in vivo*.

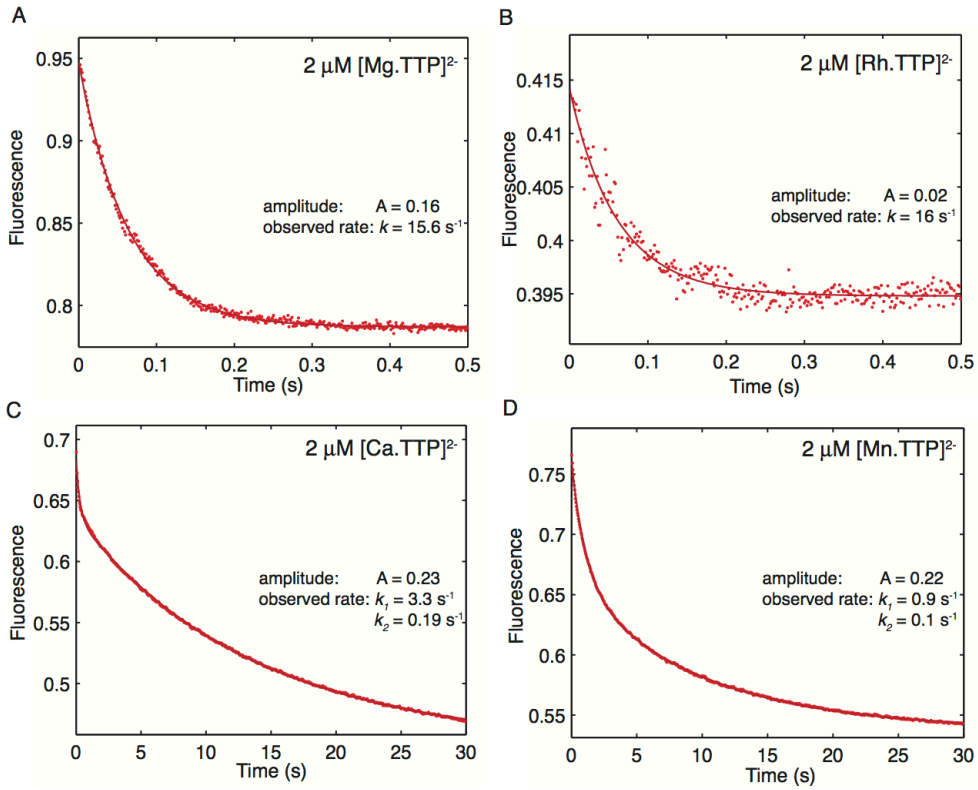

Figure 4.13 Comparison of $[Me.dNTP]^{2-}$ Complex Binding to HIVRT.

The experiments were performed by rapid mixing $[Me.TTP]^{2-}$ (2 μM) and preformed enzyme-DNA (ED_{dd}) complex (0.1 μM). Except for exchange-inert $[Rh.TTP]^{2-}$ complex (B), experiments of $[Mg.TTP]^{2-}$(A), $[Ca.TTP]^{2-}$(C), and $[Mn.TTP]^{2-}$ (D) binding were performed in the presence of 10 mM free Mg^{2+}, Ca^{2+} and Mn^{2+}, respectively. The change of the fluorescence intensity as a function of time was monitored by stopped flow instrument.

The binding of the second Mg^{2+} is required for catalysis as shown directly by our measurements, supporting proposals first put forth in the two-metal ion mechanism (105). In addition, the second Mg^{2+} also stabilizes the closed state by reducing the rate at which the enzyme opens to release the dNTP. However, it is important to note that the relatively low affinity of the second Mg^{2+} relative to the physiological concentration may provide an important contribution toward fidelity; for example, a higher Mg^{2+} binding affinity would otherwise stabilize the binding of a mismatched nucleotide and facilitate mis-incorporation. We are led to a model in which fidelity is largely determined by nucleotide binding and the conformational change to align the substrate at the active site, following by weak and presumably brief binding of the Mg^{2+} to stimulate catalysis.

The results in our study showed that $[Mg.TTP]^{2-}$ binds to HIVRT very tightly (K_d = 0.5 μM), and catalytic Mg^{2+} binds to HIVR very weakly ($K_{d,app}$ is 3.7 mM). The huge difference (more than 5000-fold) of binding affinity between two metal ions is very surprising, and has never been reported before. Our results resolved the controversy that there was only one metal ion found in the active site (59), but in theory their reactions are catalyzed by the two-metal-ion mechanism(152). Because the second metal ion binds so weakly, it just could not be observed at a limited concentration of Mg^{2+}.

In addition, our results also suggested that two metal ions bind sequentially, with the nucleotide bound Mg^{2+} binding first followed by the catalytic Mg^{2+} binding. This conclusion is supported by several experiments. The temperature dependent stopped flow experiment was repeated with three free Mg^{2+} concentrations (0.25 mM, 1 mM and 10 mM) and no obvious effect of free Mg^{2+} on the rate of forward conformational change

(k_2) was observed. In addition, the global fitting of four experiments also showed that free Mg^{2+} concentration has no effect on both the ground state binding (K_1) and the conformational change (k_2), demonstrating that catalytic Mg^{2+} binds after the enzyme closes. To further test this hypothesis, double mixing experiment was also performed. $[Mg.TTP]^{2-}$ was first mixed with the enzyme-DNA complex in the presence of very low free Mg^{2+} to allow the enzyme closing (t1). After a large excess of free Mg^{2+} was added at the second mixing (t2), the chemistry directly occurred. These results demonstrate that the catalytic Mg^{2+} is not required for the nucleotide-induced forward conformational change, but is required for catalysis. The results from all three experiments are also consistent with the result from $[Rh.TTP]^{2-}$ binding experiment, suggesting that nucleotide bound Mg^{2+} is sufficient for inducing the enzyme closing. Therefore, the results in our studies suggested that the enzyme closing is caused by nucleotide bound Mg^{2+}, and catalytic Mg^{2+} binds after the enzyme closes.

Our conclusion that two Mg^{2+} bind with different affinities and in sequential order to the active site of HIV-RT during the catalytic cycle is supported by available structural data. High-resolution x-ray crystal structures of HIV-RT have been obtained at various stages of the reaction with enzyme in complex with nucleotide analogue inhibitors (Table 4.5). These structures show that HIV-RT can bind to up to four functionally relevant Mg^{2+} ions, two at the HIV-RT polymerase domain and two at the RNase H domain (59, 153). The interests of this study are the two Mg^{2+} in the polymerase active site exhibit significantly different affinities.

In light of our kinetic result, we analyze the published structures with the focus on the coordination and interaction around Mg^{2+} ions. This analysis was performed in collaboration with Jessie Zhang. Upon binding to proteins, metal ions seek to satisfy the preferred coordination geometry of a given metal for minimized energy. Magnesium, for example, prefers an octahedral coordination and will be most tightly bound when this geometry is satisfied (Figure 4.14A). Mg^{2+} ions at the polymerase domain of HIV-RT are coordinated through polar interactions with the side chains of aspartates 110 and 185 and the triphosphate moiety of the nucleotide substrate (Figures 14B & 14C). In Mg1, the carboxylate side chain of Asp110 and 185 as well as two oxygens from the phosphate groups of the nucleotide form the four coordination on the plane with a distance around 2.2-2.4 Å. Another phosphate oxygen and the carbonyl group of valine 111 are the apex from the opposite sides with a distance close to 2.6 Å. Therefore, Mg1 displays classic octahedral coordination geometry (Figure 14B) which is most optimal thermodynamically. On the other hand, Mg2, deviates from the standard octahedral coordination with four coordination by the side chains of Asp110 and Asp185 but not forming a plane. The two apex coordinations sites are occupied by nucleotide on one end but empty on the other (Figure 14C), which is possibly occupied by a solvent water molecule that is too flexible to be seen in the structure. The analysis of the metal coordination indicates that the two magnesium ions are bound differentially.

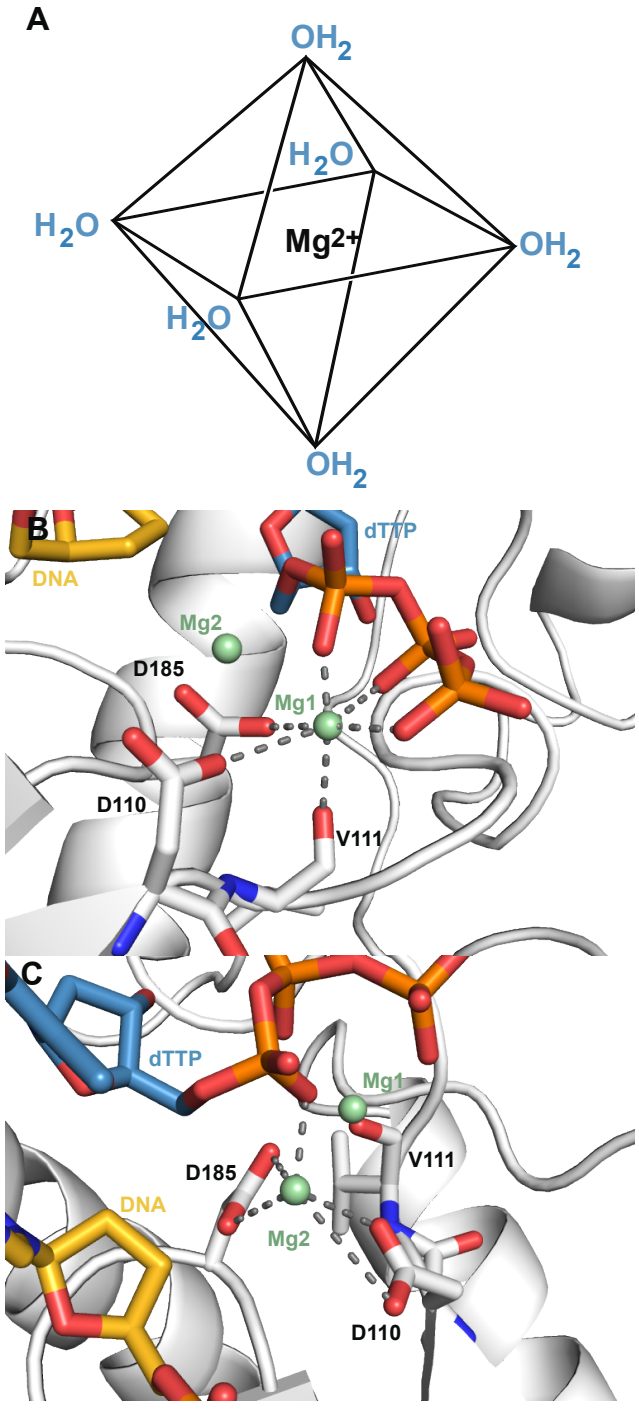

Figure 4.14 HIV-RT magnesium coordination geometry.

A) Octahedral coordination geometry is ideal for magnesium ions. Magnesium preferentially forms six evenly spaced polar interactions, demonstrated here as interactions with solvent waters. B) Mg1 (pale green) at the HIV-RT polymerase domain exhibits ideal coordination geometry by forming three polar contacts with active site residues aspartate 110, 185 and valine 111(white), and three polar contacts with the triphosphate group of substrate dTTP (steel blue) (PDB ID 1RTD). C) Mg2 (pale green) at the HIV-RT polymerase domain exhibits atypical coordination geometry and forms four polar contacts with the side chains of aspartate 110 and 185 (white) and one polar contact to the triphosphate group of substrate dTTP (steel blue) (PDB ID 1RTD). (Performed by Zhang Lab)

Table 4.5 HIVRT Crystal Structures

Structure Components	Bound Ligand	PDB ID	Mg1 B-Factor ($Å^2$)	Mg2 B-Factor ($Å^2$)	$[Mg^{2+}]$ in crystal drop
HIV-RT, DNA:DNA	NA	3KJV	NA	NA	2.5 mM
HIV-RT, RNA:DNA	dATP	4PQU	30.69	35.75	10 mM
HIV-RT, DNA:DNA	dATP	3KK2	5.08	NA	2.5 mM
HIV-RT, DNA:DNA	AZTTP	3V4I	87.31	NA	10 mM
HIV-RT, DNA:DNA	TFV	1T05	16.24	NA	10 mM
HIV-RT, DNA:DNA	GS-9148 -diphosphate	3KK1	15.85	NA	2.5 mM

To understand the relative mobility of the ions, we scrutinize on the temperature factors of the ions. Temperature factor (or thermal factor, B factor) is defined as a measure for an atom to deviate from a certain position. A high B factor correlates to high movement and low occupancy. Therefore, within the same molecule model, B factor can be used to show the relative mobility of the atoms. When we inspect the structures of

HIV-RT when both Mg^{2+} ions are present, the B factors indicate that the mobility of the ions varies. For the structure PDB IDs 4PQU in which Mg^{2+} ion concentration (10 mM), Mg1 exhibits a comparable B factor with Mg2 (30.69 vs. 35.75 Å2 in 4PQU). In other crystallization conditions in which HIV-RT is complexed with DNA:DNA template:primer, and nucleotide analog complexes either under low concentrations of Mg^{2+} or low resolution diffraction, only one Mg^{2+} can be modeled in the density which is consistently Mg1 (Table 4.5). This structural data is in line with the in solution determination of K_d for these two Mg^{2+} in our study. Mg1, the well-coordinated and low B-factor magnesium, likely corresponds to the observed nucleotide bound ion with a K_d of 0.5 μM. Indeed, the binding of magnesium ion neutralizes the negative charges of Asp110 and 185 and allows the effective recognition of nucleotide. Mg2, which is poorly coordinated and displays a high relative B-factor or even missing in structure, likely corresponds to catalytic ion with a K_d of 3.7mM. Mg2 is positioned proximal to elongating DNA primer and is better positioned to play a catalytic role. In addition, no Mg^{2+} was found in the structure PDB IDs 3KJV in which Mg^{2+} ion concentration is 10 mM and HIV-RT is complexed with DNA:DNA template:primer only, suggesting that binding of nucleotide bound Mg^{2+} in the active site is prerequisite for the binding of catalytic Mg^{2+}. Therefore, it supports the results from our kinetic experiments that two metal ion binds sequentially, with the nucleotide bound Mg^{2+} binding first followed by the catalytic Mg^{2+} binding.

The kinetic and structural data agree that the binding of Mg1 (nucleotide bound Mg^{2+}) and Mg2 (catalytic Mg^{2+}) can be partitioned as sequential processes and supports

the following model. First, Mg1 (nucleotide bound Mg^{2+}) binds and helps position nucleotide substrate by forming electrostatic interactions with the negatively charged triphosphate group (Figure 15A to 15B). These interactions fully satisfy magnesium's preferred octahedral coordination geometry and result in a tightly bound magnesium atom, reflected in its low relative B-factor and experimentally observed K_d. The tightly bound Mg1 coordinates the triphosphate of nucleotide substrates and positions an additional polar interaction for Mg2 (catalytic Mg^{2+}) binding. Once Mg1 is in place, Mg2 is recruited and forms non-octahedral polar contacts with active site residues and the positioned triphosphate (Figure 15C). Mg2 (catalytic Mg^{2+}) binds weakly with non-preferred coordination geometry, as reflected in its high relative B-factor and experimentally observed K_d. Once both Mg1 and Mg2 are bound chemistry occurs, both magnesium are released, and the cycle is reinitiated.

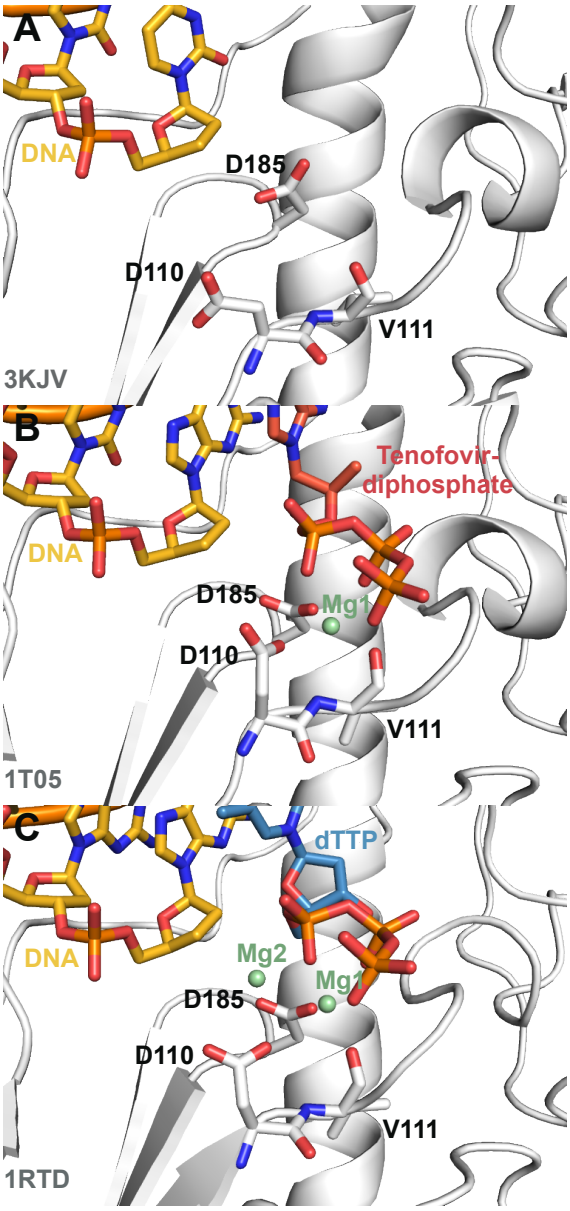

Figure 4.15 Snapshots of HIV-RT magnesium binding.

A) HIV-RT (white) and DNA:DNA template:primer (goldenrod) complex binds no magnesium in the absence of nucleotide substrate (PDB ID 3KJV). B) HIV-RT (white), DNA:DNA template:primer (goldenrod), and tenofovir-diphosphate nucleotide analogue inhibitor (tomato) non-productive complex structure binds only one magnesium ion (Mg1, pale green) (PDB ID 1T05) and represents the initial magnesium bound state. C) HIV-RT (white), DNA:DNA template:primer (goldenrod), and dTTP (steel blue) complex binds two magnesium ions. Mg1 (pale green) is well coordinated and appears to play a structural role to position the triphosphate group of dTTP. Mg2 is poorly coordinated with atypical coordination geometry. This orientation represents the hypothesized stage of the reaction cycle preceding chemistry in which two magnesium ions are bound. (Performed by Zhang Lab)

In addition, the effects of two Mg^{2+} ions on each individual step of the nucleotide incorporation were also investigated. As shown above, the results from $[Mg.TTP]^{2-}$ and $[Rh.TTP]^{2-}$ binding experiments suggested that nucleotide bound Mg^{2+} is required for the enzyme closing (Figure 4.3). Because $[Mg.TTP]^{2-}$ concentration dependent chemistry was observed in the presence of 10 mM free Mg^{2+}, the result from chemical quench suggested that nucleotide bound Mg^{2+} is also required for the chemistry step (Figure 4.6C). Because the rate of pyrophosphate release is much faster than the rate of the chemistry in our experiments, only a lower limit of the rate could be defined (Table 4.3). In future, measurement of the rate of pyrophosphate release using chemical quench assay will be performed to better define the effects of $[Mg.TTP]^{2-}$ and free Mg^{2+} on the pyrophosphate release step.

The results in our study suggested that catalytic Mg^{2+} binds after the enzyme closing. It does not affect the steps of ground state binding and conformational change, but affect the reopening of the enzyme and the rate of the chemistry. Based on its function, we proposed the sequential binding model as shown in the scheme 4.4. In this model, nucleotide bound Mg^{2+} first binds to the enzyme and induces the conformational change, and then catalytic Mg^{2+} binds to the active site after the enzyme closing. Binding of catalytic Mg^{2+} then stabilizes the closed tertiary complex and facilitates the chemistry. It is known that k_{-2} versus k_3 is a critical kinetic partitioning in defining nucleotide specificity (k_{cat}/K_m). Our results suggested that nucleotide specificity is re-defined as the free Mg^{2+} concentration is changed from 10 to 0.25 mM. Therefore, it also suggests that binding of catalytic Mg^{2+} ($K_{d,app}$ of 3.7 mM) re-defines the nucleotide specificity. In DNA polymerases, high specificity is achieved partially by proper positioning and alignment of two metal ions with stringent coordination requirement (154), which could not be achieved without the binding of catalytic Mg^{2+}. Therefore, the nucleotide specificity of an

enzyme may be achieved by several steps. First, the enzyme undergoes a conformational change from the open state to the closed state to allow the nucleotide binding. At this stage, different nucleotides induce different conformational change of the enzyme and therefore display different binding affinities. The discrimination of the correct nucleotide from the mismatches comes from the base-pairing between the incoming nucleotide and the DNA template. As a result, correct nucleotide displays a tight binding (small k_{-2} value) and mismatched displays a loose binding (a very high k_{-2} value) (130). In the second step, catalytic Mg^{2+} binds after the enzyme closing. The binding of catalytic Mg^{2+} stabilizes the closed complex by forming coordination with nucleotide bound Mg^{2+} and the transition state for the chemistry. Because catalytic Mg^{2+} affects the kinetic partitioning between going forward for the chemistry and going backward for the reopening of the enzyme. The binding of the catalytic Mg^{2+} actually re-defines the nucleotide specificity.

Scheme 4.4 Proposed model for the sequential binding of two metal ions

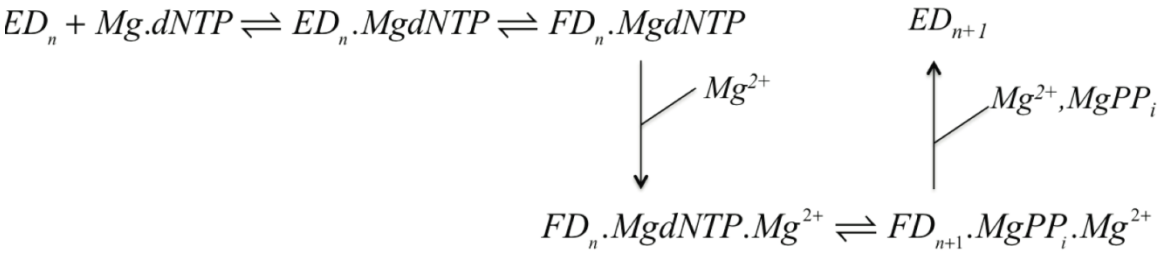

Recently, it has been reported that the third Mg^{2+} is transiently bound during nucleotide incorporation, and the existence of the third Mg^{2+} was proposed to affect pyrophosphate release (111). It is also shown that the third Mg^{2+} only exist in the correct but not in the mismatched nucleotide incorporation, and the transient existence of the third Mg^{2+} is critical for the pyrophosphorolysis reaction (112). Although the rates of the pyrophosphate release were not accurately defined in our experiments, they are all very fast in the correct nucleotide incorporation at the free Mg^{2+} concentrations ranging from 0.25 mM to 10 mM. Our previous studies on the mismatched incorporation using RNA/DNA duplex suggested the rate of pyrophosphate release is very slow (~0.03 s^{-1}) (An Li and Johnson, unpublished). Further studies on the mismatched incorporation using DNA/DNA duplex will also be performed to directly compare the rate of pyrophosphate release between correct nucleotide incorporation and mismatched incorporation. If the rate of the pyrophosphate release is indeed very slow in mismatched nucleotide incorporation, it would suggest that nucleotide bound Mg^{2+} itself is not sufficient for facilitating the pyrophosphate release, and the proper alignment in the active site or probably the third Mg^{2+} is required for the pyrophosphate release. To further investigate the third Mg^{2+}, molecular dynamic simulation will also be performed to directly observe the dynamic movement of the Mg^{2+} ions in the active site of HIVRT. In addition, the Mg^{2+} dependent pyrophosphorolysis was also performed using both correct and mismatched terminated primers to investigate the effect of the possible third Mg^{2+} on pyrophosphorolysis reaction. The results showed that no obvious product of pyrophosphorolysis was observed with mismatched terminated primer in the time scale of 4 hours (Gong and Johnson, unpublished), which suggested that pyrophosphorolysis is very unfavorable in the mismatched terminated primer. Therefore, the results in our study

seem to support the previous report that the transient existence of the Mg^{2+} ion is critical for the pyrophosphorolysis reaction.

Finally, nucleotide specificity (k_{cat}/K_m) at different Mg^{2+} concentration was investigated. Our results suggested that nucleotide incorporation in HIVRT is highly Mg^{2+} dependent. The k_{cat}/K_m value for TTP incorporation is changed approximately 12-fold as the free Mg^{2+} concentration is changed from 10 mM to 0.25 mM (Table 4.6). It is known that the physiological Mg^{2+} concentration varies in different cell types (155, 156). For example, it is reported that the physiological concentration of free Mg^{2+} in human T lymphocytes is around 0.25 mM (109, 157), but around 0.6 mM in mammalian muscle cell (158). Therefore, the Mg^{2+} dependent nucleotide incorporation found in our experiment may be one of the mechanisms that the host used to regulate the activities of some enzymes. On the other hand, because virus has its preference for the host cell types, it may also be one of the sensors that the virus used to find its favorite host cells or perhaps perturb the intracellular Mg^{2+} concentration to optimize viral replication.

Table 4.6 Kinetic Constants for TTP Incorporation at Low and High Concentrations of Free Magnesium Ion

$[Mg^{2+}]$, mM	$K_{d,net}$ (μM)	K_m (μM)	k_{cat} (s^{-1})	k_{cat}/K_m ($\mu M^{-1}s^{-1}$)	Fold
10	0.5 ± 0.02	3.6 ± 0.1	20.7 ± 1	6 ± 0.3	12
1	1.0 ± 0.09	1.7 ± 0.2	6 ± 0.7	3.5 ± 0.6	7
0.25	1.1± 0.1	1.2 ± 0.1	0.6 ± 0.08	0.5 ± 0.08	1

In conclusion, we have investigated the role of each Mg^{2+} ion in the two-metal-ion mechanism by studying their binding affinities, binding mode (sequential binding or simultaneous binding), and the effects of their binding on each individual steps of the nucleotide incorporation. The studies we have performed here provided insight and detailed information about the general two-metal-ions mechanism. Finally, we found that Mg^{2+} concentration also affects the nucleotide specificity.

Chapter 5: The Effects of Mg^{2+} on Nucleotide Fidelity and Processivity of HIVRT

5.1 INTRODUCTION

DNA polymerases play vital roles in many biological processes as they catalyze nucleotide incorporation by adding incoming nucleotides according to the template sequence. Fidelity and processivity are the two important properties of a DNA polymerase (107). Fidelity is the ability of enzymes to discriminate correct nucleotides from the pool of mismatched nucleotides. A high fidelity is achieved by the combination of many factors including base pairing geometry, enzyme conformational changes, exonucleolytic proofreading, strand-misalignment, and the effects of accessory proteins (159). Processivity is the ability of enzymes to perform continuous polymerization without dissociation from the DNA template. The value of processivity is quantified by the number of the nucleotides incorporated into the growing DNA primer during a single DNA binding event. It is reported that enzymes containing multi-subunit complexes such as sliding clamp usually has high processivity because the sliding clamp holds the DNA template and prevents its dissociation (160, 161). Enzymes without auxiliary clamp structures have a broad spectrum of processivity ranging from a few to thousands of nucleotides (160, 162).

DNA polymerases are divided to seven families: A, B, C, D, X, Y and RT (including HIV reverse transcriptase, HIVRT) (58). Like other RTs, the structure of HIVRT is analogous to a right-hand containing fingers, thumb and palm subdomains,

which provide the active site for polymerization. In addition, HIVRT also contains two other subdomains: connection subdomain and ribonuclease H (RNase H) subdomain (58, 60). The connection subdomain of HIVRT connects the polymerase domain and RNase H domain. It is reported that the connection subdomain also facilitates the *in vivo* annealing of host tRNA to the viral genomic RNA (163). The RNase H subdomain is known for its ribonuclease activity, which degrades the RNA template and removes the RNA primer after its single-stranded RNA has been replicated to form an RNA/DNA duplex (60).

It is reported that the structure of HIVRT affects both fidelity and processivity (107, 123, 153, 159, 164). For example, the conformational change of the fingers domain upon nucleotide binding is critical for selecting the correct nucleotide (123, 159). Residues in the thumb domain affect both the fidelity and processivity of HIVRT by interacting with the primer strand and the minor groove of the duplex (107, 164), and the RNase H domain affects the DNA binding (153). Key residues that interact with the incoming nucleotide also affect the fidelity of HIVRT. For example, K65R and K65A mutations alter the fidelity by affecting both mismatched nucleotide incorporation and mismatched base-pair extension efficiencies (165).

Both the polymerase domain and the RNase H domain of HIVRT prefer the Magnesium ions (Mg^{2+}) for its catalysis (58, 60, 153). It is reported that two Mg^{2+} are separated by ~ 3.6 angstrom in the polymerase active site of HIVRT (58, 166). The role of the first Mg^{2+} (catalytic Mg^{2+}) is to lower the pKa of 3'-terminal OH of the DNA primer, bring it close to the incoming nucleotide, and generate an oxyanion that attacks the α phosphate group of the incoming nucleotide (167). The role of second Mg^{2+}

(nucleotide bound Mg^{2+}) is to stabilize the transition state by neutralizing the negative charge on the α-phosphate (105). Recently, it was reported that the value of HIVRT fidelity is higher at the low free Mg^{2+} concentrations *in vivo* compared to most experiments performed *in vitro* (108). Because most of the *in vitro* studies were performed at Mg^{2+} concentrations ranging from 5 to 10 mM (108) and the physiological Mg^{2+} concentration in human lymphocytes was reported as low as 0.25 mM (108-110), whether the concentration of Mg^{2+} affects fidelity requires more rigorous study.

In this chapter, we investigated the effects of Mg^{2+} on both correct and mismatched nucleotide incorporation, from which we characterized the effects of Mg^{2+} on fidelity. In addition, we studied the effects of Mg^{2+} on DNA binding and dissociation, and on processivity. We also investigated the possible relationship among fidelity, processivity and Mg^{2+} ions.

5.2 METHODS

Expression and Purification of HIVRT

HIVRT protein was expressed, purified and labeled as previous described (123). Briefly, the p51 and p66 subunits of HIVRT were separately expressed. The cell pellets were combined to yield a 1:1 ratio, lysed, and sonicated. Then, the protein was purified by tandem Q-Sepharose and Bio-Rex70 columns followed by single-stranded DNA (ssDNA) affinity column, and labeled by MDCC (7–DIETHYLAMINO–3- ((((2-MALEIMIDYL) ETHYL) AMINO) CARBONYL) COUMARIN) fluorophore. The

unreacted MDCC was then removed by Bio-Rex70 column. The concentration of purified HIVRT was measured by 'Coomassie Plus' protein assay and an active site titration experiment.

DNA Substrates for Kinetic Studies

The 25/45nt DNA substrates (Table 5.1) were purchased from Integrated DNA Technologies. The DNA substrates were annealed by first heating at 95° for 5 min and followed by gradually cooling to room temperature. For DNA substrates used in quench flow assay, the DNA primer (25nt) was labeled at the 5' with γ-^{32}P ATP (PerkinElmer) using T4 polynucleotide kinase (NEB).

Table 5.1 DNA substrates for kinetic studies

25/45nt	
25nt:	5′-GCCTCGCAGCCGTCCAACCAACTCA-3′
45nt:	5′-CGGAGCGTCGGCAGGTTGGTTGAGT**A**GCAGCTAGGTTACGGCAGG-3′

Correct Nucleotide Incorporation

The time dependence of correct nucleotide incorporation was monitored by quench flow assay. The experiment was performed by rapidly mixing a preformed enzyme-DNA complex (0.1 μM) with various concentrations of incoming nucleotide (from 0.25 μM to 20 μM). All concentrations are those during the reaction after the 1:1 mixing. The experiments were repeated at various concentrations of free Mg^{2+}. Each reaction was quenched by the addition of 0.5 M EDTA at varying time points. Products were separated by running 15% PAGE (acrylamide (1:19 bisacrylamide), 7M Urea), and quantified by ImageQuant 6.0 software (Molecular® Dynamics). The product formation upon TTP incorporation was fitted to the model shown in scheme 5.1 using *KinTek Explorer* software (KinTek Corp. Austin, TX). The specificity constant of correct nucleotide incorporation was calculated by $k_{cat}/K_m = k_{pol}/K_{d,app}$.

Scheme 5.1 Simplified model for dNTP incorporation

$$ED_n + dNTP \underset{}{\overset{K_{d,app}}{\rightleftharpoons}} ED_n dNTP \overset{k_{pol}}{\rightleftharpoons} ED_{n+1} + PPi$$

Mismatched Nucleotide Incorporation

The time dependence of mismatched nucleotide incorporation was monitored by hand mixing methods. The experiments were performed by mixing an enzyme-DNA complex (0.1 μM) with various concentrations (from 0.5 mM to 8 mM) of mismatched

nucleotides (dA: dC, dA:dG, and dA:dA). The reactions were quenched by the addition of 0.5 M EDTA at varying time points. The experiments were repeated at various concentrations of free Mg^{2+} condition. Product formation was quantified and analyzed similarly as mentioned above in the correct nucleotide incorporation.

DNA binding measurement

The kinetics of DNA binding to HIVRT was measured using stopped flow fluorescence assays. The experiment was performed by rapidly mixing 0.1 μM enzyme (MDCC-labeled HIVRT) with various concentrations of DNA (ranging from 0.05 μM to 0.2 μM). The time dependence of the fluorescence change upon DNA binding was monitored using an AutoSF-120 stopped-flow instrument (KinTek Corp., Austin, TX) by exciting the fluorophore at 425 nm and monitoring the fluorescence change at 475 nm using a single band-pass filter with a 25 nm bandwidth (Semrock).

DNA off-rate measurement

The rate of DNA dissociation was also measured by stopped flow. The experiment was performed by premixing enzyme DNA complex (MDCC-labeled HIVRT) (0.1 μM) for 10 min, followed by mixing with large amount of heparin trap. The time dependent fluorescence change upon DNA dissociation was monitored using a stopped-flow instrument (KinTek Corp. Austin, TX).

Global Fitting of DNA binding and dissociation

The results from DNA binding and dissociation were globally fitted to the model shown in scheme 5.2 by *KinTek Explorer* software (KinTek Corp. Austin, TX). FitSpace confidence contours analysis was also performed for standard error estimation.

Scheme 5.2 DNA binding Model

In the absence of Mg^{2+}

$$E + D \underset{160s^{-1}}{\overset{341\mu M^{-1}s^{-1}}{\rightleftharpoons}} ED \underset{3.3s^{-1}}{\overset{41s^{-1}}{\rightleftharpoons}} FD$$

In the presence of 10 mM Mg^{2+}

$$E + D \underset{73s^{-1}}{\overset{383\mu M^{-1}s^{-1}}{\rightleftharpoons}} ED \underset{0.2s^{-1}}{\overset{48s^{-1}}{\rightleftharpoons}} FD$$

Calculation of Processivity

The processivity of HIVRT was first calculated using the equation of $k_{pol}/k_{off,DNA}$, and then directly observed by Mg^{2+} dependent experiment. The experiments were performed by mixing ED complex with 500 μM dNTP in the presence or absence of heparin trap (2 mg/ml), and the reactions were quenched at either 10s or 3 min. The observed processivity of HIVRT was calculated using equation 5.1.

Equation 5.1 Calculation of Processivity

$$\text{Processivity} = \frac{\sum(\text{relative intensity} \times \text{no.nucletides})}{\sum(\text{relative intensity})}$$

Free Mg^{2+} Concentration Calculation

Free Mg^{2+} concentration calculation was performed as previous described (Chapter 4). Briefly, 0.5 mM EDTA was added to the solution to provide a Mg-EDTA buffer. The concentrations of free Mg^{2+} and $[Mg.dNTP]^{2-}$ were specified, and the total concentrations of Mg^{2+} and dNTP in solution were calculated using the equation 5.2. Because this simplified equation relies on some simplifying approximations, the reactions with all equilibria were also simulated using *KinTek Explorer* software to calculate the free Mg^{2+} concentration in solution based upon given total concentrations of each species and the pH.

Equation 5.2 Free Mg^{2+} concentration calculation

$$[Mg]_0 = [Mg] + [Mg.dNTP] + \frac{[EDTA]_0}{1 + K_2 / [Mg]}$$

$$[dNTP]_0 = [Mg.dNTP] \cdot (1 + (K_1 / [Mg]) \cdot (1 + [H] / K_3))$$

Derivation of Equation 5.3

In the equilibrium:

$$ED + Mg \underset{}{\overset{K_d}{\rightleftharpoons}} ED.Mg$$

$$E_0 = ED + ED.Mg \qquad K_d = \frac{[ED][Mg]}{[ED.Mg]}$$

Therefore,

$$[ED] = \frac{K_d \cdot [ED.Mg]}{[Mg]}$$

For the linked equilibrium (simplified from Figure 5.4):

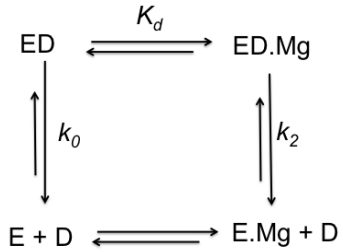

$$k_{obs} = \frac{k_0 \cdot [ED] + k_2 \cdot [ED.Mg]}{[ED] + [ED.Mg]}$$

$$k_{obs} = k_0 \cdot \frac{ED}{E_0} + k_2 \cdot \frac{ED.Mg}{E_0}$$

$$k_{obs} = \frac{k_0[ED.Mg]K_d / [Mg] + k_2[ED.Mg]}{[ED.Mg]K_d / [Mg] + [ED.Mg]}$$

$$k_{obs} = \frac{k_0 + k_2[Mg] / K_d}{1 + [Mg] / K_d}$$

$$k_{obs} = \frac{k_0 K_d / [Mg] + k_2}{K_d / [Mg] + 1}$$

Where k_0 represents the maximal rate (k_{max}) of DNA dissociation, and k_2 represents the minimum rate (k_{min}) of DNA dissociation. Therefore,

$$k_{obs} = \frac{k_{\max} + k_{\min}[Mg] / K_d}{1 + [Mg] / K_d}$$

5.3 RESULTS

The effects of Mg^{2+} on fidelity of HIVRT

To study the effects of Mg^{2+} on fidelity of HIVRT, correct nucleotide incorporation was first investigated at various concentrations of free Mg^{2+} conditions (80 μM, 0.25 mM and 10 mM Mg^{2+}). An enzyme-DNA complex was mixed with various concentrations of incoming nucleotide (TTP) using rapid quench experiment. Products were then separated and quantified relative to the substrate DNA. Fitting the dNTP concentration dependence of the rate of single nucleotide incorporation afforded the maximal rate of polymerization (k_{pol}) and apparent binding affinity ($K_{d,app}$) governing TTP binding and incorporation according to the simplified model shown in Scheme 5.1. Rather than fitting each curve to a single exponential and then plotting rate versus concentration, the primary data were fit globally using *KinTek Explorer* software (Figure 5.1A and 5.1C). Even though nucleotide binding proceeds occurs in two-steps, analysis of the single turnover kinetics provides an accurate estimate for k_{cat}/K_m for sequential nucleotide incorporation events during processive synthesis (123). The simple model shown in Scheme 5.1 is adequate because steps after the chemistry (pyrophosphate release and translocation) are fast (123, 126, 148), and the measurement of k_{pol} and $K_{d,app}$ values provide an estimate for the specificity constant ($k_{cat}/K_m = k_{pol}/K_{d,app}$). The results showed that $k_{pol}/K_{d,app}$ values governing correct nucleotide incorporation are highly Mg^{2+} dependent. The efficiency of correct nucleotide incorporation increases more than 200-fold as the free Mg^{2+} concentration increases from 80 μM ($k_{pol}/K_{d,app}$ = 2.9 x 10^{-2} $\mu M^{-1}s^{-1}$) to 10 mM ($k_{pol}/K_{d,app}$ = 6.1 $\mu M^{-1}s^{-1}$). A similar trend could also be observed in the k_{pol} values as well. The k_{pol} value is increased by

about 120-fold as free Mg^{2+} concentration is changed from 80 μM to 10 mM. The results in our study indicates that the binding of catalytic Mg^{2+} significantly increases the efficiency of nucleotide incorporation.

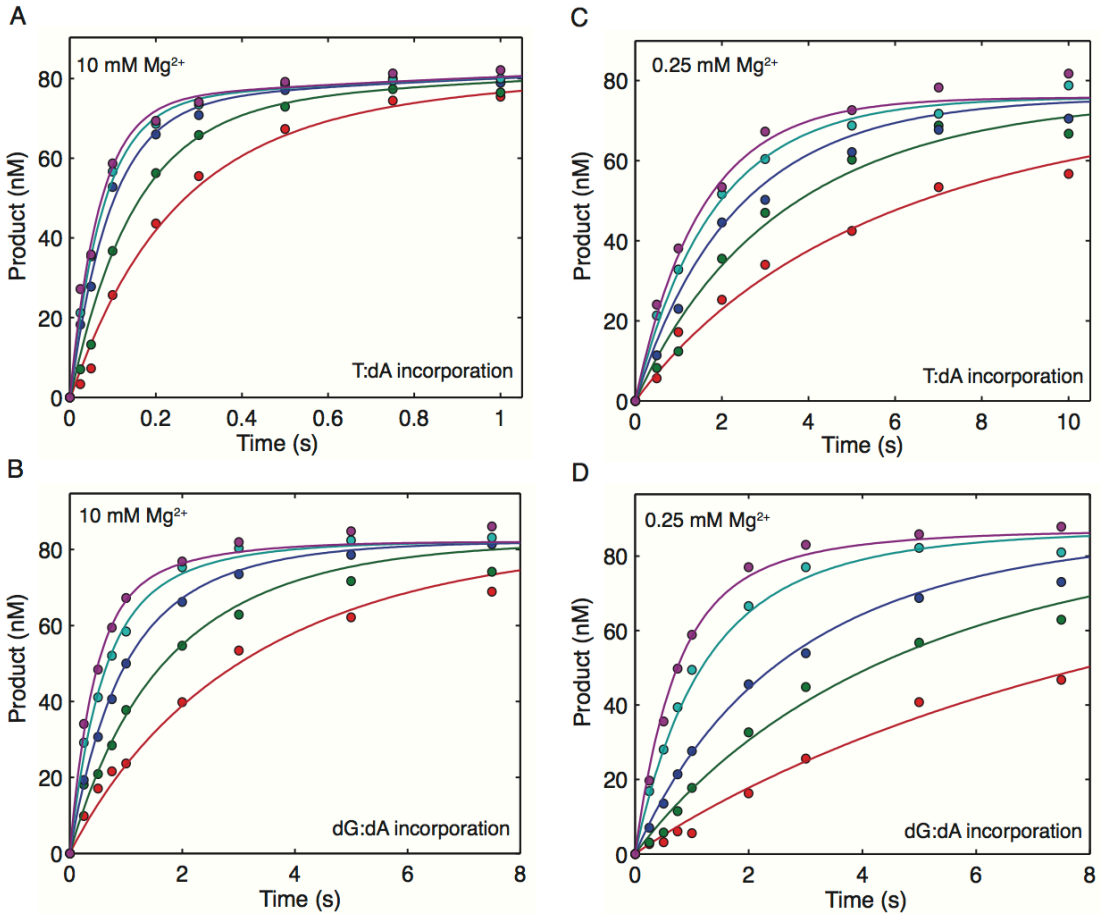

(Figure 5.1)

Figure 5.1 Correct or mismatched incorporation in the presence of 10 mM or 0.25 mM free Mg^{2+} condition.

Correct nucleotide incorporation experiments were performed by rapid mixing ED complex (0.1 μM) with various concentrations of TTP (1, 2, 5, 10, 20 μM) in 10 mM free Mg^{2+}(A), or rapid mixing ED complex (0.1 μM) with various concentrations of TTP (0.25, 0.5, 1, 2, 5 μM) in 0.25 mM free Mg^{2+}(C). Mismatched nucleotide incorporation experiments were performed by rapid mixing ED complex (0.1 μM) with various concentrations of mismatched nucleotides (500, 1000, 2000, 4000, 8000 μM) at either 10 mM free Mg^{2+} (B) or 0.25 mM free Mg^{2+} (D).

To investigate the effect of mismatched nucleotide incorporation, similar experiments were performed as shown for correct incorporation (Figure 5.1B and 5.1D). Because mismatched nucleotides bind to HIVRT with apparent K_d of millimolar range (Table 5.2), much higher concentrations (500, 1000, 2000, 4000 and 8000 μM) of nucleotides were used. The experiments were repeated at various concentrations of free Mg^{2+} as well (25 μM, 0.25 mM and 10 mM). The results showed that as free Mg^{2+} is increased from 25 μM to 10 mM, the $k_{pol}/K_{d,app}$ values of mismatched nucleotides incorporation is increased by 34-, 46- and 25-fold for dC:dA, dG:dA and dA:dA mismatched pairs, respectively (Table 5.2). Therefore, the result indicated that mismatched nucleotide incorporations are also Mg^{2+} dependent. Note that because high concentrations of free nucleotide (>4 mM) showed inhibitory effects due to free dNTP at 25 μM free Mg^{2+}, reliable kinetics could not be obtained at saturating concentrations nucleotide. In this case, neither k_{pol} values nor $K_{d,app}$ values could be accurately defined. Only the $k_{pol}/K_{d,app}$ values for mismatch incorporation could be defined. A good example could be seen in mismatched dATP incorporation at 25 μM free Mg^{2+} (Table 1). The obtained apparent K_d (12.6 mM) has a very broad range of lower and upper bound (6.1 mM - 133 mM). The observed inhibitory effect appear to be due to the binding competition between $[Mg.dNTP]^{2-}$ and high concentrations of free nucleotides (> 4 mM) under conditions designed to maintain a low free Mg^{2+} concentration comparable to the K_d for forming the $[Mg.dNTP]^2$ complex.

Table 5.2 Discrimination and Fidelity of HIV Reverse Transcriptase at Low and High Concentrations of Free Magnesium Ion

Base pairs	$[Mg^{2+}]$ mM	k_{pol} (s^{-1})	$K_{d,app}$ (μM)	$k_{pol}/K_{d,app}$ ($\mu M^{-1}s^{-1}$)	D	Fidelity
	0.080	0.14 (0.13 - 0.16)	4.8 (4.2 - 5.7)	2.9×10^{-2}	1	1
T:dA	0.25	0.9 (0.8 - 1)	0.6 (0.5 - 0.9)	1.5	1	1
	10	16.7 (15 - 18.5)	2.8 (2.3 - 3.3)	6	1	1
	0.025	0.2 (0.16 - 0.34)	5200 (4000 - 9400)	3.8×10^{-5}	< 763	$> 1.3 \times 10^{-3}$
dC:dA	0.25	1.5 (1 - 2.9)	10800 (6500 - 22000)	1.4×10^{-4}	10714	9.3×10^{-5}
	10	5.7 (4.9 - 7.1)	4400 (3600 - 5900)	1.3×10^{-3}	4615	2.2×10^{-4}
	0.025	0.16 (0.03 - 0.23)	7900 (700 - 12400)	2×10^{-5}	< 1450	$> 6.9 \times 10^{-4}$
dG:dA	0.25	3.5 (2.3 - 7.1)	9500 (6000 - 19700)	3.7×10^{-4}	4054	2.5×10^{-4}
	10	3.4 (3.1 - 4)	3700 (3100 - 4600)	9.2×10^{-4}	6522	1.5×10^{-4}
	0.025	0.4 (0.2 - 4.1)	12600 (6100 - 133000)	3.2×10^{-5}	< 906	$> 1.1 \times 10^{-3}$
dA:dA	0.25	1.1 (0.8 - 1.9)	3000 (2000 - 5900)	3.7×10^{-4}	4054	2.5×10^{-4}
	10	3.8 (3.1 - 6)	4800 (3700 - 7900)	7.9×10^{-4}	7595	1.3×10^{-4}

Note: Discrimination is indicated as "D", and calculated by using the equation of $(k_{pol}/K_d)_{correct}/(k_{pol}/K_d)_{mismatch.}$ Fidelity= 1/Discrimination; The lower and upper limits for obtained kinetic parameters are shown in parenthesis as (-) respectively.

Finally, discrimination and fidelity at various concentrations of free Mg^{2+} were calculated using the $k_{pol}/K_{d,app}$ values obtained above (Table 5.2). The results showed that there is no significant difference of fidelity between 0.25 mM and 10 mM free Mg^{2+} for two of the three mismatches studied. Because cellular Mg^{2+} concentrations range from 0.25 mM to 2 mM (108-110, 168-170), it also suggests that the fidelity of HIVRT is not significantly different at the cellular Mg^{2+} concentrations compared to standard conditions used *in vitro*. Our result is consistent with a recent finding that HIV mutation rate is comparable in different cell types (171). HIVRT showed higher discrimination against one mismatch, dC:dA, at 0.25 mM free Mg^{2+} (10^{-5}) than others mismatches (10^{-4}). Thus, the fidelity of HIVRT may be slightly affected by Mg^{2+} concentration for some mismatches. Similar results were also observed in our previous report, in which dC:T and T:T mismatched shows higher fidelity (10^{-5}) than dG:T (10^{-4}) (172).

As the free Mg^{2+} concentration is decreased to a very limited level (eg. 25 μM), a significant decrease of fidelity was observed suggesting that Mg^{2+} does affect fidelity of HIVRT if the level of free Mg^{2+} is very low. However, the concentration of free Mg^{2+} is too low to fully saturate the nucleotide in forming the $[Mg.dNTP]^{2-}$ complex. Therefore, the results at the lowest free Mg^{2+} concentration are not reliable.

The effects of Mg^{2+} on DNA binding kinetics and equilibrium

To investigate the effects of Mg^{2+} on DNA binding equilibrium, various concentrations of DNA were rapidly mixed with a fixed concentration of HIVRT. By site specifically labeling HIVRT with an environmentally sensitive fluorophore-MDCC, the

time dependent fluorescence change upon DNA binding was monitored by stopped flow instrument. The experiment was first performed in the absence of Mg^{2+} (Figure 5.2A) and repeated in the presence of 10 mM free Mg^{2+} (Figure 5.2C). The results showed that the increase of fluorescent signal upon DNA binding was biphasic, indicating that the binding of DNA is a two-step binding reaction, as monitored by the MDCC label. Therefore, double exponential equation was used for the data fitting. In addition, the dissociation of DNA from HIVRT was also observed by stopped flow assay. The experiment was performed by first equilibrating the MDCC labeled HIVRT-DNA complex and then rapidly mixing with a large amount of heparin. Because heparin traps all HIVRT that dissociates from DNA, the off-rate of DNA was measured by the time dependent fluorescence decrease. The experiments were also repeated at no Mg^{2+} or at 10 mM free Mg^{2+}. The result showed that the data from DNA dissociation could be fitted with a single exponential equation. Our study suggests that although the DNA binding is a two-step binding, the dissociation of DNA has only one rate-limiting step. Therefore, rapid equilibrium binding model was used for global data fitting (Scheme 5.2) based on numerical integration of the rate equations. The results showed that Mg^{2+} does not affect the initial binding (Scheme 5.2) and the forward conformational change (from the *ED* state to the *FD* state), but it affects the reverse of the conformational change (from the *FD* state back to the *ED* state) upon DNA dissociation. The off-rate of DNA at that step was decreased by more than 15-fold in the presence of 10 mM free Mg^{2+}.

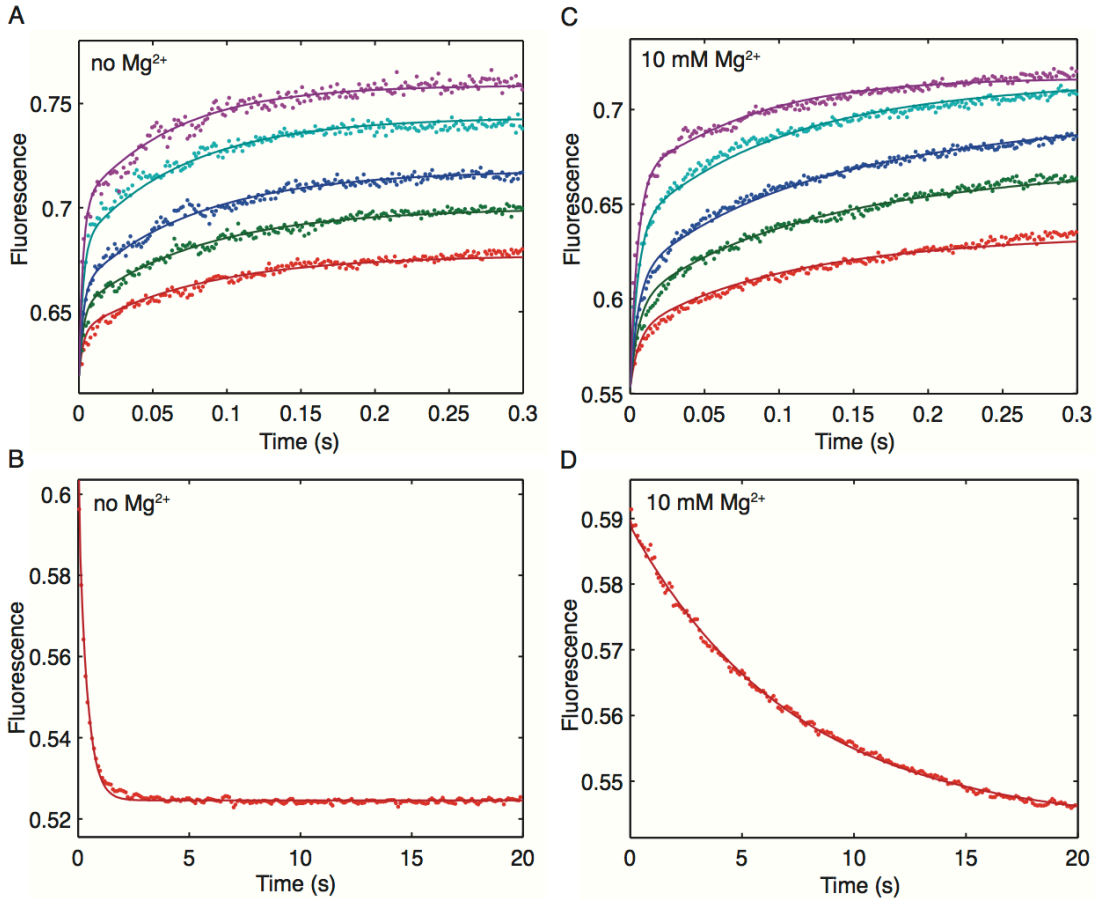

Figure 5.2 DNA binding to HIVRT in the absence or presence of Mg^{2+}.

The DNA binding experiment in the absence of Mg^{2+} (A) was performed by rapidly mixing ED complex (0.1 μM) with various concentrations of DNA (0.05, 0.075, 0.1, 0.15, 0.2 μM), and the DNA off-rate measurement in the absence of Mg^{2+} (B) was performed by premixing ED complex (0.1 μM) for 10 min, and then rapidly mixing with heparin trap (2 mg/ml). The DNA binding experiment (C) and DNA off-rate measurement (D) in the presence of 10 mM Mg^{2+} were performed similarly as shown above. The results from DNA binding and dissociation ((A and B) or (C and D)) were globally fit to the model shown in scheme 5.2 to rigorously define each kinetic parameter governing DNA binding.

To further investigate the effects of Mg^{2+} we measured the rate of DNA dissociation as a function of Mg^{2+} concentration using the heparin trap assay to get the results shown in Figure 5.3. The DNA dissociation rate as a function of the concentration of free Mg^{2+} was fit to a hyperbolic equation (Equation 5.3) to get the apparent K_d for Mg^{2+} binding and maximum dissociation rate. The result showed that Mg^{2+} binds to the preformed ED complex with a $K_{d,app}$ of 50 μM, and the binding of Mg^{2+} slows the rate of dissociation of DNA from the enzyme. It is possible that Mg^{2+} binds to a specific site of HIVRT and the binding of Mg^{2+} neutralizes some negative charge of the enzyme or that the binding of Mg^{2+} to DNA duplex favors a special structure or conformation of DNA and slows its dissociation from the enzyme. It is also likely that the Mg^{2+} associates weakly with multiple sites along the DNA as a counter-ion to the DNA polyelectrolyte and that the effective K_d is a function of multiple Mg^{2+} ions.

Equation 5.3 Apparent binding affinity calculation for Mg^{2+} binding to an enzyme DNA complex

$$k_{obs} = \frac{k_{max} + k_{min}[Mg]/K_d}{1+[Mg]/K_d}$$

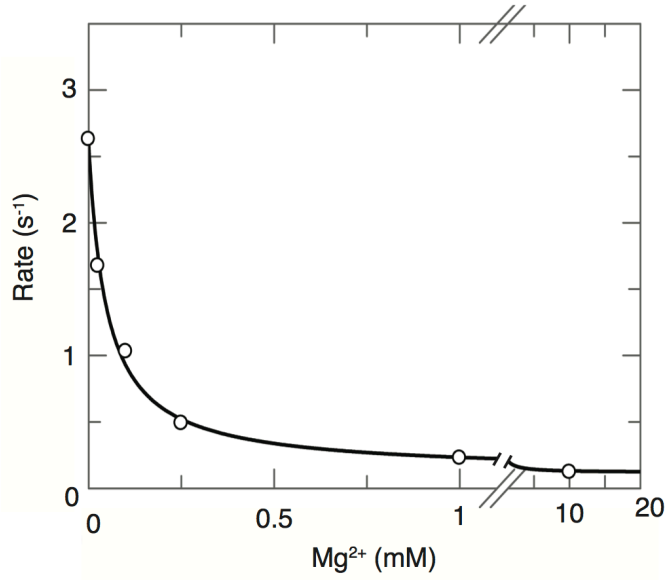

Figure 5.3 Mg^{2+} dependence of the DNA dissociation rate.

The DNA off-rate measurements were repeated with various concentrations of free Mg^{2+} (0, 0.025, 0.1, 0.25, 1 and 10 mM). The observed rates were then plotted as a function of Mg^{2+}, and fitted to the Equation 5.2.

Finally, the binding affinities of DNA were calculated from the on and off rates in the absence of Mg^{2+} or in the presence of 10 mM free Mg^{2+} using equation 5.4. The results showed that DNA binds to HIVRT with a K_d of 37.5 nM in the absence of Mg^{2+}, and a K_d of 0.9 nM in the presence of 10 mM free Mg^{2+} (Figure 5.4). The results suggest that Mg^{2+} stabilizes the DNA binding by about 40-fold in the presence of saturating (10 mM) free Mg^{2+}. Because the binding of DNA to enzyme (HIVRT) and binding of Mg^{2+} to ED complex are linked equilibria (Figure 5.4), the equilibrium constants governing either pathway should be the same. Because our previous data showed that Mg^{2+} binds to the preformed ED complex with a $K_{d,app}$ of 50 μM, the apparent binding affinity (K_d) of Mg^{2+} to enzyme or DNA alone was calculated as 2 mM.

Equation 5.4 The net K_d calculation for two-steps binding

$$K_{d,net} = \frac{1}{K_1\left(1+K_2\right)}$$

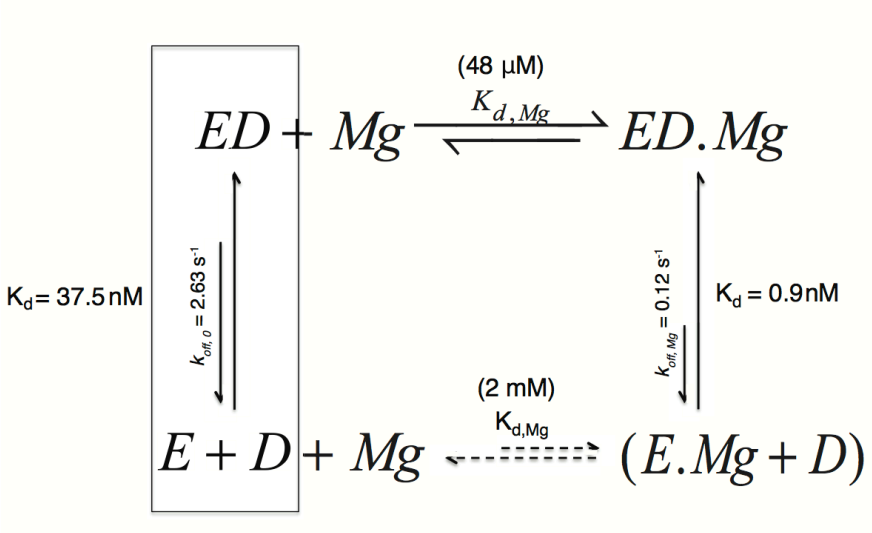

Figure 5.4 The effects of Mg^{2+} on the linked equilibria of DNA binding.

The rectangle region indicates the equilibrium of DNA binding in the absence of Mg^{2+}. Here the two-step DNA binding is reduced to a single step with the corresponding net K_d.

The effects of Mg^{2+} on processivity of HIVRT

The processivity of HIVRT was calculated at different concentrations of free Mg^{2+} ranging from 10 mM to 25 μM. The results showed that the processivity of HIVRT is highly Mg^{2+} dependent, as suggested by the Mg^{2+} concentration dependence of the polymerization and DNA dissociation rates. Compared with the values observed at 10 mM free Mg^{2+}, the processivity decreases by about 7, 80, and 1400-fold at 1 mM, 0.25 mM and 0.025 mM (or 25 μM) free Mg^{2+}, respectively (Table 5.3). The calculated processivity of HIVRT was then examined using by monitoring the Mg^{2+} dependence of the processivity in the following experiment. An enzyme-DNA complex was mixed with high concentrations of all four nucleotides to allow the incoming nucleotides to sequentially incorporate into the DNA template. The experiment was performed in the presence or absence of heparin trap added with the nucleotides, and the reaction was quenched at either 10 s or 3 min. The processivity of HIVRT was then directly observed by studying the number of nucleotides incorporated prior to dissociation of the DNA (equation 5.1). To test the efficiency of the heparin trap, four negative controls were used (Figure 5.5). In the control experiments, HIVRT was either first incubated with heparin for 10 min before mixing with DNA (control 1 and 2), or first incubated with DNA for 10 min before mixing with heparin (control 3 and control 4). If heparin could not trap HIVRT efficiently, nucleotide incorporation could be easily observed on the gel at the time scale of 3 min. As a result, no obvious band was observed indicating that the

efficiency of trap was high. The experiment was then repeated at different concentrations of Mg^{2+} (25 μM, 250 μM, 1 mM, and 10 mM). The results showed that the DNA was extended for multiple rounds of polymerization without the trap at 25 μM free Mg^{2+} (Figure 5.5). With the addition of the trap, almost half of the DNA primer (25nt) was not be extended even at the timescale of 3 min suggesting that the processivity of HIVRT is very low at 25 μM free Mg^{2+}. As the free Mg^{2+} concentration went up to 10 mM, almost all DNA were fully extended in the presence or absence of heparin indicating that the processivity of HIVRT is high at 10 mM free Mg^{2+}. The Mg^{2+} dependence of the processivity was also easily observed by directly comparing the length of the extended products in the presence of heparin after 3 min (Figure 5.5). Because the length of our DNA template was limited (~20 nucleotides long), the observed processivity at 1 mM or 10 mM Mg^{2+} condition was calculated as a minimum value (Table 5.3). The values of the observed processivity were consistent with the values of our calculated processivity (Table 5.3). Again, the results showed that the processivity of HIVRT is highly Mg^{2+} dependent.

Table 5.3 Mg^{2+} Dependent DNA Off-Rate and Processivity

$[Mg^{2+}]$, mM	$k_{off,DNA}$ (s^{-1})	k_{pol} (s^{-1})	Calculated Processivity[a]	Observed Processivity
0.025	1.67	< 0.14	< 0.1	0.6
0.25	0.49	0.9	1.8	1.6
1	0.22	4.12	19	> 8.5
10	0.12	16.7	139	> 16

[a]Processivity was calculated by using the equation of $k_{pol}/k_{off,DNA}$

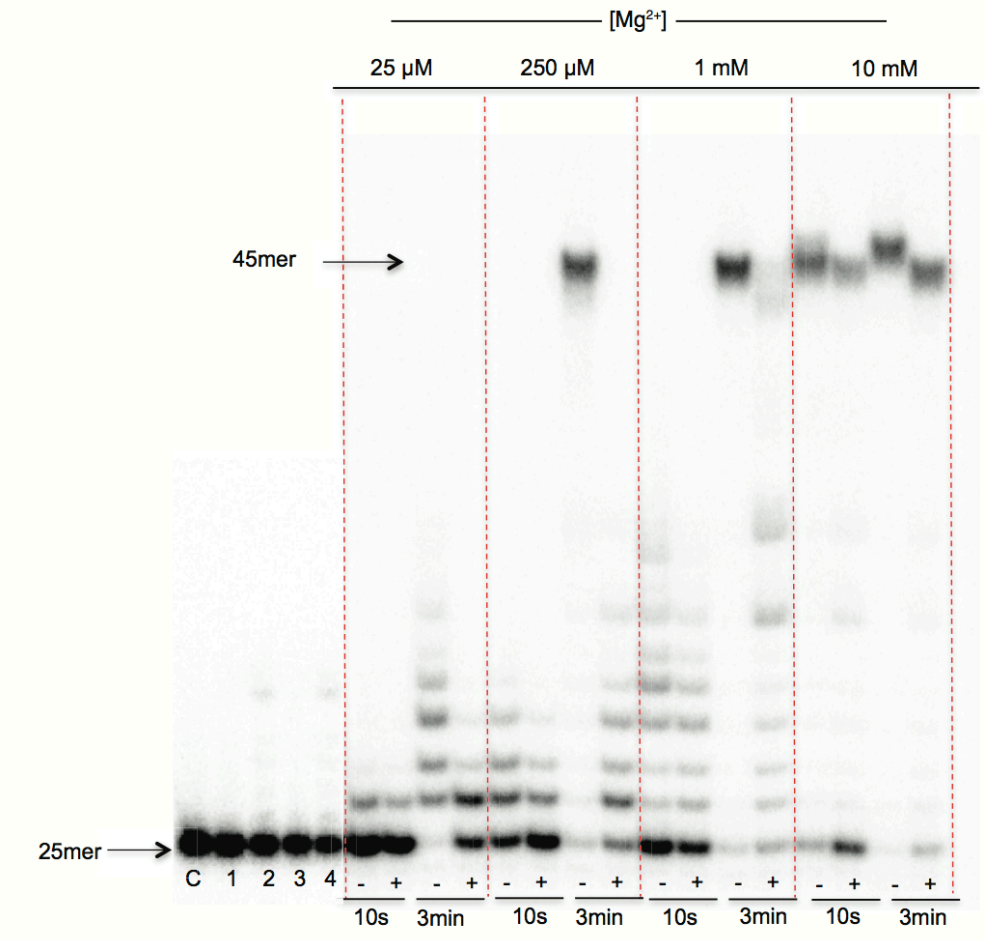

Figure 5.5 The effects of Mg^{2+} on the processivity of HIVRT.

The experiments were performed by mixing ED complex with 500 μM dNTP in the presence (+) or absence (-) of heparin trap (2 mg/ml), and the reactions were quenched at either 10s or 3 min. Five controls were used in the experiment, where C indicates ED complex alone and 1-4 indicates the conditions containing heparin in the reaction. The enzyme is premixed with heparin for 10 min, and then mixed with DNA for 10 min, and finally mixed with 500 μM dNTP in the presence of 10 mM Mg^{2+}. The reactions were quenched at 10s (1) and 3 min (2) respectively. Or the enzyme is premixed with DNA for 10 min, and then mixed with heparin for 10 min, and finally mixed with 500 μM dNTP in the presence of 10 mM Mg^{2+}. The reactions were quenched at 10s (3) and 3 min (4) respectively.

Because the processivity at 25 μM free Mg^{2+} is very low (<0.1), HIVRT actually does not have enough time to finish the nucleotide incorporation in the single DNA binding event. The k_{pol} values of both correct and mismatched incorporations (Table 5.2) are much lower than the value of $k_{off,DNA}$ (1.67 s^{-1}), suggesting both correct and mismatched incorporations are affected by the relative fast dissociation of DNA. Therefore, the extremely low processivity of HIVRT at 25 μM free Mg^{2+} affects the fidelity of HIVRT. As the free Mg^{2+} concentration goes up to 10 mM, the processivity of HIVRT goes up to around 140 in the correct nucleotide incorporation. In this case, the enzyme is highly processive and the fidelity of the enzyme is not affected by the relative slow DNA dissociation. Although mismatched nucleotide incorporations are much less efficient than correct nucleotide incorporation, the k_{pol} values of mismatched nucleotide incorporations are much higher than the value of $k_{off,DNA}$. Therefore, the mismatched nucleotide incorporations are also not affected by the relative slow DNA dissociation. In conclusion, a low processivity affects the fidelity but a high processivity does not. The possible correlation between processivity and fidelity is determined by the kinetic partition between the polymerization (k_{pol}) and DNA dissociation ($k_{off,DNA}$).

5.4 DISCUSSION

Fidelity is one of the most important features of DNA polymerases. In the absence of error correction, fidelity is entirely due the ability of the enzyme to discriminate mismatched nucleotides from correct base pairs. In nuclear DNA replication,

polymerases with high fidelity are required for maintaining the genome stability. Fidelity is attributed to many factors including base pairing geometry, hydrogen bonding, and substrate induced conformational change (159). It has been reported that the active sites of DNA polymerases are designed for accepting the signature geometry of correct base-pairing, and restricting the binding of mismatched base-pairs (159). All four correct nucleotides are very similar in their geometries including the glycosidic dihedral angles, C1'-C2' distances, and locations for hydrogen bonding groups in the DNA minor grooves (159). Those features are different among mismatches (159, 173, 174). In addition, the interaction between key residues in enzymes and the minor groove of the DNA may sense the base pair geometry at a distance and influence the enzyme fidelity (159). For example, DNA templates with different sequence may have different efficiencies for mismatched nucleotide incorporation (175). To facilitate the interaction, some DNA polymerases (eg. HIVRT and T7 pol) change the secondary structure of the DNA (from B form to A form) around the active site by bending the template by about 40° four-five based pairs from the active site (159, 164).

The substrate-induced conformational change also plays important roles in fidelity. For example, the binding of correct nucleotide induces a large conformational change of the enzyme (T7 pol and HIVRT)(123, 148), which brings the nucleotide to its optimum position for catalysis. The binding of mismatched nucleotides on the other hand may only induce partial or very limited closing of the enzyme (eg. pol β) (176), or an altered geometry (177) so that the misalignment of catalytic residues at the active site decreases the rate of mismatched nucleotide incorporation (159). Biochemical

experiments also demonstrate the role of the conformational change in enzyme fidelity. Correct nucleotide binding leads to a slow rate of nucleotide dissociation and a fast rate of chemistry so that once the nucleotide is bound, the kinetic partitioning favors the chemistry (126). Binding of a mismatched nucleotide fails to stabilize the closed enzyme state, leading to fast nucleotide dissociation and slow chemistry (130). Therefore, the efficiency of mismatched nucleotide incorporation is much lower than that of correct nucleotide incorporation.

The exonucleolytic proofreading activity and accessory proteins also affect the fidelity. The 3'-5' exonuclease activity can contributes more than 100 fold increase in fidelity (159). For example, T7 DNA polymerase has a fidelity around 10^{-5} and 10^{-6} range in exonuclease deficient mutant (178), and it has a fidelity around 10^{-8} and 10^{-9} range in wild type enzyme (179). The rate of excision by exonuclease activity is very slow as correct nucleotides are incorporated (efficient catalysis), and the rate of excision is high as mismatched nucleotide are incorporated (inefficient catalysis) (179). Accessory proteins play important roles in affecting the fidelity of some enzymes as well. It is reported that the fidelity of exonuclease deficient T7 DNA polymerase is increased by 46-fold with the assistance of its accessory protein thioredoxin (180). In eukaryotic cell, it is more obvious because the multiprotein replication complex highly increase the fidelity of replication (159).

HIVRT is a DNA polymerase with medium fidelity and no proofreading activity. The level of its fidelity allows it not only to maintain its basic genome stability but also evolve fast through generations to escape the host immune system and circumvent the

anti-viral treatment. It is important to compare fidelity estimates for HIVRT from analysis of replicate in cells with those obtained by *in vitro* measurements. HIVRT fidelity is estimated to be about 10^{-5} in most cellular experiments, and a fidelity around 10^{-4} range some *in vitro* experiments (108). Because the cellular Mg^{2+} concentrations were reported varying from 0.25 to 2 mM and most of the *in vitro* experiments used Mg^{2+} concentrations ranging from 5 to 10 mM (108, 166), the reported difference could be attributed to the differences in the free Mg^{2+} concentrations. Although it was reported that the fidelity of HIVRT went up to 10^{-5} range as the Mg^{2+} concentration was lowered to 0.25 mM, no significant difference was found between 2 mM and 6 mM (108). However, the reported steady state kinetic measurements are unreliable and in these studies the free Mg^{2+} concentration was not accurately controlled (108). For example, the binding equilibrium of Mg^{2+} and dNTP was considered as the only equilibrium in affecting the free Mg^{2+} concentration in solution (108). This assumption is valid in the high concentration of free Mg^{2+} (eg. 10 mM), but not in the low concentration of free Mg^{2+} (eg. 0.25 mM).

In this study, we revisited the effect of free Mg^{2+} by performing accurate measurements and data analysis. The results in our study suggested that there is no significant difference of fidelity between 10 mM free Mg^{2+} and 0.25 mM free Mg^{2+}. This result actually is consistent with a previous report showing that cellular concentrations of free Mg^{2+} concentration from 0.5 to 2 mM do not affect the fidelity of HIVRT (171). Because different mismatched nucleotides have different efficiency ($k_{pol}/K_{d,app}$) for incorporation, the fidelity of HIVRT, which is calculated by the equation of

$(k_{pol}/K_{d,app})_{mismatched}/(k_{pol}/K_{d,app})_{correct}$, is also affected by the specific mismatched-base pairings. The same phenomenon was also observed in our previous study where dG:T mismatched base pairing displays lower fidelity (10^{-4} range) than dC:T and T:T mismatched base pairing (10^{-5} range) (172). In addition, the calculation of fidelity could also be affected by a slow rate of pyrophosphate release. Whether the rate of pyrophosphate release is also slow in the mismatched incorporation using DNA template is still under investigation.

Finally, the observed difference of HIVRT fidelity between cellular experiments and some *in vitro* experiments may be caused by a combination of many factors. For example, the difference in the sequence of DNA template was also reported to affect the mismatched nucleotide incorporation (175). In addition, the fidelity other enzymes involved in HIVRT replication (eg. RNA polymerase II) is still unknown. If its fidelity is comparable to that of HIVRT, the observed fidelity from cellular experiments would be reduced. In addition, it has also been reported that additional cellular components such as HIV nucleic capsid protein (NC protein) may also affect the fidelity of HIVRT (108).

There are a total four Mg^{2+} binding sites in HIVRT, two in the polymerase active site and two in the RNase H site (58). Binding of Mg^{2+} to HIVRT is critical for both the polymerase activity and the RNase H activity (58, 105, 153). The results from this study showed that the binding of Mg^{2+} also stabilizes the binding of DNA to HIVRT. Compared with DNA binding in the absence of Mg^{2+}, the binding affinity increases by 40-fold in the presence of 10 mM free Mg^{2+}. DNA binding to HIVRT occurs in two steps binding, which could be understood as an initial binding step followed by a

conformational change step of HIVRT (scheme 5.2), each of which is reported by the MDCC-labeled protein. Higher Mg^{2+} concentration does not affect the kinetics of DNA binding, rather it only affects the rate of DNA dissociation, presumably by affecting the reverse of the conformational change of HIVRT (from the closed DNA bound state to the open DNA bound state). The results suggested that Mg^{2+} may bind to a specific site of HIVRT with K_d around 50 μM, and the binding of Mg^{2+} stabilizes the enzyme-DNA complex by slowing the reverse of the conformational change. Alternatively, Mg^{2+} may bind to the surface of DNA with K_d around 50 μM, and the binding of Mg^{2+} stabilizes the secondary structure of DNA by neutralizes some negative charge on the DNA surface. Although the binding of DNA-Mg^{2+} complex to HIVRT is similar to the binding of DNA to HIVRT, once the complex is bound, Mg^{2+} stabilizes the interaction between DNA and HIVRT and therefore significantly decreases the rate of DNA dissociation from HIVRT.

Binding of Mg^{2+} to the HIVRT-DNA is part of several linked equilibria. Mg^{2+} could either bind before or after the formation of the HIVRT-DNA complex, but more likely, it is in a rapid equilibrium with several binding sites during the process of DNA binding. Based on the thermodynamic box shown in Figure 5.4, we could calculate an apparent dissociation constant for Mg^{2+} binding to the free enzyme or DNA as 2 mM. It is reported that the binding of free Mg^{2+} (catalytic Mg^{2+}) to the polymerase active site of HIVRT is also very weak (K_d of 3.7 mM) in the process of nucleotide incorporation. It is possible that the Mg^{2+} observed here shares the same binding pocket with the catalytic Mg^{2+} in the polymerase active site, which could bind and release rapidly in the absence of nucleotides, and serves as the catalytic Mg^{2+} if the incoming nucleotide is bound. It is

also possible that the Mg^{2+} mentioned here binds to the RNase H site of HIVRT. The results from our study suggested that Mg^{2+} binds differently in the presence and absence of DNA. It is also reported that the structure of RNase H site is very different in the presence and absence of DNA (181). Therefore, it is possible that the RNase H site of HIVRT is complete and stable in the presence of DNA, and hence Mg^{2+} binds tightly with K_d around 50 μM. The structure of RNase H site is incomplete and very dynamic in the absence of DNA (181), and hence Mg^{2+} binds weakly to HIVRT with K_d of 2 mM. Then, the binding of Mg^{2+} neutralizes some negative charges at the RNase H site and prevents the repulsion of the DNA from HIVRT.

Processivity is another important feature of DNA polymerases and is defined by the number of nucleotides incorporated during the single DNA binding event (159). Therefore, the processivity is a function of DNA dissociation rate ($k_{off,DNA}$). For example, residues that interact with DNA contribute to the processivity of HIVRT (164). In addition, the processivity is also affected by the maximal rate of polymerization (k_{pol}). In this study, both $k_{off,DNA}$ and k_{pol} values were studied to investigate the processivity of HIVRT. The results suggested that the processivity of HIVRT is highly Mg^{2+} dependent, and the contribution from the change of the k_{pol} value is significant. Comparing the processivity at 10 mM free Mg^{2+}, the processvity of HIVRT is decreased by more than 1400-fold in the presence of 25 μM free Mg^{2+}, among which only about 14-fold comes from the change of $k_{off,DNA}$ value. Therefore, most of the effect (about 90%) on the processivity of HIVRT comes from the change of k_{pol} value.

Similarly, DNA dissociation ($k_{off,DNA}$) does not affect the fidelity. In our study, both correct and mismatched nucleotide incorporation does not reach completion during a single DNA binding event at 0.25 mM Mg^{2+}. A correlation was observed between low processivity and low fidelity, but this relationship could be two consequences of the failure to bind tightly and orient substrates for catalysis. A similar correlation has been reported previously, but the specific mechanism was unclear at that time. For example, it was reported that residues in thumb domain affect both the processivity and the fidelity of HIVRT (164). The fidelity of HIVRT was decreased when the DNA template contained sequences with a higher probability of termination (182 , 183). The study performed here provides a reasonable mechanism for this correlation.

To sum up, the studies performed here provide a systematic understanding about the effects of Mg^{2+} on HIVRT fidelity and processivity. The results in our study showed that Mg^{2+} does not significantly affect the fidelity of HIVRT as the Mg^{2+} concentration is increased from 0.25 mM to 10 mM. Mismatched base pairing, on the other hand, may have some effects on the calculation of fidelity due to their slight difference in the incorporation efficiency. In addition, the results in our study showed that the binding of Mg^{2+} stabilizes the binding of DNA by decreasing its dissociation rate. The results also indicate that kinetic partition between polymerization and DNA dissociation is critical to understand the correlation between the fidelity and processivity.

REFERENCE:

1. Vahlne A. A historical reflection on the discovery of human retroviruses. Retrovirology. 2009;6:40. PMCID: 2686671.
2. types HSa. AVERT. 2016.
3. Sharp PM, Hahn BH. Origins of HIV and the AIDS pandemic. Cold Spring Harb Perspect Med. 2011;1(1):a006841. PMCID: 3234451.
4. Marx PA, Alcabes PG, Drucker E. Serial human passage of simian immunodeficiency virus by unsterile injections and the emergence of epidemic human immunodeficiency virus in Africa. Philos Trans R Soc Lond B Biol Sci. 2001;356(1410):911-20. PMCID: 1088484.
5. Overview HitUSA. Center for Disease Control and Prevention. 2012 [updated 2012; cited]; Available from.
6. Baggaley RF, Boily MC, White RG, Alary M. Risk of HIV-1 transmission for parenteral exposure and blood transfusion: a systematic review and meta-analysis. AIDS. 2006;20(6):805-12.
7. Kripke C. Antiretroviral prophylaxis for occupational exposure to HIV. Am Fam Physician. 2007;76(3):375-6.
8. Vogel M, Schwarze-Zander C, Wasmuth JC, Spengler U, Sauerbruch T, Rockstroh JK. The treatment of patients with HIV. Dtsch Arztebl Int. 2010;107(28-29):507-15; quiz 16. PMCID: 2915483.
9. Hernandez-Vargas EA, Middleton RH. Modeling the three stages in HIV infection. J Theor Biol. 2013;320:33-40.
10. AIDS. MedlinePlus. 2012 Retrieved.
11. Sheet F. UNAIDSorg. 2013.
12. MDG 6: 15 Years lohftAr. UNAID. 2015.
13. WHO case definitions of HIV for surveillance and revised clinical staging and immunological classification of HIV-related disease in adults and children. Geneva: World Health Organization. 2007.
14. Mandell B, and Dolan. Chapter 18. 2010.
15. Kellerman S, Essajee S. HIV testing for children in resource-limited settings: what are we waiting for? PLoS Med. 2010;7(7):e1000285. PMCID: 2907270.
16. Crosby R, Bounse S. Condom effectiveness: where are we now? Sex Health. 2012;9(1):10-7.
17. Anglemyer A, Horvath T, Rutherford G. Antiretroviral therapy for prevention of HIV transmission in HIV-discordant couples. JAMA. 2013;310(15):1619-20.
18. Coutsoudis A, Kwaan L, Thomson M. Prevention of vertical transmission of HIV-1 in resource-limited settings. Expert Rev Anti Infect Ther. 2010;8(10):1163-75.
19. UNAIDS. The quest for an HIV vaccine. 2012.
20. General USAOotS. HIV Vaccine Trial in Thai Adult. ClinicalTrials gov. 2011.
21. Barbaro G, Barbarini G. Human immunodeficiency virus & cardiovascular risk. Indian J Med Res. 2011;134(6):898-903. PMCID: 3284097.

22. Cleghorn FR RM, Popovic M, Gallo RC. Human Immunodeficiency Viruses. In: Mandell GL, Bennett JE, Dolin R (eds). . Principles and Practice of Infectious Diseases 6th ed. 2005:pp2119-33.
23. Fisher RJ, Fivash MJ, Stephen AG, Hagan NA, Shenoy SR, Medaglia MV, et al. Complex interactions of HIV-1 nucleocapsid protein with oligonucleotides. Nucleic Acids Res. 2006;34(2):472-84. PMCID: 1351370.
24. Shum KT, Zhou J, Rossi JJ. Aptamer-based therapeutics: new approaches to combat human viral diseases. Pharmaceuticals (Basel). 2013;6(12):1507-42. PMCID: 3873675.
25. Engelman A, Cherepanov P. The structural biology of HIV-1: mechanistic and therapeutic insights. Nat Rev Microbiol. 2012;10(4):279-90. PMCID: 3588166.
26. Arts EJ, Hazuda DJ. HIV-1 antiretroviral drug therapy. Cold Spring Harb Perspect Med. 2012;2(4):a007161. PMCID: 3312400.
27. Wild C, Greenwell T, Matthews T. A synthetic peptide from HIV-1 gp41 is a potent inhibitor of virus-mediated cell-cell fusion. AIDS Res Hum Retroviruses. 1993;9(11):1051-3.
28. Rimsky LT, Shugars DC, Matthews TJ. Determinants of human immunodeficiency virus type 1 resistance to gp41-derived inhibitory peptides. J Virol. 1998;72(2):986-93. PMCID: 124569.
29. Reeves JD, Miamidian JL, Biscone MJ, Lee FH, Ahmad N, Pierson TC, et al. Impact of mutations in the coreceptor binding site on human immunodeficiency virus type 1 fusion, infection, and entry inhibitor sensitivity. J Virol. 2004;78(10):5476-85. PMCID: 400359.
30. Reeves JD, Lee FH, Miamidian JL, Jabara CB, Juntilla MM, Doms RW. Enfuvirtide resistance mutations: impact on human immunodeficiency virus envelope function, entry inhibitor sensitivity, and virus neutralization. J Virol. 2005;79(8):4991-9. PMCID: 1069568.
31. Kuhmann SE, Pugach P, Kunstman KJ, Taylor J, Stanfield RL, Snyder A, et al. Genetic and phenotypic analyses of human immunodeficiency virus type 1 escape from a small-molecule CCR5 inhibitor. J Virol. 2004;78(6):2790-807. PMCID: 353740.
32. Hart GJ, Orr DC, Penn CR, Figueiredo HT, Gray NM, Boehme RE, et al. Effects of (-)-2'-deoxy-3'-thiacytidine (3TC) 5'-triphosphate on human immunodeficiency virus reverse transcriptase and mammalian DNA polymerases alpha, beta, and gamma. Antimicrob Agents Chemother. 1992;36(8):1688-94. PMCID: 192031.
33. Lee H, Hanes J, Johnson KA. Toxicity of nucleoside analogues used to treat AIDS and the selectivity of the mitochondrial DNA polymerase. Biochemistry. 2003;42(50):14711-9.
34. Santos LH, Ferreira RS, Caffarena ER. Computational drug design strategies applied to the modelling of human immunodeficiency virus-1 reverse transcriptase inhibitors. Mem Inst Oswaldo Cruz. 2015;110(7):847-64. PMCID: 4660614.
35. Sluis-Cremer N, Temiz NA, Bahar I. Conformational changes in HIV-1 reverse transcriptase induced by nonnucleoside reverse transcriptase inhibitor binding. Curr HIV Res. 2004;2(4):323-32. PMCID: 1298242.

36. Esnouf R, Ren J, Ross C, Jones Y, Stammers D, Stuart D. Mechanism of inhibition of HIV-1 reverse transcriptase by non-nucleoside inhibitors. Nat Struct Biol. 1995;2(4):303-8.
37. Hsiou Y, Ding J, Das K, Clark AD, Jr., Hughes SH, Arnold E. Structure of unliganded HIV-1 reverse transcriptase at 2.7 A resolution: implications of conformational changes for polymerization and inhibition mechanisms. Structure. 1996;4(7):853-60.
38. Tachedjian G, Orlova M, Sarafianos SG, Arnold E, Goff SP. Nonnucleoside reverse transcriptase inhibitors are chemical enhancers of dimerization of the HIV type 1 reverse transcriptase. Proc Natl Acad Sci U S A. 2001;98(13):7188-93.
39. Spence RA, Kati WM, Anderson KS, Johnson KA. Mechanism of inhibition of HIV-1 reverse transcriptase by nonnucleoside inhibitors. Science. 1995;267(5200):988-93.
40. Xia Q, Radzio J, Anderson KS, Sluis-Cremer N. Probing nonnucleoside inhibitor-induced active-site distortion in HIV-1 reverse transcriptase by transient kinetic analyses. Protein Sci. 2007;16(8):1728-37.
41. Bacheler LT, Anton ED, Kudish P, Baker D, Bunville J, Krakowski K, et al. Human immunodeficiency virus type 1 mutations selected in patients failing efavirenz combination therapy. Antimicrob Agents Chemother. 2000;44(9):2475-84. PMCID: 90088.
42. Deeks SG. International perspectives on antiretroviral resistance. Nonnucleoside reverse transcriptase inhibitor resistance. J Acquir Immune Defic Syndr. 2001;26 Suppl 1:S25-33.
43. Espeseth AS, Felock P, Wolfe A, Witmer M, Grobler J, Anthony N, et al. HIV-1 integrase inhibitors that compete with the target DNA substrate define a unique strand transfer conformation for integrase. Proc Natl Acad Sci U S A. 2000;97(21):11244-9. PMCID: 17185.
44. Grobler JA, Stillmock K, Hu B, Witmer M, Felock P, Espeseth AS, et al. Diketo acid inhibitor mechanism and HIV-1 integrase: implications for metal binding in the active site of phosphotransferase enzymes. Proc Natl Acad Sci U S A. 2002;99(10):6661-6. PMCID: 124459.
45. Marinello J, Marchand C, Mott BT, Bain A, Thomas CJ, Pommier Y. Comparison of raltegravir and elvitegravir on HIV-1 integrase catalytic reactions and on a series of drug-resistant integrase mutants. Biochemistry. 2008;47(36):9345-54. PMCID: 2660605.
46. Park J, Morrow CD. Mutations in the protease gene of human immunodeficiency virus type 1 affect release and stability of virus particles. Virology. 1993;194(2):843-50.
47. Molla A, Korneyeva M, Gao Q, Vasavanonda S, Schipper PJ, Mo HM, et al. Ordered accumulation of mutations in HIV protease confers resistance to ritonavir. Nat Med. 1996;2(7):760-6.
48. Nijhuis M, Deeks S, Boucher C. Implications of antiretroviral resistance on viral fitness. Curr Opin Infect Dis. 2001;14(1):23-8.
49. Isel C, Lanchy JM, Le Grice SF, Ehresmann C, Ehresmann B, Marquet R. Specific initiation and switch to elongation of human immunodeficiency virus type 1

reverse transcription require the post-transcriptional modifications of primer tRNA3Lys. EMBO J. 1996;15(4):917-24. PMCID: 450289.
50. Hu WS, Hughes SH. HIV-1 reverse transcription. Cold Spring Harb Perspect Med. 2012;2(10). PMCID: 3475395.
51. Sarafianos SG, Marchand B, Das K, Himmel DM, Parniak MA, Hughes SH, et al. Structure and function of HIV-1 reverse transcriptase: molecular mechanisms of polymerization and inhibition. J Mol Biol. 2009;385(3):693-713. PMCID: 2881421.
52. Jacobo-Molina A, Ding J, Nanni RG, Clark AD, Jr., Lu X, Tantillo C, et al. Crystal structure of human immunodeficiency virus type 1 reverse transcriptase complexed with double-stranded DNA at 3.0 A resolution shows bent DNA. Proc Natl Acad Sci U S A. 1993;90(13):6320-4. PMCID: 46920.
53. Lightfoote MM, Coligan JE, Folks TM, Fauci AS, Martin MA, Venkatesan S. Structural characterization of reverse transcriptase and endonuclease polypeptides of the acquired immunodeficiency syndrome retrovirus. J Virol. 1986;60(2):771-5. PMCID: 288955.
54. Kohlstaedt LA, Wang J, Friedman JM, Rice PA, Steitz TA. Crystal structure at 3.5 A resolution of HIV-1 reverse transcriptase complexed with an inhibitor. Science. 1992;256(5065):1783-90.
55. Ghosh M, Jacques PS, Rodgers DW, Ottman M, Darlix JL, Le Grice SF. Alterations to the primer grip of p66 HIV-1 reverse transcriptase and their consequences for template-primer utilization. Biochemistry. 1996;35(26):8553-62.
56. Ghosh M, Williams J, Powell MD, Levin JG, Le Grice SF. Mutating a conserved motif of the HIV-1 reverse transcriptase palm subdomain alters primer utilization. Biochemistry. 1997;36(19):5758-68.
57. Sarafianos SG, Clark AD, Jr., Das K, Tuske S, Birktoft JJ, Ilankumaran P, et al. Structures of HIV-1 reverse transcriptase with pre- and post-translocation AZTMP-terminated DNA. EMBO J. 2002;21(23):6614-24. PMCID: 136941.
58. Huang H, Chopra R, Verdine GL, Harrison SC. Structure of a covalently trapped catalytic complex of HIV-1 reverse transcriptase: implications for drug resistance. Science. 1998;282(5394):1669-75.
59. Cowan JA, Ohyama T, Howard K, Rausch JW, Cowan SM, Le Grice SF. Metal-ion stoichiometry of the HIV-1 RT ribonuclease H domain: evidence for two mutually exclusive sites leads to new mechanistic insights on metal-mediated hydrolysis in nucleic acid biochemistry. J Biol Inorg Chem. 2000;5(1):67-74.
60. Pari K, Mueller GA, DeRose EF, Kirby TW, London RE. Solution structure of the RNase H domain of the HIV-1 reverse transcriptase in the presence of magnesium. Biochemistry. 2003;42(3):639-50.
61. Menendez-Arias L. Mechanisms of resistance to nucleoside analogue inhibitors of HIV-1 reverse transcriptase. Virus Res. 2008;134(1-2):124-46.
62. Feng JY, Myrick F, Selmi B, Deval J, Canard B, Borroto-Esoda K. Effects of HIV Q151M-associated multi-drug resistance mutations on the activities of (-)-beta-D-1',3'-dioxolan guanine. Antiviral Res. 2005;66(2-3):153-8.

63. Harrigan PR, Kinghorn I, Bloor S, Kemp SD, Najera I, Kohli A, et al. Significance of amino acid variation at human immunodeficiency virus type 1 reverse transcriptase residue 210 for zidovudine susceptibility. J Virol. 1996;70(9):5930-4. PMCID: 190612.
64. Hooker DJ, Tachedjian G, Solomon AE, Gurusinghe AD, Land S, Birch C, et al. An in vivo mutation from leucine to tryptophan at position 210 in human immunodeficiency virus type 1 reverse transcriptase contributes to high-level resistance to 3'-azido-3'-deoxythymidine. J Virol. 1996;70(11):8010-8. PMCID: 190874.
65. Lin PF, Samanta H, Rose RE, Patick AK, Trimble J, Bechtold CM, et al. Genotypic and phenotypic analysis of human immunodeficiency virus type 1 isolates from patients on prolonged stavudine therapy. J Infect Dis. 1994;170(5):1157-64.
66. Coakley EP, Gillis JM, Hammer SM. Phenotypic and genotypic resistance patterns of HIV-1 isolates derived from individuals treated with didanosine and stavudine. AIDS. 2000;14(2):F9-15.
67. Krebs R, Immendorfer U, Thrall SH, Wohrl BM, Goody RS. Single-step kinetics of HIV-1 reverse transcriptase mutants responsible for virus resistance to nucleoside inhibitors zidovudine and 3-TC. Biochemistry. 1997;36(33):10292-300.
68. Deval J, Navarro JM, Selmi B, Courcambeck J, Boretto J, Halfon P, et al. A loss of viral replicative capacity correlates with altered DNA polymerization kinetics by the human immunodeficiency virus reverse transcriptase bearing the K65R and L74V dideoxynucleoside resistance substitutions. J Biol Chem. 2004;279(24):25489-96.
69. Gao HQ, Boyer PL, Sarafianos SG, Arnold E, Hughes SH. The role of steric hindrance in 3TC resistance of human immunodeficiency virus type-1 reverse transcriptase. J Mol Biol. 2000;300(2):403-18.
70. Sarafianos SG, Das K, Clark AD, Jr., Ding J, Boyer PL, Hughes SH, et al. Lamivudine (3TC) resistance in HIV-1 reverse transcriptase involves steric hindrance with beta-branched amino acids. Proc Natl Acad Sci U S A. 1999;96(18):10027-32. PMCID: 17836.
71. Ray AS, Basavapathruni A, Anderson KS. Mechanistic studies to understand the progressive development of resistance in human immunodeficiency virus type 1 reverse transcriptase to abacavir. J Biol Chem. 2002;277(43):40479-90.
72. Tisdale M, Kemp SD, Parry NR, Larder BA. Rapid in vitro selection of human immunodeficiency virus type 1 resistant to 3'-thiacytidine inhibitors due to a mutation in the YMDD region of reverse transcriptase. Proc Natl Acad Sci U S A. 1993;90(12):5653-6. PMCID: 46779.
73. Mewshaw JP, Myrick FT, Wakefield DA, Hooper BJ, Harris JL, McCreedy B, et al. Dioxolane guanosine, the active form of the prodrug diaminopurine dioxolane, is a potent inhibitor of drug-resistant HIV-1 isolates from patients for whom standard nucleoside therapy fails. J Acquir Immune Defic Syndr. 2002;29(1):11-20.
74. Zhang Z, Walker M, Xu W, Shim JH, Girardet JL, Hamatake RK, et al. Novel nonnucleoside inhibitors that select nucleoside inhibitor resistance mutations in human immunodeficiency virus type 1 reverse transcriptase. Antimicrob Agents Chemother. 2006;50(8):2772-81. PMCID: 1538665.

75. Wei X, Liang C, Gotte M, Wainberg MA. Negative effect of the M184V mutation in HIV-1 reverse transcriptase on initiation of viral DNA synthesis. Virology. 2003;311(1):202-12.
76. Back NK, Nijhuis M, Keulen W, Boucher CA, Oude Essink BO, van Kuilenburg AB, et al. Reduced replication of 3TC-resistant HIV-1 variants in primary cells due to a processivity defect of the reverse transcriptase enzyme. EMBO J. 1996;15(15):4040-9. PMCID: 452124.
77. Shirasaka T, Kavlick MF, Ueno T, Gao WY, Kojima E, Alcaide ML, et al. Emergence of human immunodeficiency virus type 1 variants with resistance to multiple dideoxynucleosides in patients receiving therapy with dideoxynucleosides. Proc Natl Acad Sci U S A. 1995;92(6):2398-402. PMCID: 42491.
78. Iversen AK, Shafer RW, Wehrly K, Winters MA, Mullins JI, Chesebro B, et al. Multidrug-resistant human immunodeficiency virus type 1 strains resulting from combination antiretroviral therapy. J Virol. 1996;70(2):1086-90. PMCID: 189915.
79. Gu Z, Allard B, de Muys JM, Lippens J, Rando RF, Nguyen-Ba N, et al. In vitro antiretroviral activity and in vitro toxicity profile of SPD754, a new deoxycytidine nucleoside reverse transcriptase inhibitor for treatment of human immunodeficiency virus infection. Antimicrob Agents Chemother. 2006;50(2):625-31. PMCID: 1366874.
80. Paolucci S, Baldanti F, Maga G, Cancio R, Zazzi M, Zavattoni M, et al. Gln145Met/Leu changes in human immunodeficiency virus type 1 reverse transcriptase confer resistance to nucleoside and nonnucleoside analogs and impair virus replication. Antimicrob Agents Chemother. 2004;48(12):4611-7. PMCID: 529209.
81. Deval J, Selmi B, Boretto J, Egloff MP, Guerreiro C, Sarfati S, et al. The molecular mechanism of multidrug resistance by the Q151M human immunodeficiency virus type 1 reverse transcriptase and its suppression using alpha-boranophosphate nucleotide analogues. J Biol Chem. 2002;277(44):42097-104.
82. Meyer PR, Smith AJ, Matsuura SE, Scott WA. Effects of primer-template sequence on ATP-dependent removal of chain-terminating nucleotide analogues by HIV-1 reverse transcriptase. J Biol Chem. 2004;279(44):45389-98.
83. Yahi N, Tamalet C, Tourres C, Tivoli N, Ariasi F, Volot F, et al. Mutation patterns of the reverse transcriptase and protease genes in human immunodeficiency virus type 1-infected patients undergoing combination therapy: survey of 787 sequences. J Clin Microbiol. 1999;37(12):4099-106. PMCID: 85889.
84. Hanna GJ, Johnson VA, Kuritzkes DR, Richman DD, Brown AJ, Savara AV, et al. Patterns of resistance mutations selected by treatment of human immunodeficiency virus type 1 infection with zidovudine, didanosine, and nevirapine. J Infect Dis. 2000;181(3):904-11.
85. Boyer PL, Sarafianos SG, Arnold E, Hughes SH. Selective excision of AZTMP by drug-resistant human immunodeficiency virus reverse transcriptase. J Virol. 2001;75(10):4832-42. PMCID: 114238.
86. Boyer PL, Sarafianos SG, Arnold E, Hughes SH. Nucleoside analog resistance caused by insertions in the fingers of human immunodeficiency virus type 1 reverse

transcriptase involves ATP-mediated excision. J Virol. 2002;76(18):9143-51. PMCID: 136461.
87. Matamoros T, Franco S, Vazquez-Alvarez BM, Mas A, Martinez MA, Menendez-Arias L. Molecular determinants of multi-nucleoside analogue resistance in HIV-1 reverse transcriptases containing a dipeptide insertion in the fingers subdomain: effect of mutations D67N and T215Y on removal of thymidine nucleotide analogues from blocked DNA primers. J Biol Chem. 2004;279(23):24569-77.
88. Cases-Gonzalez CE, Franco S, Martinez MA, Menendez-Arias L. Mutational patterns associated with the 69 insertion complex in multi-drug-resistant HIV-1 reverse transcriptase that confer increased excision activity and high-level resistance to zidovudine. J Mol Biol. 2007;365(2):298-309.
89. Masquelier B, Race E, Tamalet C, Descamps D, Izopet J, Buffet-Janvresse C, et al. Genotypic and phenotypic resistance patterns of human immunodeficiency virus type 1 variants with insertions or deletions in the reverse transcriptase (RT): multicenter study of patients treated with RT inhibitors. Antimicrob Agents Chemother. 2001;45(6):1836-42. PMCID: 90554.
90. Villena C, Prado JG, Puertas MC, Martinez MA, Clotet B, Ruiz L, et al. Relative fitness and replication capacity of a multinucleoside analogue-resistant clinical human immunodeficiency virus type 1 isolate with a deletion of codon 69 in the reverse transcriptase coding region. J Virol. 2007;81(9):4713-21. PMCID: 1900151.
91. Delviks-Frankenberry KA, Nikolenko GN, Barr R, Pathak VK. Mutations in human immunodeficiency virus type 1 RNase H primer grip enhance 3'-azido-3'-deoxythymidine resistance. J Virol. 2007;81(13):6837-45. PMCID: 1933283.
92. Brehm JH, Koontz D, Meteer JD, Pathak V, Sluis-Cremer N, Mellors JW. Selection of mutations in the connection and RNase H domains of human immunodeficiency virus type 1 reverse transcriptase that increase resistance to 3'-azido-3'-dideoxythymidine. J Virol. 2007;81(15):7852-9. PMCID: 1951314.
93. Gu Z, Arts EJ, Parniak MA, Wainberg MA. Mutated K65R recombinant reverse transcriptase of human immunodeficiency virus type 1 shows diminished chain termination in the presence of 2',3'-dideoxycytidine 5'-triphosphate and other drugs. Proc Natl Acad Sci U S A. 1995;92(7):2760-4. PMCID: 42298.
94. White KL, Margot NA, Wrin T, Petropoulos CJ, Miller MD, Naeger LK. Molecular mechanisms of resistance to human immunodeficiency virus type 1 with reverse transcriptase mutations K65R and K65R+M184V and their effects on enzyme function and viral replication capacity. Antimicrob Agents Chemother. 2002;46(11):3437-46. PMCID: 128721.
95. Margot NA, Waters JM, Miller MD. In vitro human immunodeficiency virus type 1 resistance selections with combinations of tenofovir and emtricitabine or abacavir and lamivudine. Antimicrob Agents Chemother. 2006;50(12):4087-95. PMCID: 1693985.
96. Das K, Bandwar RP, White KL, Feng JY, Sarafianos SG, Tuske S, et al. Structural basis for the role of the K65R mutation in HIV-1 reverse transcriptase polymerization, excision antagonism, and tenofovir resistance. J Biol Chem. 2009;284(50):35092-100. PMCID: 2787370.

97. Lwatula C, Garforth SJ, Prasad VR. Lys66 residue as a determinant of high mismatch extension and misinsertion rates of HIV-1 reverse transcriptase. FEBS J. 2012;279(21):4010-24. PMCID: 3472125.
98. Michailidis E, Ryan EM, Hachiya A, Kirby KA, Marchand B, Leslie MD, et al. Hypersusceptibility mechanism of Tenofovir-resistant HIV to EFdA. Retrovirology. 2013;10:65. PMCID: 3695782.
99. White KL, Chen JM, Feng JY, Margot NA, Ly JK, Ray AS, et al. The K65R reverse transcriptase mutation in HIV-1 reverses the excision phenotype of zidovudine resistance mutations. Antivir Ther. 2006;11(2):155-63.
100. Brenner BG, Coutsinos D. The K65R mutation in HIV-1 reverse transcriptase: genetic barriers, resistance profile and clinical implications. HIV Ther. 2009;3(6):583-94. PMCID: 2826981.
101. Grant PM, Taylor J, Nevins AB, Calvez V, Marcelin AG, Wirden M, et al. International cohort analysis of the antiviral activities of zidovudine and tenofovir in the presence of the K65R mutation in reverse transcriptase. Antimicrob Agents Chemother. 2010;54(4):1520-5. PMCID: 2849386.
102. Tu X, Das K, Han Q, Bauman JD, Clark AD, Jr., Hou X, et al. Structural basis of HIV-1 resistance to AZT by excision. Nat Struct Mol Biol. 2010;17(10):1202-9. PMCID: 2987654.
103. Hoogewerf M, Regez RM, Schouten WE, Weigel HM, Frissen PH, Brinkman K. Change to abacavir-lamivudine-tenofovir combination treatment in patients with HIV-1 who had complete virological suppression. Lancet. 2003;362(9400):1979-80.
104. Frankel FA, Invernizzi CF, Oliveira M, Wainberg MA. Diminished efficiency of HIV-1 reverse transcriptase containing the K65R and M184V drug resistance mutations. AIDS. 2007;21(6):665-75.
105. Steitz TA, Steitz JA. A general two-metal-ion mechanism for catalytic RNA. Proc Natl Acad Sci U S A. 1993;90(14):6498-502.
106. Castro C, Smidansky ED, Arnold JJ, Maksimchuk KR, Moustafa I, Uchida A, et al. Nucleic acid polymerases use a general acid for nucleotidyl transfer. Nat Struct Mol Biol. 2009;16(2):212-8. PMCID: 2728625.
107. Rezende LF, Kew Y, Prasad VR. The effect of increased processivity on overall fidelity of human immunodeficiency virus type 1 reverse transcriptase. J Biomed Sci. 2001;8(2):197-205.
108. Achuthan V, Keith BJ, Connolly BA, DeStefano JJ. Human immunodeficiency virus reverse transcriptase displays dramatically higher fidelity under physiological magnesium conditions in vitro. J Virol. 2014;88(15):8514-27. PMCID: 4135932.
109. Delva P, Pastori C, Degan M, Montesi G, Lechi A. Catecholamine-induced regulation in vitro and ex vivo of intralymphocyte ionized magnesium. J Membr Biol. 2004;199(3):163-71.
110. Rink TJ, Tsien RY, Pozzan T. Cytoplasmic pH and free Mg2+ in lymphocytes. J Cell Biol. 1982;95(1):189-96. PMCID: 2112339.

111. Nakamura T, Zhao Y, Yamagata Y, Hua YJ, Yang W. Watching DNA polymerase eta make a phosphodiester bond. Nature. 2012;487(7406):196-201. PMCID: 3397672.
112. Freudenthal BD, Beard WA, Shock DD, Wilson SH. Observing a DNA polymerase choose right from wrong. Cell. 2013;154(1):157-68. PMCID: 3924593.
113. Molina JM, Marcelin AG, Pavie J, Heripret L, De Boever CM, Troccaz M, et al. Didanosine in HIV-1-infected patients experiencing failure of antiretroviral therapy: a randomized placebo-controlled trial. J Infect Dis. 2005;191(6):840-7.
114. Winters MA, Bosch RJ, Albrecht MA, Katzenstein DA. Clinical impact of the M184V mutation on switching to didanosine or maintaining lamivudine treatment in nucleoside reverse-transcriptase inhibitor-experienced patients. J Infect Dis. 2003;188(4):537-40.
115. Eron JJ, Jr., Bosch RJ, Bettendorf D, Petch L, Fiscus S, Frank I. The effect of lamivudine therapy and M184V on the antiretroviral activity of didanosine. J Acquir Immune Defic Syndr. 2007;45(2):249-51.
116. Rhee SY, Taylor J, Wadhera G, Ben-Hur A, Brutlag DL, Shafer RW. Genotypic predictors of human immunodeficiency virus type 1 drug resistance. Proc Natl Acad Sci U S A. 2006;103(46):17355-60. PMCID: 1622926.
117. Boyer PL, Sarafianos SG, Arnold E, Hughes SH. The M184V mutation reduces the selective excision of zidovudine 5'-monophosphate (AZTMP) by the reverse transcriptase of human immunodeficiency virus type 1. J Virol. 2002;76(7):3248-56. PMCID: 136050.
118. Mouroux M, Descamps D, Izopet J, Yvon A, Delaugerre C, Matheron S, et al. Low-rate emergence of thymidine analogue mutations and multi-drug resistance mutations in the HIV-1 reverse transcriptase gene in therapy-naive patients receiving stavudine plus lamivudine combination therapy. Antivir Ther. 2001;6(3):179-83.
119. Ray AS, Murakami E, Basavapathruni A, Vaccaro JA, Ulrich D, Chu CK, et al. Probing the molecular mechanisms of AZT drug resistance mediated by HIV-1 reverse transcriptase using a transient kinetic analysis. Biochemistry. 2003;42(29):8831-41.
120. Meyer PR, Matsuura SE, Mian AM, So AG, Scott WA. A mechanism of AZT resistance: an increase in nucleotide-dependent primer unblocking by mutant HIV-1 reverse transcriptase. Mol Cell. 1999;4(1):35-43.
121. Meyer PR, Matsuura SE, Schinazi RF, So AG, Scott WA. Differential removal of thymidine nucleotide analogues from blocked DNA chains by human immunodeficiency virus reverse transcriptase in the presence of physiological concentrations of 2'-deoxynucleoside triphosphates. Antimicrob Agents Chemother. 2000;44(12):3465-72. PMCID: 90226.
122. Parikh UM, Bacheler L, Koontz D, Mellors JW. The K65R mutation in human immunodeficiency virus type 1 reverse transcriptase exhibits bidirectional phenotypic antagonism with thymidine analog mutations. J Virol. 2006;80(10):4971-7. PMCID: 1472090.

123. Kellinger MW, Johnson KA. Nucleotide-dependent conformational change governs specificity and analog discrimination by HIV reverse transcriptase. Proc Natl Acad Sci U S A. 2010;107(17):7734-9.
124. Johnson KA. Role of induced fit in enzyme specificity: a molecular forward/reverse switch. J Biol Chem. 2008;283(39):26297-301.
125. Larder BA, Kemp SD. Multiple mutations in HIV-1 reverse transcriptase confer high-level resistance to zidovudine (AZT). Science. 1989;246(4934):1155-8.
126. Kellinger MW, Johnson KA. Role of induced fit in limiting discrimination against AZT by HIV reverse transcriptase. Biochemistry. 2011;50(22):5008-15. PMCID: 3381507.
127. Shanzhong Gong aKAJ. The Role of K65R in HIV-1 Resistance to AZT and Tenofovir Excision. In prep. 2014.
128. Hanes JW, Johnson KA. A novel mechanism of selectivity against AZT by the human mitochondrial DNA polymerase. Nucleic Acids Res. 2007;35(20):6973-83. PMCID: 2175305.
129. Hanes JW, Johnson KA. Real-time measurement of pyrophosphate release kinetics. Anal Biochem. 2008;372(1):125-7. PMCID: 3381508.
130. Kirmizialtin S, Nguyen V, Johnson KA, Elber R. How conformational dynamics of DNA polymerase select correct substrates: experiments and simulations. Structure. 2012;20(4):618-27. PMCID: 3322391.
131. Li JZ, Sax PE. AZT or tenofovir for patients with the K65R mutation? J Watch AIDS Clin Care. 2010;22(6):51-2.
132. Deval J, White KL, Miller MD, Parkin NT, Courcambeck J, Halfon P, et al. Mechanistic basis for reduced viral and enzymatic fitness of HIV-1 reverse transcriptase containing both K65R and M184V mutations. J Biol Chem. 2004;279(1):509-16.
133. Parikh UM, Barnas DC, Faruki H, Mellors JW. Antagonism between the HIV-1 reverse-transcriptase mutation K65R and thymidine-analogue mutations at the genomic level. J Infect Dis. 2006;194(5):651-60.
134. Selmi B, Deval J, Boretto J, Canard B. Nucleotide analogue binding, catalysis and primer unblocking in the mechanisms of HIV-1 reverse transcriptase-mediated resistance to nucleoside analogues. Antivir Ther. 2003;8(2):143-54.
135. Mas A, Parera M, Briones C, Soriano V, Martinez MA, Domingo E, et al. Role of a dipeptide insertion between codons 69 and 70 of HIV-1 reverse transcriptase in the mechanism of AZT resistance. EMBO J. 2000;19(21):5752-61. PMCID: 305792.
136. Goldschmidt V, Marquet R. Primer unblocking by HIV-1 reverse transcriptase and resistance to nucleoside RT inhibitors (NRTIs). Int J Biochem Cell Biol. 2004;36(9):1687-705.
137. Parikh UM, Zelina S, Sluis-Cremer N, Mellors JW. Molecular mechanisms of bidirectional antagonism between K65R and thymidine analog mutations in HIV-1 reverse transcriptase. AIDS. 2007;21(11):1405-14.
138. White KL, Margot NA, Ly JK, Chen JM, Ray AS, Pavelko M, et al. A combination of decreased NRTI incorporation and decreased excision determines the resistance profile of HIV-1 K65R RT. AIDS. 2005;19(16):1751-60.

139. Traut TW. Physiological concentrations of purines and pyrimidines. Mol Cell Biochem. 1994;140(1):1-22.
140. Shanzhong Gong aKAJ. The Role of K65R in HIV-1 Resistance to AZT and Tenofovir Incorporation. In Prep. 2014.
141. Dharmasena S, Pongracz Z, Arnold E, Sarafianos SG, Parniak MA. 3'-Azido-3'-deoxythymidine-(5')-tetraphospho-(5')-adenosine, the product of ATP-mediated excision of chain-terminating AZTMP, is a potent chain-terminating substrate for HIV-1 reverse transcriptase. Biochemistry. 2007;46(3):828-36.
142. Pitcher WH, 3rd, Kirby TW, DeRose EF, London RE. Metabolic transformation of AZTp4A by Ap4A hydrolase regenerates AZT triphosphate. Antiviral Res. 2003;58(3):227-33.
143. Matthew W. Kellinger* ST, Jonas Korlach†, and Kenneth A. Johnson*‡. Single-Molecule Kinetic Analysis Reveals AZT Impacts
HIV RT Isomerization More Than Translocation. In Prep. 2014.
144. Yang L, Arora K, Beard WA, Wilson SH, Schlick T. Critical role of magnesium ions in DNA polymerase beta's closing and active site assembly. J Am Chem Soc. 2004;126(27):8441-53.
145. Fenstermacher KJ, DeStefano JJ. Mechanism of HIV reverse transcriptase inhibition by zinc: formation of a highly stable enzyme-(primer-template) complex with profoundly diminished catalytic activity. J Biol Chem. 2011;286(47):40433-42. PMCID: 3220506.
146. Martell LGSaAE. Stability constants of metal-ion complexes. The Chemical Society. 1964.
147. Storer AC, Cornish-Bowden A. Concentration of MgATP2- and other ions in solution. Calculation of the true concentrations of species present in mixtures of associating ions. Biochem J. 1976;159(1):1-5. PMCID: 1164030.
148. Tsai YC, Johnson KA. A new paradigm for DNA polymerase specificity. Biochemistry. 2006;45(32):9675-87.
149. Brune M, Hunter JL, Howell SA, Martin SR, Hazlett TL, Corrie JE, et al. Mechanism of inorganic phosphate interaction with phosphate binding protein from Escherichia coli. Biochemistry. 1998;37(29):10370-80.
150. Bakhtina M, Lee S, Wang Y, Dunlap C, Lamarche B, Tsai MD. Use of viscogens, dNTPalphaS, and rhodium(III) as probes in stopped-flow experiments to obtain new evidence for the mechanism of catalysis by DNA polymerase beta. Biochemistry. 2005;44(13):5177-87.
151. Lee HR, Wang M, Konigsberg W. The reopening rate of the fingers domain is a determinant of base selectivity for RB69 DNA polymerase. Biochemistry. 2009;48(10):2087-98. PMCID: 2845987.
152. Klumpp K, Hang JQ, Rajendran S, Yang Y, Derosier A, Wong Kai In P, et al. Two-metal ion mechanism of RNA cleavage by HIV RNase H and mechanism-based design of selective HIV RNase H inhibitors. Nucleic Acids Res. 2003;31(23):6852-9. PMCID: 290251.

153. Cristofaro JV, Rausch JW, Le Grice SF, DeStefano JJ. Mutations in the ribonuclease H active site of HIV-RT reveal a role for this site in stabilizing enzyme-primer-template binding. Biochemistry. 2002;41(36):10968-75.
154. Yang W, Lee JY, Nowotny M. Making and breaking nucleic acids: two-Mg2+-ion catalysis and substrate specificity. Mol Cell. 2006;22(1):5-13.
155. Valberg LS, Holt JM, Paulson E, Szivek J. Spectrochemical Analysis of Sodium, Potassium, Calcium, Magnesium, Copper, and Zinc in Normal Human Erythrocytes. J Clin Invest. 1965;44:379-89. PMCID: 292488.
156. Walser M. Magnesium metabolism. Ergeb Physiol. 1967;59:185-296.
157. Delva P, Pastori C, Degan M, Montesi G, Lechi A. Intralymphocyte free magnesium and plasma triglycerides. Life Sci. 1998;62(24):2231-40.
158. Tashiro M, Konishi M. Basal intracellular free Mg2+ concentration in smooth muscle cells of guinea pig tenia cecum: intracellular calibration of the fluorescent indicator furaptra. Biophys J. 1997;73(6):3358-70. PMCID: 1181237.
159. Kunkel TA, Bebenek K. DNA replication fidelity. Annu Rev Biochem. 2000;69:497-529.
160. Bibillo A, Eickbush TH. High processivity of the reverse transcriptase from a non-long terminal repeat retrotransposon. J Biol Chem. 2002;277(38):34836-45.
161. Kelman Z, Hurwitz J, O'Donnell M. Processivity of DNA polymerases: two mechanisms, one goal. Structure. 1998;6(2):121-5.
162. Joyce CM, Steitz TA. Polymerase structures and function: variations on a theme? J Bacteriol. 1995;177(22):6321-9. PMCID: 177480.
163. Cen S, Niu M, Kleiman L. The connection domain in reverse transcriptase facilitates the in vivo annealing of tRNALys3 to HIV-1 genomic RNA. Retrovirology. 2004;1:33. PMCID: 524520.
164. Bebenek K, Beard WA, Darden TA, Li L, Prasad R, Luton BA, et al. A minor groove binding track in reverse transcriptase. Nat Struct Biol. 1997;4(3):194-7.
165. Garforth SJ, Domaoal RA, Lwatula C, Landau MJ, Meyer AJ, Anderson KS, et al. K65R and K65A substitutions in HIV-1 reverse transcriptase enhance polymerase fidelity by decreasing both dNTP misinsertion and mispaired primer extension efficiencies. J Mol Biol. 2010;401(1):33-44. PMCID: 2925049.
166. Goldschmidt V, Didierjean J, Ehresmann B, Ehresmann C, Isel C, Marquet R. Mg2+ dependency of HIV-1 reverse transcription, inhibition by nucleoside analogues and resistance. Nucleic Acids Res. 2006;34(1):42-52. PMCID: 1325016.
167. Wang M, Lee HR, Konigsberg W. Effect of A and B metal ion site occupancy on conformational changes in an RB69 DNA polymerase ternary complex. Biochemistry. 2009;48(10):2075-86. PMCID: 2846627.
168. Wang S, McDonnell EH, Sedor FA, Toffaletti JG. pH effects on measurements of ionized calcium and ionized magnesium in blood. Arch Pathol Lab Med. 2002;126(8):947-50.
169. Maguire ME, Cowan JA. Magnesium chemistry and biochemistry. Biometals. 2002;15(3):203-10.

170. Moomaw AS, Maguire ME. The unique nature of mg2+ channels. Physiology (Bethesda). 2008;23:275-85. PMCID: 2711038.
171. Holtz CM, Mansky LM. Variation of HIV-1 mutation spectra among cell types. J Virol. 2013;87(9):5296-9. PMCID: 3624292.
172. Kati WM, Johnson KA, Jerva LF, Anderson KS. Mechanism and fidelity of HIV reverse transcriptase. J Biol Chem. 1992;267(36):25988-97.
173. Seeman NC, Rosenberg JM, Rich A. Sequence-specific recognition of double helical nucleic acids by proteins. Proc Natl Acad Sci U S A. 1976;73(3):804-8. PMCID: 336007.
174. Kou Y, Koag MC, Lee S. N7 methylation alters hydrogen-bonding patterns of guanine in duplex DNA. J Am Chem Soc. 2015;137(44):14067-70.
175. Naiser T, Kayser J, Mai T, Michel W, Ott A. Position dependent mismatch discrimination on DNA microarrays - experiments and model. BMC Bioinformatics. 2008;9:509. PMCID: 2661940.
176. Sawaya MR, Prasad R, Wilson SH, Kraut J, Pelletier H. Crystal structures of human DNA polymerase beta complexed with gapped and nicked DNA: evidence for an induced fit mechanism. Biochemistry. 1997;36(37):11205-15.
177. Tsai YC, Jin Z, Johnson KA. Site-specific labeling of T7 DNA polymerase with a conformationally sensitive fluorophore and its use in detecting single-nucleotide polymorphisms. Anal Biochem. 2009;384(1):136-44. PMCID: 3045965.
178. Patel SS, Wong I, Johnson KA. Pre-steady-state kinetic analysis of processive DNA replication including complete characterization of an exonuclease-deficient mutant. Biochemistry. 1991;30(2):511-25.
179. Donlin MJ, Patel SS, Johnson KA. Kinetic partitioning between the exonuclease and polymerase sites in DNA error correction. Biochemistry. 1991;30(2):538-46.
180. Kunkel TA, Patel SS, Johnson KA. Error-prone replication of repeated DNA sequences by T7 DNA polymerase in the absence of its processivity subunit. Proc Natl Acad Sci U S A. 1994;91(15):6830-4. PMCID: 44291.
181. Zheng X, Mueller GA, DeRose EF, London RE. Metal and ligand binding to the HIV-RNase H active site are remotely monitored by Ile556. Nucleic Acids Res. 2012;40(20):10543-53. PMCID: 3488238.
182. Bebenek K, Abbotts J, Roberts JD, Wilson SH, Kunkel TA. Specificity and mechanism of error-prone replication by human immunodeficiency virus-1 reverse transcriptase. J Biol Chem. 1989;264(28):16948-56.
183. Bebenek K, Abbotts J, Wilson SH, Kunkel TA. Error-prone polymerization by HIV-1 reverse transcriptase. Contribution of template-primer misalignment, miscoding, and termination probability to mutational hot spots. J Biol Chem. 1993;268(14):10324-34.